DOCTORAATSPROEFSCHRIFT

2007 | Faculteit Wetenschappen

Morphological, thermal and electrical characterization of organic photovoltaic blends

Proefschrift voorgelegd tot het behalen van de graad,
Doctor in de wetenschappen, richting natuurkunde, te verdedigen door:

Ann Swinnen

Promotor: Prof. Dr. Jean Manca
Co-promotor: Prof. Dr. Marc D'Olieslaeger

universiteit hasselt
INSTITUUT VOOR MATERIAALONDERZOEK

Dankwoord

Hier zijn we dan, een hele thesis geschreven en dan nog de moed vinden om het dankwoord te schrijven. Meermaals tijdens het schrijven heb ik snode plannen bedacht om de thesis zelf niet te moeten schrijven: mensen geld beloofd, kaboutertjes gezocht, de pc onder mijn hoofdkussen gelegd in de hoop dat mijn gedachten vanzelf goed geschreven in de pc geraakten, meerdere malen pc en raam aan elkaar geassocieerd en als laatste hoopte ik een huiself zoals Dobby (de laatste Harry Potter boek laat zijn sporen na) te vinden. Spijtig maar helaas moest ik het zelf doen, niemand kon me helpen. Ik denk dat iedereen er wel kan van meespreken dat ik veel geklaagd en gezaagd heb de laatste maanden, en daarom verdient iedereen van jullie toch een plekje in mijn dankwoord voor de vele steun en de aanmoedigingen wanneer het even niet meer ging. Dankzij jullie allemaal ben ik er geraakt, thanks folks!

In de eerste plaats wil ik prof. dr. Jean Manca, mijn promotor, en prof. dr. Marc D'Olieslaeger bedanken om mij de kans te geven een doctoraat te kunnen aanvangen op het IMO. Jean bedankt dat je altijd vertrouwen had in die scheikundige die zich een moeilijke weg moest banen door toch wel voor mij onlogische fysica: halfgeleiders, elektrische metingen, elektrostatische krachten microscopie,…. Je stond altijd klaar voor een goeie peptalk en frisse ideeën. Ook tijdens de moeilijke momenten zowel op werkvlak als privé stond je steeds klaar met begripvolle en motiverende woorden. Mede dankzij jou heb ik het kunnen volhouden.
In de tweede plaats zou ik dr. Jan D'Haen willen bedanken. Als ik een kritische beoordeling wou of de expert op vlak van analytische technieken dan is er maar één man op het IMO waar je moet zijn en dat is Jan. Jan bedankt om me regelmatig bij te staan met je deskundige uitleg en innoverende ideeën. Dankzij jou hebben we de PCBM kristallen gevonden, terwijl ik als groentje dacht dat mijn film kapot was heb jij me overtuigd om er nog eens naar te kijken. Je hebt me geleerd om meer kritisch te zijn en steeds naar oplossingen te blijven zoeken, één van de belangrijkste elementen van een onderzoeker. Je drive werkte aanstekelijk want als we met Jan achter de SEM of TEM zaten was er geen sprake van stoppen. We hebben beiden op hetzelfde moment even tegenslag gekend, maar net datgene heeft ons korter bij elkaar gebracht. Ik zal de vele gesprekken missen en aan wie moet ik nu mijn wilde verhalen gaan vertellen? Jan het ga je goed en ik denk dat ik in de toekomst weinig kans ga hebben om zo'n goeie band te hebben met één van mijn bazen.
Prof. dr. Dirk Vanderzande, mijn steun op scheikundig vlak, wat was ik toch blij dat ik een scheikundige tijdens mijn PhD meetings had. Dankzij je connecties bij de VUB, is het toch uiteindelijk gelukt om een fase diagramma op te stellen.

Over de VUB gesproken, prof. dr. ir. Guy Van Assche je was een super hulp om me wegwijs te maken in de thermische analyse van polymeren. Met jouw kennis over thermisch gedrag van polymeren en mijn morfologie studies zijn we er geraakt. Bedankt dat je altijd tijd kon maken in je drukke agenda en veel succes nog met de lessen chinees. Ik voelde me een beetje terug thuis komen bij de chemische ingenieurs. Eindelijk een materie waar ik me toch een beetje meer op mijn gemak bij voelde. Hierbij mag ik zeker prof. dr. ir. Bruno Van Mele niet vergeten die toch steeds klaar stond met deskundige uitleg en hulp om tijdens meetings het menggedrag van polymeren toe te lichten. Bruno bedankt dat ik in jouw groep al de DSC metingen mocht komen uitvoeren. Jun thanks a lot for all the endless DSC and MTDSC measurements you performed for me. The tempo at which you performed these measurements was incredible and without you I wasn’t able to get this wonderfull initial state diagram. Nele, je bent een super meid en vond het fijn met je samen te werken. Veel succes met het schrijven van je doctoraatsthesis. Kristof, jij zorgde voor de nodige toffe afleiding en maakte het eindeloze wachten op de DSC resultaten heel wat minder erg. Veel succes met je doctoraatsthesis. Voor de rest van de groep wou ik zeggen dat ik het super vond bij jullie en zeker tijdens de laatste BPG meeting in Houffalise. Jullie zijn één voor één toffe mensen en het VUB restaurant is nog steeds beter dan dat van de UHasselt. In Hasselt hadden ze al schrik dat ik niet meer ging terugkomen. Dat zegt genoeg denk ik.

Olivier merci pour tous que tu as fais pour moi. Merci beaucoup pour ton aide avec mes C-AFM expérimentes et les EFM expérimentes. Sans toi je ne pouvais jamais réussir à comprendre se truc difficile. T’étais toujours prêts pour m’aider avec mes textes et quand je recevrais mes corrections, mon papier étais toujours complètement rouge mais comme ça j’appréciais que tu t’avais fait ton meilleur effort pour que tout était parfait. T’es un super mec et je vais te manquer et je vais certainement penser à toi la prochaine fois que je suis derrière le AFM et c’est si silencieux sans toi parce qu’avec toi il y avait toujours de la musique. Je vous souhaites le meilleur en tous ce que tu vas faire : le théâtre, le rugby et ton nouveau boulot. Bonne chance!

Special thanks also goes to dr. Alexander Volodin and prof. dr. Van Haesendonck. Alexander, I really appreciate all the effort you did to help me with the EFM measurements. You always believed in the great results that would be obtained. Thanks for sharing all your knowledge about EFM with me and for always being patient when I didn’t completely understand everything. I wouldn’t have succeeded at all without you since in the beginning EFM measurements equalled to Chinese for me. I also want to thank you and your wife for your warm welcome during my house hunting.

Dan zijn we bij alle IMO collega’s aanbeland. Toen ik 4 jaar geleden in het IMO aankwam had ik nooit durven dromen dat ik zo’n super tijd met jullie allemaal ging hebben. Wat oorspronkelijk collega’s waren zijn toch wel vrienden geworden en sommige heel goeie vrienden zelfs. Limburgers zijn echt wel toffe mensen al werd er bij mijn eerste presentatie toch geadviseerd om een beetje trager te spreken. Ik zal zeker nooit vergeten wat een steun jullie me gegeven hebben tijdens die moeilijke periode in het begin van mijn doctoraat. Bedankt voor jullie vele kaartjes en dat jullie zo talrijk aanwezig waren. Limburgers hebben echt een warm hart. Ik ga jullie allemaal missen dat is een feit wat zeker is.

Christel en Hilde onze twee toffe laborantes. Hilde bedankt om me altijd bij te staan bij de preparatie van nieuwe stalen en de SEM metingen. En dan ons Christel, het is er me eentje. Christel bedankt om altijd klaar te staan om me te helpen met de pure scheikundige dingen en mijn voorraad wafertrays in toom te houden. Ik kon altijd bij je terecht voor zowel privé-zaken als werk gerelateerd. Je hebt me dikwijls een hart onder de riem gestoken en ik zal je missen. Vooral de discussies tussen jou en Johnny zal ik zeker niet vergeten. Johnny, je stond altijd klaar om direct hulp te verlenen met technische problemen. Ik denk niet dat er een betere handige “Johnny” bestaat dan jij. Zelfs in het weekend wanneer ik weer een van mijn chlorobenzeen rijke experimenten uitvoerde stond je klaar om me te helpen met de glovebox. Nen dikke merci! Dany bedankt om tijd te maken voor de altijd moeilijke microtomie experimenten. Jan bedankt om me te helpen met het verouderingskamertje en de programmatie van mijn verwarmplaat, en geef nu toe mijn keramisch houdertje heeft toch zijn vruchten afgeworpen. Erik bedankt om me altijd te helpen wanneer mijn pc weer rare kuren kreeg. Kris bedankt voor de SEM metingen en voor het delen van morele leed tijdens het schrijven van deze thesis want we zaten alletwee in hetzelfde schuitje. Bart bedankt voor de vele XRD metingen.

Dan zijn we aan onze beste secretaresses beland die er kunnen zijn : Relinde, Lea en Marina. Relinde je was er altijd als ik een luisterend oor nodig had bedankt voor de toffe 4 jaren en Lea mercikes om me altijd met die onkostennota’s uit de nood te helpen want geef nu toe die zijn toch wel moeilijk opgesteld.

En dan mijn bureaugenootjes. Evi, je bent een van mijn beste vriendinnen geworden. Het principe van tot 10 tellen is een van je beste uitvindingen, vooral als ik weer snel opgejaagd was. Ik vind het super dat ik altijd op je kan rekenen. Ik heb enorm veel van je geleerd en bedankt voor de toffe tijd zonder jou was het veel minder leuk geweest. Onze Ludwig mag ik toch ook niet vergeten ondanks dat hij nu tussen de american babes zit. Ik denk dat we onze relatie het beste als een haat liefde verhouding kunnen beschrijven. De pennen vlogen meermaals van de ene bureau naar de andere maar ik vond je toch een super kerel. Het ga je nu goed in de States en veel succes nog in alles wat je doet. PS: ik heb mijn tijger gevonden! Na onze Ludwig hebben we toch als evenwaardige vervanger Rob gekregen. Rob bedankt voor de toffe pauzes. Koen, je was meestal vrij stil maar als er iets uitkwam dan was het ook meteen raak en lagen we allemaal onder tafel. Je maakte de skivakantie altijd geslaagd en er zijn weinige snowboarders die ons zo goed kon volgen als jij. Bedankt om me te

helpen met de zonnecelmetingen en met het model om de mobiliteiten te berekenen. Nu we toch de zonnecellengroep aan het bedanken zijn zullen we maar verder gaan met diegene die de meest aanstekelijke lach heeft van heel het IMO, ons bijna eerste Belgische vrouw in space. Ilse, ik zal je eerst maar bedanken voor de eindeloze TEM en XRD metingen die je voor mij gedaan hebt en dat waren er veel. Sorry voor de daardoor opgelopen verkoudheden en keelpijnen omdat ik je weer eens in het super gekoelde TEM kamertje liet zitten maar het was toch soms fijn. Voor Ilse diende er geen verlofkalender ingevuld te worden enkel de decibels moesten gemeten worden en we wisten genoeg. Jij bracht echt leven in de brouwerij en zonder jou was het veel minder leuk geweest. Je stond altijd klaar voor mij, zelfs al was er weer een dringende kermat die af moest. Je hebt me heel veel geholpen en ik weet ik val in herhaling maar op persoonlijk vlak heb je me dikwijls erdoor geholpen en ben je daar heel dankbaar voor. Dat bureaugenootje van jou was er ook altijd met de nodige juiste raad en aanvankelijk was ze wat stil en bedeesd maar kijk we hebben ze los gekregen. Mijn enige thesisstudent maar het was een goeike, ons Sabine. Sabine bedankt voor ook de meerdere TEM metingen (en ook sorry voor de nodige verkoudheden) en de toffe tijd tijdens onze skivakanties. Bedankt voor de oppeppende woorden. Onze laatste zonnecelman: Wouter. Tja wat zou nen burgie doen zonder nen industrieel ingenieur in de buurt, den burgie zou nog gene multimeter kunnen gebruiken. Daar ging mijn reputatie van burgie al de eerste maand. Wouter bedankt voor al de technische hulp met multimeters, opdampen, gloveboxdingen kortom laten we zeggen elektronica was nooit mijn sterkste vak. Bedankt voor de morele steun en de hulp met pc problemen en alle toffe vrijdagavonden in de cafetaria wanneer we daar allen zaten uit te blazen van de zware week met een La Chouffe. Van La Chouffe gesproken, Ronald je bent de beste kerstman ooit! Ik zal je grappen nooit vergeten en zeker de grappige en soms ook wel irritante ringtones die door de gang zoemden. Mercikes om me met de pc problemen altijd uit de nood te helpen. Veel succes nog met de bouw van je huis. Hoe kunnen we Rob het beste omschrijven, zullen we maar zeggen prettig gestoord. Dankzij jou waren de luchpauzes echt wel hilarisch. Niemand kan beter een kip of koe nabootsen dan jij. Rob je hebt de 4 jaar op het IMO echt super gemaakt. Michael was er ook altijd bij als er te feesten viel. Bedankt voor de toffe skivakanties en voor de nodige les die ik nog gekregen heb. Als we toch bij diamant aangekomen zijn is er toch nog een persoon die ik zeker niet mag vergeten en wil bedanken. Ken, je bent tijdens die eerste jaren een heel goeie vriend van me geworden, zelfs een van de beste. Bedankt voor de vele toffe etentjes tijdens de middag en de leuke tijd. Je was er altijd voor me als ik je nodig had en pas op voor de jeneverkes he.
Als ik nog iemand van het IMO moest vergeten zijn sorry en bedankt.

Mijn vrienden mogen hier zeker niet ontbreken. Katrien bedankt om er altijd te zijn voor mij tijdens de moeilijke momenten. Ik zal nooit vergeten hoe je er was voor mij 4 jaar geleden. Je bent een toffe madam, het party animal bij uitstek. Ik wens je het beste toe want dat verdien je. An bedankt voor de jarenlange vriendschap en steun. Bedankt voor de vele toffe squash avondjes en tennismatchkes. Griet, je was er ook altijd voor me met de juiste raad. Ines, Steven, David en Tom, jullie hebben het laatste 1,5 jaar super gemaakt. Onze wekelijkse etentjes, drankjes, op stap gaan het is gewoon super. Ik denk dat niemand van ons 5 kon geloven dat we zo'n toffe vriendengroep zouden hebben. Dank u allemaal voor de vele morele steun tijdens de moeilijke momenten.

Mijn ouders mogen hier ook zeker niet ontbreken. Mama je bent er altijd voor mij geweest, en je bent mijn beste vriendin. Samen hebben we al moeilijke tijden doorstaan maar toch was je er altijd voor me, en je hebt me gesteund in alles wat ik deed, hoe moeilijk ook. Je stond me bij met raad en daad en ondanks dat ik je niet altijd wilde geloven bleek toch dat je altijd gelijk had. Je dochter kwam altijd op de eerste plaats, zelfs voor jezelf. Papa, je zal dit nooit kunnen lezen maar toch vind ik dat iedereen moeten weten dat ik enorm naar je opkeek. Je zou zo fier geweest zijn het moment dat ik dit doctoraat zou gehaald hebben. Je steunde me altijd voluit en je moedigde me altijd aan om het moeilijkste te kiezen. Dankzij jou ben ik sterker geworden en mijn doorzettingsvermogen en koppigheid heb ik van jou. We waren twee dezelfde karakters en dat kan wel eens botsen, maar voor mij was je de beste papa. Mama en papa bedankt voor me deze kans te geven en voor alle fijne momenten samen.

En dan last but zeker not least mijn chocoprins. We zijn nog niet zo lang samen maar je hebt me de laatste 8 maanden altijd gesteund en me altijd bijgestaan. Ook je ouders hebben hun steentje bijgedragen en me gesteund. Ik vind je super en had nooit gedacht dat ik eindelijk eens geluk ging hebben en mijn zalm zou vinden. Bij jou kon ik me ontspannen tijdens de moeilijke thesismomenten en kan ik mezelf zijn. Je kan me opvrolijken en me de kracht geven om door te gaan. Bij jou voel ik dat ik alles kan en je laat me voelen als een prinses. Ihvj.

Table of contents

4. LOCAL ELECTRICAL PROPERTIES 85

Nederlandse samenvatting

De toenemende wereldpopulatie vereist een grotere energieproductie. In 2003, werd 77% van alle energieproductie geleverd door fossiele brandstoffen, echter het grote nadeel van deze uitputbare bron is de productie van CO_2, verantwoordelijk voor de opwarming van de aarde. Hernieuwbare energie biedt hier een aantal interessante mogelijkheden zoals bijvoorbeeld fotovoltaïsche energie. Toch vormt nog steeds de productiekost van fotovoltaïsche panelen een belemmering voor de doorbraak van deze vorm van energieproductie. Organisch geconjugeerde polymeren zouden hiervoor een oplossing kunnen bieden. Door het gebruik van geconjugeerde polymeren kunnen op grote schaal goedkoop flexibele zogenaamde “plastic” zonnecellen gemaakt worden. Reeds gedurende enige tijd is de studie voor plastic zonnecellen aan de gang. Gaande van enkelvoudige polymeer lagen naar een 2-laag structuur (polymeer en organische molecule) tot het bulk heterojunctie concept. De actieve laag van deze zogenaamde “bulk heterojunctie” zonnecel bestaat uit een mengsel van een donor materiaal, typisch een geconjugeerd polymeer, en een acceptor materiaal, meestal een C_{60} derivaat. Aangezien dat bulk heterojunctie zonnecellen, bestaande uit een mengsel van het geconjugeerde polymeer regioregulair poly(3-hexylthiophene) (P3HT) en het C_{60}-derivaat methanofullerene: [6-6]-phenyl C_{61} butyric acid methyl ester (PCBM), de beste efficiëntie behaalde, bij de aanvang van dit doctoraatsproefschrift, werd de focus op dit materiaal systeem gelegd. Bovendien was dit systeem nog weinig begrepen en optimalisatie van dit systeem, met behulp van bijvoorbeeld temperatuursbehandeling, diende nog nagestreefd te worden. Er werd aangetoond dat een zonnecel bestaande uit een P3HT:PCBM mengsel significant verbeterde wanneer een temperatuursbehandeling van 5 min op 75°C werd toegepast. Deze temperatuur komt overeen met de reële werkingscondities van een zonnecel maar er was niet geweten hoe de structuur verandert. Daarom was het vooraleerst noodzakelijk om een uitgebreide morfologie studie uit te voeren. In een tweede fase werd er een poging gedaan om de morfologie te linken aan de elektrische eigenschappen, aangezien ook deze relatie onvoldoende begrepen was.

In een eerste experimentele hoofdstuk werd om bovengenoemde redenen de morfologie van het regioregulair P3HT gemengd met PCBM uitgebreid bestudeerd met de hulp van transmissie elektronen microscopie (TEM), X-stralen diffractie (XRD), atomaire kracht microscopie (AFM), confocale fluorescentie microscopie en optische microscopie. Beide materialen werden gemengd in verschillende verhoudingen en onderworpen aan verscheidene temperatuursbehandelingen. Puur P3HT werd gekarakteriseerd als een semi-kristallijn materiaal. Door toevoeging van PCBM werd de dimensie verkleind van het gebied met geordend P3HT. Een aangepaste temperatuursbehandeling zorgt er dan voor dat P3HT zijn oorspronkelijke kristallijne fase gedeeltelijk of volledig terug krijgt. Afhankelijk van de temperatuursbehandeling kon er een dubbele kristallisatie verkregen worden. Bij korte verwarmingstijden (i.e. 5 min) en lage temperaturen (i.e. 75°C-100°C) werd een toename in kristalllijne P3HT gebieden geobserveerd. Bij toenemende temperatuur en verwarmingstijd, werd een nieuw soort naaldvormige PCBM kristallen gevormd van nanometer tot μm schaal waarbij lengtes tot zelfs 100 μm werden geobserveerd. Door gebruik te maken van specifieke preparatiecondities kunnen deze naalden uitgroeien tot een twee dimensionaal netwerk van kristallen en zelfs waaiervormige kristallen kunnen bekomen worden. Er werd aangetoond dat de P3HT:PCBM mengverhouding en de aangepaste verwarmingscondities de belangrijkste parameters zijn om de grootte van deze PCBM kristallen te controleren. Aangezien deze vorm en grootte van PCBM kristallen nooit eerder gerapporteerd werden, werd er nagegaan wat de oorzaak van de specifieke vormgeving is en hoe ze bekomen wordt. Er werd aangetoond dat niet zozeer het kristallisatie mechanisme van regioregulair P3HT de oorzaak is, aangezien verwarmde regiorandom P3HT dezelfde PCBM kristallen opleverde, maar eerder de lage glasovergangstemperatuur (i.e. 18.7°C) van het regioregulaire P3HT in combinatie met een verschillende “start” morfologie in vergelijking met de MDMO-PPV:PCBM blends. De PCBM kristallen zelf werden vervolgens meer nauwkeurig bestudeerd. Er werd gevonden dat PCBM kristalliseert triklien. Rondom de naalden werd een dunnere regio met bijna puur kristallijn P3HT gevonden, duidend op de diffusie van PCBM uit de matrix naar het groeiende kristal onder invloed van temperatuur. Voor de eerste maal in dit onderzoeksgebied werd vervolgens confocale fluorescentie microscopie gebruikt om te bevestigen dat de omringende PCBM regio bestaat uit bijna puur kristallijn P3HT. Een irreversibele morfologie van puur kristallijn P3HT omgeven door PCBM kristallen werd bekomen wanneer alle PCBM uit de matrix gediffundeerd was, voor de 1:2 mengverhouding werd dit bereikt na een verwarming van 8-16 uur op 100°C. Eveneens werden volledige zonnecellen gemaakt en hier werden eveneens de grote PCBM kristallen geobserveerd, waardoor er aangetoond werd dat het P3HT:PCBM mengsel helemaal geen thermisch stabiel mengsel is.

Om een duidelijk idee te krijgen hoe en waarom de P3HT:PCBM mengverhouding deze welbepaalde morfologie geeft, geobserveerd in het eerste experimentele hoofdstuk, werd een toestandsdiagramma opgesteld. Differentiële scanning calorimetrie (DSC) werd daarom gebruikt om het smelt- en kristallisatiegedrag te bestuderen, terwijl gemoduleerde temperatuur differentiële scanning calorimetrie (MTDSC) gebruikt werd om voornamelijk de glasovergangstemperatuur (T_g) te bepalen. Eerst werd het pure P3HT en PCBM bestudeerd gevolgd door de mengsels. Een T_g van 18.7°C, een smelttemperatuur van 209°C en een kristallisatietemperatuur van 179°C werd gevonden voor puur P3HT, dewelke in overeenstemming zijn met de waarden gerapporteerd in de literatuur. Zowel de kristallisatie- als de smeltpieken vertoonden een schouder waarschijnlijk afkomstig van verschillende kristalvormen. Voor de eerste keer werd een T_g van PCBM gevonden, i.e. 130°C. Een dubbele smeltpiek, een kleinere ter hoogte van 266°C gevolgd door een grotere op 287°C, werd geobserveerd voor PCBM. Puur PCBM kan triklien en/of monoklien kristalliseren. Deze dubbele smeltpiek is daarom waarschijnlijk afkomstig van de aanwezigheid van beide kristalvormen. Verschillende metingen met behulp van XRD en EBSD konden echter hierover geen definitief duidelijk bewijs leveren. Een enkelvoudige kristallisatiepiek was gevonden rond 228°C. Voor alle mengverhoudingen werd een enkelvoudige T_g gevonden, dewelke door toevoegen van PCBM aan P3HT, verschuift van de T_g van P3HT naar die van PCBM. De afwezigheid van een dubbele T_g wijst erop dat alle mengsels in een homogene fase zijn, tot op een schaal van 10 nm, dus alleen kristallisatie geïnduceerde fasescheiding kon gevonden worden en geen intrinsieke vloeistof-vloeistof fasescheiding. Als bevestiging hiervan werd er eveneens geen fasescheiding gevonden in de smeltfase. Uit het smelt- en kristallisatiegedrag van de mengsels kon besloten worden dat bij toenemende P3HT concentratie de smeltkristallisatietemperatuur van PCBM duidelijk verlaagd werd, terwijl dit effect minder duidelijk was in het smeltgedrag van PCBM. Omgekeerd, wanneer PCBM toegevoegd wordt aan P3HT, verlaagt eveneens de smeltkristallisatietemperatuur en de smelttemperatuur van P3HT. Het effect is bij deze laatstgenoemde meer uitgesproken. Er kan dus gezegd worden dat beide componenten elkaars kristallisatiegedrag verstoren. Het meest amorfe mengsel werd daarom bekomen bij een gewichtsconcentratie van 60% PCBM. In het tweede hoofdstuk werd reeds gevonden dat PCBM de kristallisatie van PCBM verstoort, desondanks deze resultaten werd er hier aangetoond dat door het opstellen van een initieel toestandsdiagramma, sneller en een meer accuraat idee kan gegeven worden over hoe een mengsel zich morfologisch gedraagt. Aangezien dat de werkingstemperatuur van een zonnecel 80°C kan bedragen kan het begin van de glasovergang als een belangrijke parameter beschouwd worden in de studie van zonnecellen. Immers beneden de glasovergang bevindt het mengsel zich in een stabiele glastoestand zodat geen morfologische veranderingen meer tot stand kunnen gebracht worden. Enkel dus P3HT:PCBM mengsels met een gewichtsconcentratie gelijk aan of hoger dan 90% PCBM zijn in de glasfase bij een temperatuur van 80°C. Dit betekent dat de P3HT:PCBM mengsels niet geschikt zijn voor zonnecellen waar een lange termijn thermische stabiliteit noodzakelijk is. Desondanks, fysische veroudering kan nog steeds plaats vinden in de glastoestand. Aangezien dat de eigenschappen van een P3HT:PCBM gebaseerde zonnecel verbeteren door een temperatuursbehandeling, door de toenemende kristallisatie van P3HT, kan het einde van de glasovergang gebruikt worden als de benedengrens voor de temperatuur gebruikt bij de temperatuursbehandeling.

In de hoofdstukken 2 en 3 werd een uitgebreide morfologie studie uitgevoerd. Aangezien dat morfologie een belangrijke rol speelt in de performantie van bulk heterojunctie zonnecellen is het belangrijk om de morfologie te relateren met de performantie via elektrische metingen op microstructureel niveau. Scanning probe microscopie (SPM) biedt hiervoor een aantal interessante technieken om de morfologie met hoge resolutie simultaan met de lokale elektrische eigenschappen te bepalen. Scanning tunneling microscopie (STM), scanning near field optische microscopie (SNOM), elektrostatische krachten microscopie (EFM), Kelvin probe krachten microscopie (KPFM) en conductive AFM (C-AFM) zijn een aantal van de mogelijkheden.

In dit doctoraat werd gebruik gemaakt van EFM en C-AFM. Aangezien EFM een non-contact techniek is, maakt deze methode de ideale kandidaat om zachte materialen zoals organische halfgeleider te meten. In C-AFM wordt dit probleem verholpen door zachte probes te gebruiken. C-AFM is voornamelijk attractief omdat deze methode het voordeel heeft om lokale I-V profielen te bepalen en lokale verschillen in geleidbaarheid simultaan met morfologie te visualiseren. De traditionele EFM opstelling was aangepast om succesvol laterale geleidbaarheidsmetingen uit voeren terwijl de C-AFM gebruikt werd om transversaal de geleidbaarheid te meten en om de ladingstransport mechanismen te bepalen.

De standaard EFM opstelling werd succesvol aangepast om lokale laterale geleidbaarheidsmetingen uit te voeren. Voor de PPV:PCBM film werd een laterale niet-lineaire potentiaal vermindering geobserveerd, wat betekent dat de ladingsdragende film zich gedraagt als een diffuse geleider. Aan de goudcontacten is het potentiaalverschil klein waardoor er een lage injectie barrière is tussen het goudcontact en de ladingsdragende film. Lokale voltage variaties konden gerelateerd worden aan lokale geleidsbaarheidsverschillen in de film. Een grotere elektrische geleidbaarheid is gevonden in de PCBM clusters in vergelijking met het omringende mengsel. Aangezien dat de focus in deze thesis gelegd werd op het P3HT:PCBM mengsel, werd ook hierop laterale EFM toegepast. Een niet-lineaire potentiaal vermindering werd ook hier geobserveerd en een kleine injectie barrière is aanwezig tussen het goud en de respectievelijke film. Kleine lokale potentiaal variaties tezamen met de grote homogeniteit van de film maakte het moeilijk om de elektrostatische eigenschappen van deze film te analyseren. Bovendien konden de grote PCBM naalden niet geanalyseerd worden als gevolg van de te grote hoogteverschillen en de significante bijdrage ervan op het EFM signaal.

In parallel met de EFM metingen, werd C-AFM gebruikt om de transversale geleidbaarheidseigenschappen van dezelfde PPV:PCBM en P3HT:PCBM films te meten. Eerst en vooral was het noodzakelijk om het effect van scannen op de film na te gaan aangezien dat C-AFM opereert in contact mode. Door gebruik te maken van zachte probes werd topografische schade vermeden. Lokale elektrische schade werd echter wel geobserveerd, waarschijnlijk afkomstig van elektrochemische effecten aan de tip-staal contacten. Daarom werden metingen altijd op een nieuw gebied uitgevoerd. Eerst werd de MDMO-PPV:PCBM film gemeten. Een zeer lage stroom (in de orde van pA) werd hier gedetecteerd en rond de PCBM clusters werd een gebied van hogere weerstand gemeten. Door de spanning gradueel te veranderen kon er besloten worden dat het ladingstransport voornamelijk bepaald wordt door gaten geleiding in MDMO-PPV in het positieve spanningsbereik en elektronen geleiding in PCBM in het negatieve spanningsbereik. P3HT:PCBM films werden eveneens bestudeerd. Hier werd een grotere geleidbaarheid gemeten in vergelijking met de MDMO-PPV:PCBM film. De kleine geleidbaarheidsverschillen gevonden in de P3HT:PCBM film werden toegeschreven aan lokale verschillen in kristalliniteit van het P3HT. Verder werd C-AFM toegepast op puur P3HT om de ladingstransport mechanismen te onderzoeken. Hiervoor is het noodzakelijk om lokale I-V profielen op te meten. Aangezien het meten van lokale I-V profielen door middel van C-AFM inaccuraat is gezien de lage signaal tot ruis verhouding werd een nieuwe methode ontwikkeld om de signaal tot ruis verhouding te verbeteren. Deze nieuwe methode bestaat erin om gedurende het scannen de spanning geleidelijk aan te vermeerderen en lokaal de stroom te meten. Van dit stroom signaal wordt lijn per lijn het gemiddelde genomen om zo een “lokaal” I-V profiel te verkrijgen met een betere signaal tot ruis verhouding. Uit dit lokaal I-V profiel, verkregen voor puur P3HT, kon er afgeleid worden dat het ladingstransport in P3HT voornamelijk geleid wordt door space charge limited current (SCLC). Uit deze metingen werd een mobiliteit van 6.2*10-4 $cm^2/V.s$ berekend. Voor de berekening werd een sfeer/sfeer interactie model gebruikt om zo de geometrie van de tip-staal interactie te beschrijven. Verdere modelering zal nodig zijn om de mobiliteit te bepalen uit C-AFM metingen aangezien dat het contact waarmee de I-V curves opgenomen wordt ideaal beschouwd kan worden als een halve sfeer/plaat contact. In tegenstelling tot EFM waar de grote hoogteverschillen van de PCBM naalden een obstructie waren, vormt dit voor C-AFM metingen geen probleem. Significante geleidbaarheidsverschillen werden gedetecteerd tussen het mengsel, de PCBM naald en de PCBM depletie regio dewelke de PCBM naald omringt. Uit het C-AFM beeld kon er afgeleid worden dat de PCBM depletie regio zich veel verder uitstrekt dan wat er op het eerste zicht kon besloten worden uit het topografie beeld. De geleidbaarheid is het hoogste in de PCBM depletie regio en daalt gradueel naarmate er verder van de PCBM naald wordt gegaan hetgeen overeenkomt met een graduele toename van PCBM. De PCBM depletie regio vertoonde een hogere geleidbaarheid. Hier eveneens werden “lokale” I-V profielen opgemeten om de ladingstransporten in de verschillende gebieden te onderzoeken. Ongeacht de polariteit van het voltage, wordt het ladingstransport voornamelijk bepaald door de gaten geleiding in P3HT. Er werd in dit hoofdstuk aangetoond dat zowel EFM als C-AFM krachtige en complementaire technieken zijn om simultaan de lokale geleidbaarheid en de morfologie te meten voor nanogestructureerde materiaalsystemen, en organische mengsels in het bijzonder.

Publications

A. *International Publications*

“Tuning the dimensions of C-60-based needlelike crystals in blended thin films”, **A. Swinnen**, I. Haeldermans, M. vande Ven, J. D'Haen, G. Vanhoyland, S. Aresu, M. D'Olieslaeger, J. Manca, ADVANCED FUNCTIONAL MATERIALS 16 (6): 760-765 APR 4 2006.

“Dual crystallization behaviour of polythiophene/fullerene blends”, **A. Swinnen**, I. Haeldermans, P. Vanlaeke, J. D Haen, J. Poortmans, M. D Olieslaeger, J.V. Manca, THE EUROPEAN PHYSICAL JOURNAL, **36**, 2006, 251-256.

“Elucidating the aspect of “phase separation” in organic blends by means of thermal analysis”, **A. Swinnen**, J. Zhao, G. Van Assche, D. Vanderzande, M. D’Olieslaeger, J.V. Manca, B. Van Mele, SPIEE proceeding, 2007, San Diego, *accepted.*

“High resolution morphological and electrical characterisation of organic bulk heterojunction solar cells by scanning probe microscopy”, O. Douhéret, **A. Swinnen**, S. Bertho, I. Haeldermans, J. D’Haen, M. D’Olieslaeger, D. Vanderzande, J.V. Manca, PROGRESS IN PHOTOVOLTAIC, *accepted*.

“NMR study of the nanomorphology in thin films of polymer blends used in organic PV devices: MDMO-PPV/PCBM”, R. Mens, P. Adriaensens, L. Lutsen, **A. Swinnen**, S. Bertho, B. Ruttens, J. D'Haen, J. Manca, T. Cleij, D. Vanderzande, J. Gelan, Journal of Polymer Science Part A: Polymer Chemistry, **46**, 2008, 138-145.

“High resolution electrical characterization of organic protovoltaic blends”, O. Douhéret, **A. Swinnen**, M. Breselge, I. Van Severen, L. Lutsen, D. Vanderzande, J. Manca, MICROELECTRONIC ENGINEERING, **84**, 2007, 431.

“Influence of thermal ageing on the stability of polymer bulk heterojunction solar cells”, S. Bertho, I. Haeldermans, **A. Swinnen**, W. Moons, T. Martens, L. Lutsen, D. Vanderzande, J.V. Manca, A. Senes and A. Bonfiglio, SOLAR ENERGY MATERIALS AND SOLAR CELLS, *in press*, 2006.

“Local electrical characterization of organic photovoltaic blends”, **A. Swinnen**, A. Volodin, M. P. Chowdhury, O. Douhéret, K. Vandewal, M. D’Olieslaeger, J. Manca, C. Van Haesendonck, THIN SOLID FILMS, *submitted.*

"P3HT/PCBM Bulk Heterojunction Solar Cells: Relation between Morphology and Electro-Optical Characteristics.", P. Vanlaeke, **A. Swinnen**, I. Haeldermans, G. Vanhoyland, T. Aernouts, D. Cheyns, C. Deibel, J. D´Haen, P. Heremans, J. Poortmans, J. V. Manca, SOLAR ENERGY MATERIALS AND SOLAR CELLS 90 (14): 2150-2158 SEP 6 2006

"Local electrical characterisation of organic photovoltaic blends by conductive atomic force microscopy", O. Douhéret, **A. Swinnen**, M. Breselge, K. Vandewal, L. Goris, L. Lutsen and J. Manca, APPLIED PHYSICS LETTERS 89 (3): Art. No. 032107 JUL 17 2006

"Optical absorption by defect states in organic solar cells ", L. Goris, A. Poruba, A. Purkrt, K. Vandewal, **A. Swinnen**, I. Haeldermans, K. Haenen, J.V. Manca, M. Vanecek , JOURNAL OF NON-CRYSTALLINE SOLIDS 352 (9-20): 1656-1659 JUN 15 2006

B. Oral presentations

"Influence of post-production annealing on the morphology of polythiophene/fullerene bulk heterojunction solar cells", A. Swinnen, P. Vanlaecke, I. Haeldermans, J. D'Haen, G. Vanhoyland, M. D'Olieslaeger, J.V. Manca, J. Mullens, J. Poortmans, and D. Vanderzande, submitted to ICOE05, Eindhoven (NL), 21/06/05-24/06/05

"Local electrical characterization of organic photovoltaic blends", A. Swinnen, A. Volodin, M. P. Chowdhury, O. Douhéret, K. Vandewal, M. D'Olieslaeger, J. Manca, C. Van Haesendonck, E-MRS07, Strasbourg (FR), June '07

C. Poster

"Influence of preparation and post-annealing treatment on the morphology of Bulk Hetero-Junction Organic Solar Cells", **A. Swinnen**, P. Vanlaecke, J. D'Haen, J. Poortmans, M. D'Olieslaeger and J.V. Manca, Seeing at the nanoscale II, Grenoble (FR), 13/10/04-15/10/04

"How stable is the morphology of polythiophene/fullerene bulk heterojunction solar cells?", **A. Swinnen**, P. Vanlaeke, I. Haeldermans, J. D'Haen, G. Vanhoyland , J. Poortmans, D. Vanderzande, J. Mullens, M. D'Olieslaeger and J. Manca, Bologna (It.), 29/06/05-30/06/05

“Dual crystallization behaviour of polythiophene/fullerene blends”, **A. Swinnen**, I. Haeldermans, J. D’Haen, M. D’Olieslaeger and J. V. Manca, ECHOES06, Paris (FR), 28-30/06/06

“Elucidating the aspect of “phase separation” in organic blends by means of thermal analysis”, **A. Swinnen**, J. Zhao, G. Van Assche, D. Vanderzande, M. D’Olieslaeger, J.V. Manca, B. Van Mele, SPIEE, San Diego (US), 27-20/08/07

D. Others

Cover of Advanced Functional Materials 16 (6) 2006

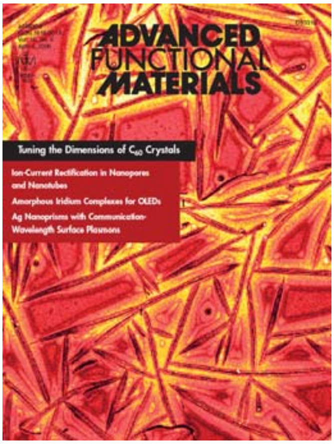

Calender of Materials Today 2006, month February

FEBRUARY

M	T	W	T	F	S	S	M	T	W	T	F	S	S
		1	2	3	4	5	6	7	8	9	10	11	12
13	14	15	16	17	18	19	20	21	22	23	24	25	26
27	28												

In the study of bulk heterojunction solar cells, the P3HT:PCBM system is a hot topic. When this blend is annealed at high temperatures (125°C and above) the PCBM starts to crystallize and forms large 'needles'. The crystallization of PCBM is extremely fast - after 5 mins structures of 100 μm begin to appear. In this optical microscopy image of PCBM crystals, height differences in the film result in beautiful color differences.

Ann Swinnen
Instituut voor Materiaalonderzoek,
Limburgs Universitair Centrum,
Wetenschapspark 1, 3590 Diepenbeek,
Belgium

materialstoday

www.materialstoday.com

XX

“Zon in een cel”, **A. Swinnen**, Knack, 12 juli 2006

ZONNECEL
Koolstofvoetballen verhogen de efficiëntie van zonnecellen.

MATERIALEN

Zon in een cel

PLASTIC ZONNECELLEN WORDEN ALMAAR EFFICIËNTER.

Zonnecellen zijn nog altijd niet efficiënt genoeg om écht rendabel te zijn. Nochtans wordt er veel hoop gesteld in deze vorm van energievoorziening, want de zon blijft maar stralen. Zolang de omzetting van licht in elektriciteit echter duurder blijft dan 0,1 euro per kilowattuur, zal zonne-energie niet kunnen concurreren met klassieke energieopwekking.

Er moeten dus nieuwe zonnecellen gemaakt worden, met nieuwe halfgeleiders, die goedkoop als een dunne film op grote oppervlakken kunnen worden aangebracht, en er zonnecel spelen met een efficiëntie in de energieomzetting van 10 procent en een kostprijs van minder dan 50 euro per m^2. Dat zijn een heleboel vereisten.

Ann Swinnen en haar collega’s van het Instituut voor Materiaalonderzoek aan de Universiteit Hasselt lijken echter, volgens hun verslag in het vakblad *Advanced Functional Materials*, goed op weg om dit doel te halen. Ze werken met plastic zonnecellen, die uit een mengsel van gatengeleidende polymeren en elektronengeleidende moleculen bestaan. Als molecule wordt een oplosbaar derivaat van zogenaamde ‘buckyballs’ gebruikt: een vorm van koolstof met zestig atomen die als een voetbal georganiseerd zijn.

Het geheel wordt opgewarmd, waardoor het een zonnecel wordt met een rendement van 4 tot 5 procent. Dat is nog altijd maar de helft van de kleine zonnecellen in, bijvoorbeeld, rekenmachines, maar de wetenschappers zijn op de goede weg.

Zodra ze voldoende inzicht krijgen in de organisatie van de microstructuur van deze film kunnen ze verbeteringen aanbrengen.

Abbreviations and symbols

α	absorption coefficient
β	heating rate
ε_o	vacuum permittivity
ε_r	dielectric constant
ϕ	work function
η	power conversion efficiency
λ	wavelength
λ_{max}	wavelength at maximal absorption
μ	charge carrier mobility
θ	angle
ω	angular frequency
Ω	frequency

A	amplitude
A_{HF}	amplitude of the cyclic heat flow
A_{HR}	amplitude of the cyclic heating rate
AFM	atomic force microscopy
AM	amplitude modulation
A.M. 1.5	air mass 1.5 solar spectral irradiance
BF	bright field
C	1) concentration 2) capacitance
C_{60}	buckminsterfullerene
$c_{p,BASE}$	baseline heat capacity
$c_{p,MTDSC}$	cyclic MTDSC heat capacity
C-AFM	conductive atomic force microscopy
CN-PPV	poly(cyano-phenylene vinylene)
CPD	contact potential difference
d	1) film thickness 2) lattice plane spacing
DF	dark field
DI	de-ionized
DSC	differential scanning calorimetry
E	electrostatic field
E_f	Fermi-level
E_g	bandgap
E_{vac}	vacuum level
EFM	electrostatic force microscopy
f	resonance frequency
F	electrostatic force
FF	fill factor
FIB	focussed ion beam

FM	frequency modulation
HF	heat flow
HOMO	highest occupied molecular orbital
HR-SEM	high resolution scanning electron microscopy
I_{max}	current at maximum power point
I_{sc}	short-circuit current
IPA	isopropyl alcohol
ITO	indium tin oxide
J	current density
J_{sc}	short-circuit current density
KPFM	kelvin probe force microscopy
L	thickness
LiF	lithium fluoride
LUMO	lowest unoccupied molecular orbital
MEH-PPV	poly(2-methoxy-5-(2'-ethyl-hexyloxy)-1,4-phenylene vinylene)
MDMO-PPV	poly(2-methoxy-5-(3'-7'-dimethyloctyloxy)-p-phenylenevinylene)
MgPc	magnesium phtalocyanines
MIBK	methylisobutylketone
MO	molecular orbital
MTDSC	modulated temperature differential scanning calorimetry
Mw	molecular weight
OECD	organization for economic co-operation and development
PA	poly(acetylene)
PAT	poly(alkyl-thiophene)
P3HT	poly-(3-hexylthiophene)
PCBM	(6,6)-phenyl-C_{61}-butyric-acid
PEDOT	poly(3,4-ethylenedioxythiophene)
$(PEO–OC_9)$–PPV	poly(2-(*n*-nonyloxy)-5-(triethoxymethoxy)-1,4-phenylene vinylene)
PEO-PPV	poly(2-methoxy-5-(triethoxymethoxy)-l,4-phenylene vinylene)
P_{light}	irradiated light power
P_{max}	maximum power point
PMMA	polymethyl methacrylate
PPV	poly(para-phenylenvinylene)
PSS	polystyrenesulphonate
$P_{theoretical\ max}$	theoretical maximum power
PV	photovoltaic
q	the magnitude of the elementary charge
Q	heat
rpm	rotation per minute

r	thickness
R	1) thermal resistance 2) reference
R_{sheet}	sheet resistance
S	sample
SAED	selected area electron diffraction
SCLC	space charge limited current
SEM	scanning electron microscopy
t	time
T	temperature
T_c	crystallization temperature
T_g	glass temperature
T_m	melting temperature
TEM	transmission electron microscopy
TUNA	tunnelling AFM
V	voltage
V_{bi}	build-in voltage
V_{max}	voltage at maximum power point
V_{oc}	open circuit voltage
V_{PD}	contact potential difference
V_s	surface potential
XRD	X-ray diffraction
z	the direction normal to the sample surface

1. Introduction: organic blends in photovoltaics

In this first chapter the relevance of the use of solar cells in general and in particular of organic solar cells is described. The significant parameters for solar cell device performances are discussed followed by an outline of the historic evolution in photovoltaics and the evolution of organic solar cells in particular. From single layer up to bilayer and bulk heterojunction solar cell working principles are discussed with an emphasize on morphology. Subsequently, the importance of morphology in these devices is described and a literature survey of the parameters influencing the morphology is also proposed: solvent choice, blending ratio, post production annealing and casting parameters. At the end of the chapter the aim of this thesis is pointed out and the outline of this thesis is given.

1.1. Why solar energy?

The increase in world population, from 1.5 billion at the beginning of the 20th century to 6 billion people at the end, requires more energy. According to the Organization for Economic Co-operation and Development (OECD) the energy consumption in 2003 increased more than 16% compared to 1993.[1] In 2003, 77% of all the energy production was supplied by fossil fuels (i.e. gas, oil and coal).[2] Major drawback of energy production using fossil fuels, is the production of large amount of CO_2 causing global warming. Additionally, fossil fuels are not inexhaustible. One way to overcome these problems is the use of nuclear power. Nuclear waste and the controversy of nuclear power makes this energy source a doubtful substitute. A second way is the use of renewable energy: biomass, wind energy, water power, geothermal energy and solar energy. However, the limited production of energy makes it yet not suitable for large-scale power generation. Still, they are bound to become the energy for the 21st century. If photovoltaic power is compared to other renewable energy sources such as wind power, water power, and even solar thermal power, it presents some obvious advantages. First, wind and water energy sources rely on turbines to turn generators to produce electricity. Turbines and generators have moving parts that can break down and require maintenance. Even solar thermal energy needs a turbine or other mechanical devices to change the heat energy of the sun into mechanical energy for a generator to produce electric power. Photovoltaic (PV) power, by contrast, is generated directly from the sun. PV systems have no moving parts and require virtually no maintenance.[3] Additionally, PV power is applicable at all places on earth.[4] In the next paragraph the parameters determining the solar cell performance are discussed.

1.2. Characteristic solar cell parameters

The performance of a solar cell can be described by several parameters, calculated from current-voltage (I-V) profiles. The external voltage applied to the solar device is plotted in function of the resulting external electrical current. Figure 1.1 shows a typical I-V curve under illumination. The power delivered by a solar cell can be described as the product of the current with the voltage, which can be found in the fourth quadrant of the I-V profile. The point at which the power reaches its maximum is called the maximum power point P_{max} and is given by:

$$P_{\max} = I_{\max} V_{\max} \qquad \textit{equation 1-1}$$

, and equal to the full line squared area in Figure 1.1.

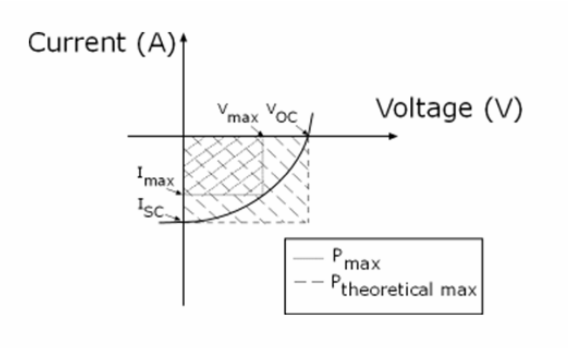

Figure 1.1: Typical I-V curve of an illuminated solar cell. The most important parameters like open circuit voltage (V_{oc}), short circuit current (I_{sc}) determining the theoretic maximum power point ($P_{theoretical\ max}$) and maximum current (I_{max}), maximum voltage (V_{max}) determining the maximum power point (P_{max}) are indicated on the plot.

From the I-V plot two important values can be determined, open-circuit voltage V_{oc} and short-circuit current I_{sc}. The open-circuit voltage (V_{oc}) is the voltage required so that no external current is flowing trough the illuminated device. The short-circuit current (I_{sc}) is the amount of external current when no external voltage is applied to the illuminated device. Since, the short-circuit current is depending on the device surface, the short-circuit current density J_{sc}, is often used. J_{sc} is equal to the short-circuit current divided by the active area A of a solar cell. In Figure 1.1, it is seen that an additional rectangle (dashed area) can be obtained with V_{oc} and I_{sc}. This area represents the theoretical maximum power P_{max} that can be delivered. The fill factor (FF) describes the ratio of the actual maximum power to the theoretical maximum power, hence indicating the degree of rectangle of the I-V plot:

$$FF = \frac{P_{\max}}{P_{theoretical \max}} = \frac{I_{\max}\, V_{\max}}{I_{SC}\, V_{OC}} \qquad \text{equation 1-2}$$

If the fill factor equals to one, a perfect rectangular shape of I-V curve is seen. All these parameters serve to describe how well a solar cell can convert light into current, i.e. to determine the efficiency η of a solar cell. The efficiency is described by the ratio between the maximum power delivered and the irradiated light power P_{light}:

$$\eta = \frac{P_{\max}}{P_{light}} = \frac{I_{\max}\, V_{\max}}{P_{light}} = \frac{I_{SC}\, V_{OC}\, FF}{P_{light}} \qquad \text{equation 1-3}$$

From this equation it is clear that the efficiency of solar cells are dependant on the irradiated light power. In order to compare different solar cells standardized irradiated light should be used. The so-called standard solar illumination is chosen Air Mass (A.M.) 1.5 spectrum, see Figure 1.2. The total value is scaled to a value of 1000 W/m².

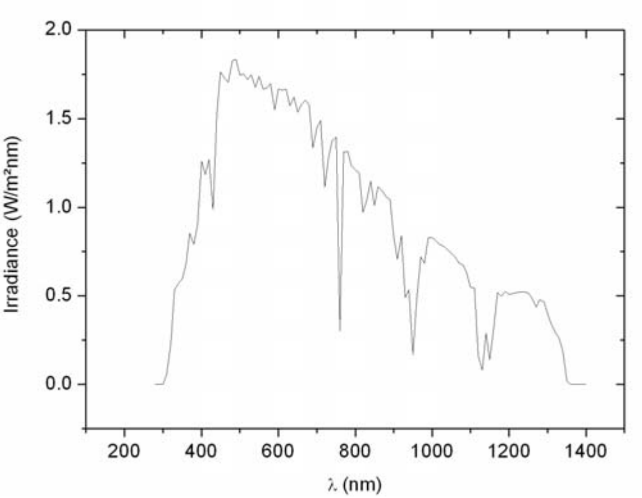

Figure 1.2: The AM 1.5 solar spectrum.

1.3. Evolution in photovoltaics

In 1839, Edmond Becquerel was the first to observe the photovoltaic effect, i.e. the conversion of light into electricity, during illumination of two silver coated platinum electrodes immersed in electrolyte.[5,6] Subsequently, Adams and Day discovered the photovoltaic effect in solid state selenium.[7] Still the efficiencies remained too low. In was only in 1941 with the discovery of silicon solar cells by Russell Ohl that a great breakthrough was realized.[8] Efficiencies of 6% were obtained with this material in 1954, making it possible to commercialize it.[9] The elevated cost price, 300 $ per Watt, limited the use of solar cells to space applications in the 50s and 60s.[10] Simultaneously, p-n junctions of cadmium sulphide, gallium arsenide, indium phosphide and cadmium telluride were also produced and yielded solar efficiencies of 6%. It was not until the 1970s, with the oil crisis, that huge investments started to be done in the research of solar cells. Alternative materials such as polycrystalline Si, amorphous Si and other "thin film" materials and organic conductors were explored. Higher efficiencies were obtained by multiple bandgap and tandem designs. Despite the significant evolution of efficiencies and designs (see Figure 1.3), commercial solar cells did not emerge until the 90s. Nowadays, commercially available solar cells still remain uncompetitive compared to traditional energy sources, because of high production costs. Cost-reduction is therefore the major motivation to move towards new type of materials such as organic molecules.

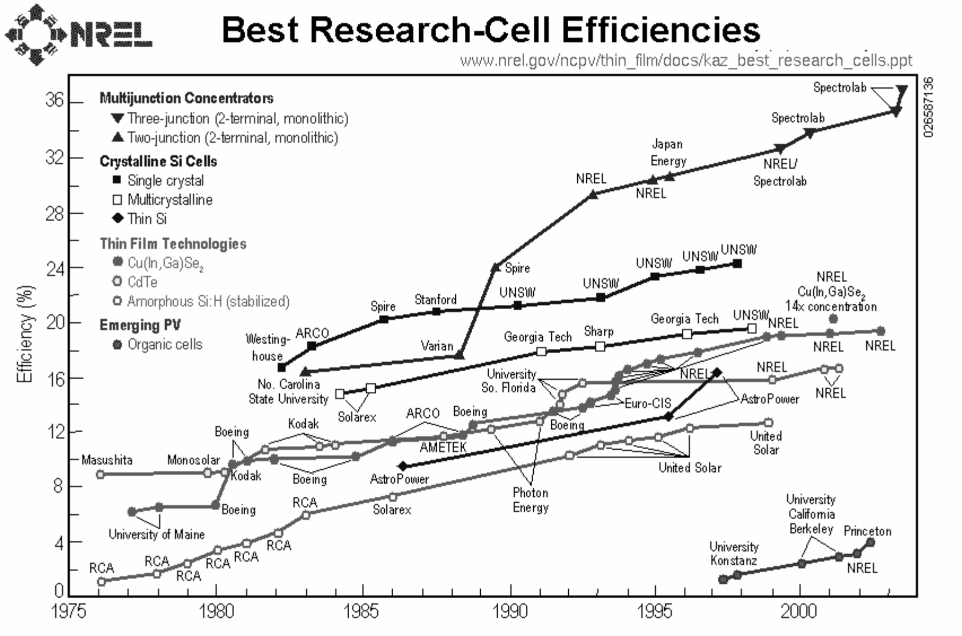

Figure 1.3: Overview of evolution of best research-cell efficiencies. Reprinted from.[11]

1.4. Organic photovoltaics

In the next paragraphs a historic overview is given about the evolution of organic photovoltaics. First a theoretical statement will be made concerning organic conjugated molecules. Secondly, the evolution of organic photovoltaic devices will be discussed. Starting from single layer devices, over bilayer devices towards the creation of bulk heterojunction solar cells. The working principles of these devices and the evolution of materials used will also be presented and the impact of morphology of the photovoltaic component of the device will be pointed out.

1.4.1. Organic conjugated molecules

Typically conjugated π-electron system molecules or polymers are used in organic photovoltaics, and consist of alternating single and double bonds between the carbon atoms in their skeleton structure. Single bonds are referred to as σ-bonds, while double bonds contain a σ-bond and a π-bond. The electronic configuration of a carbon atom in its ground state is $1s^2 2s^2 2p^2$. Carbon has four valence electrons (electrons that can be bounded): two electrons in the 2s orbital and two electrons in the 2p orbitals, shown in the left part of Figure 1.4. In excited state the orbitals are in different energy levels (2s and 2p). As a result, orbitals will mix to form new orbitals. This process is called hybridization. Hybridization will increase the overlap between orbitals, resulting in lower energy and thus more stable molecules. In carbon the s and p orbitals can rearrange to form sp, sp^2 and sp^3 hybrid orbitals. The sp^3 hybridization can be found in methane (CH_4). The four sp^3 orbitals have the same shape and energy, therefore they will be arranged in a tetrahedral structure, as shown in Figure 1.4 (top). Four single bounds (σ–bounds) can thus be formed with neighbouring atoms. A double bound between two carbon atoms can be formed due to a sp^2 hybridization. A sp^2 hybridization, found in ethylene (H-C=C-H), of a carbon atom will result in three sp^2 orbitals and one p_Z orbital. The three sp^2 orbitals are constructed out of one s orbital and two p orbitals, coplanar and oriented 120° relative to each other (see Figure 1.4 middle). The chemical bonds formed by sp^2 hybrids will be σ-bonds and localized between the bonding carbon atoms and/or hydrogen atoms. The fourth orbital p_Z does not hybridize and is perpendicular to the plane formed by the hybrid orbitals. The p_Z orbitals of the carbon atoms will overlap sidewise, which leads to the formation of so-called π–bonds.[12] In a sp hybridization of a carbon atom, present in acetylene (H-C≡C-H), two sp orbitals are formed (again used for two σ bonds) and a p_Y and p_Z orbital remain unhybridized. The sp orbitals of both carbon atoms will be used for the σ-bonds (C-C and C-H bonding) while the p atomic orbitals will overlap and form double π–bonds between the two carbon atoms.

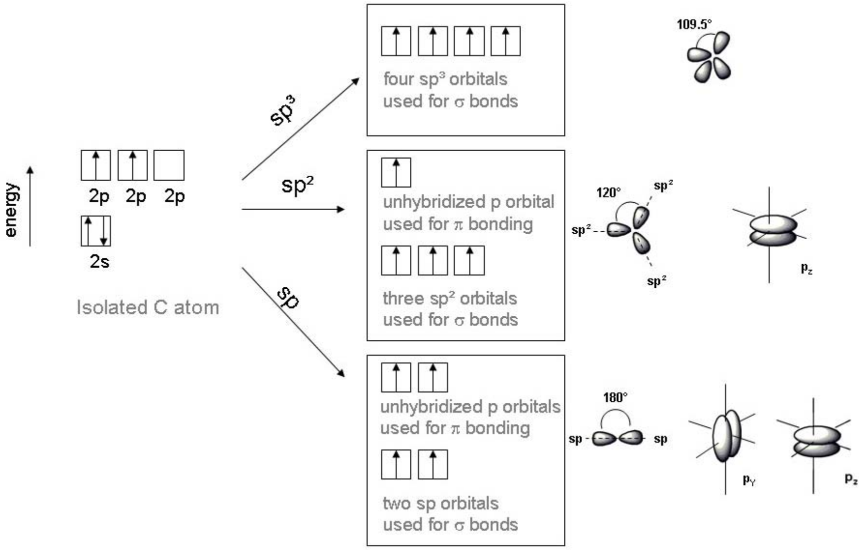

Figure 1.4: Different hybridization processes possible for an isolated carbon atom with corresponding energy levels, possible σ and π bounds and schematic of the atomic orbitals.[13]

In the atomic orbital theory or valence bond theory, described above, an atomic orbital is described as a region of space around an atom where an electron is likely to be found. On the other hand, the molecular orbital (MO) theory describes the region of space in a molecule where an electron is likely to be found. To explain the MO theory ethylene will be used, since it is the most widespread polymer. The first principle of molecular orbital theory states that the number of molecular orbitals produced is always equal to the number of atomic orbitals brought by the atoms that have been combined. Since orbitals are electron waves, the formulation of a molecular orbital can be seen as an interference of two electron waves, one from each atom of the bounded pair. The interference can be constructive, giving a bonding MO (σ or π), or destructive, rendering an antibonding MO (σ^* or π^*). The second and third principle of the MO theory states that the bonding MO (σ or π) is lower in energy than the parent atomic orbitals, the antibonding orbital (σ^* or π^*) is higher in energy, and the electrons of the molecule are assigned to orbitals of successively higher energy. Considering now ethylene, four electrons are available to form the double bond between both carbon atoms. The σ and π MO orbitals are filled while the antibonding MO orbitals σ^* and π^* remain empty, shown in Figure 1.5. Since the energy of the electrons in σ and π MO is lower than in the parent atoms, the molecule is stable. Having a look at the energy diagram in Figure 1.5, it is seen that π is the highest occupied molecular orbital (HOMO) and π* is the lowest unoccupied molecular orbital (LUMO).

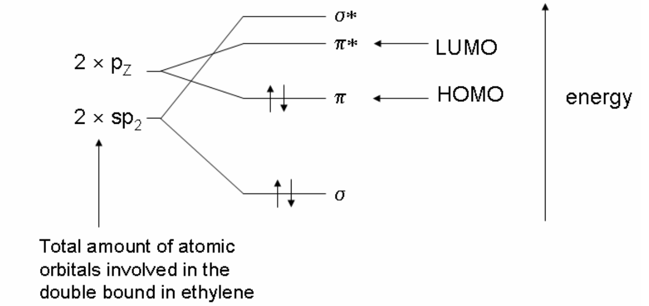

Figure 1.5: Molecular orbital energy level diagram for the double bound between carbon atoms in C_2H_4.

In a conjugated polymer (like polyacetylene), a large number of carbon atoms are connected. By increasing the amount of carbon atoms, the amount of atomic orbitals will increase and consequently the amount of molecular orbitals. Each new molecular orbital will have a different energy, but similar to the original ethylene molecular orbital, as shown in Figure 1.6. The molecular orbitals will be spread, or delocalized, over many carbon atoms, lowering the overall energy of the molecule and blend into a band of molecular orbitals. The collection of empty π* MO is called the conduction band while the collection of the filled π MO is called the valence band. The lower limit of the conduction band corresponds to the LUMO, while the upper limit of the valence band correspond to the HOMO. The energy difference between HOMO and LUMO is called the bandgap, E_g. Depending on the magnitude of the bandgap, the conductivity properties of a material can be derived, i.e. the higher the bandgap the more insulating the material.

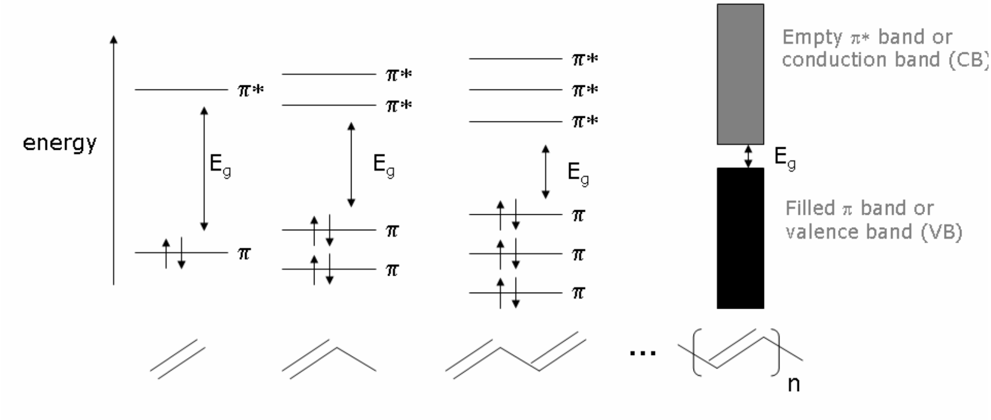

Figure 1.6: Effect of increased conjugating length on the π to π energy gap. With large amount of carbons present the energy gap still remains due to the Peierls distortion. Only the π and π* molecular orbitals are shown.*

1.4.2. Single layer devices

In the beginning of the 20th century, antracene was the first organic substance for which photoconductivity was observed.[14,15] It was only by 1959 that a single crystal of anthracene (Figure 1.7 (C)) was used in a device.[16] Simultaneously, experiments were performed with magnesium phtalocyanines (MgPc) (chemical structure shown in Figure 1.7 (A)).[17] It was the research on Chlorophyll-a (Chl-a) (chemical structure shown in Figure 1.7 (B)) that revealed the great importance of using electrodes with different work functions.[18-20] Nevertheless, only 0.1% power conversion efficiency could be reached with this type of device. During the 70's, with the discovery of high conductivity in doped poly(sulphur nitride) and poly(acetylene) (PA) (Figure 1.7 (D,E)), conjugated polymers became possible candidates for single layer devices.[21] A. J. Heeger, A. G. MacDiarmid and H. Shirakawa found in 1977 that by oxidation with chlorine, bromine or iodine vapour, PA films could be doped and thus could be made highly conductive.[22,23] Later, additional semiconducting polymers such as poly(alkyl-thiophenes) (PATs, Figure 1.7 (F)) and poly(p-phenylene vinylene) (PPV, Figure 1.7 (G)) have also been tested for single layer devices. The unconvincing results (very low efficiencies of ~0.1% under white light illumination) were shown to be related to the poor design of the device rather than the material themselves, considering the significant breakthrough they both have been able to provide in bulk heterojunction solar cells.[24,25]

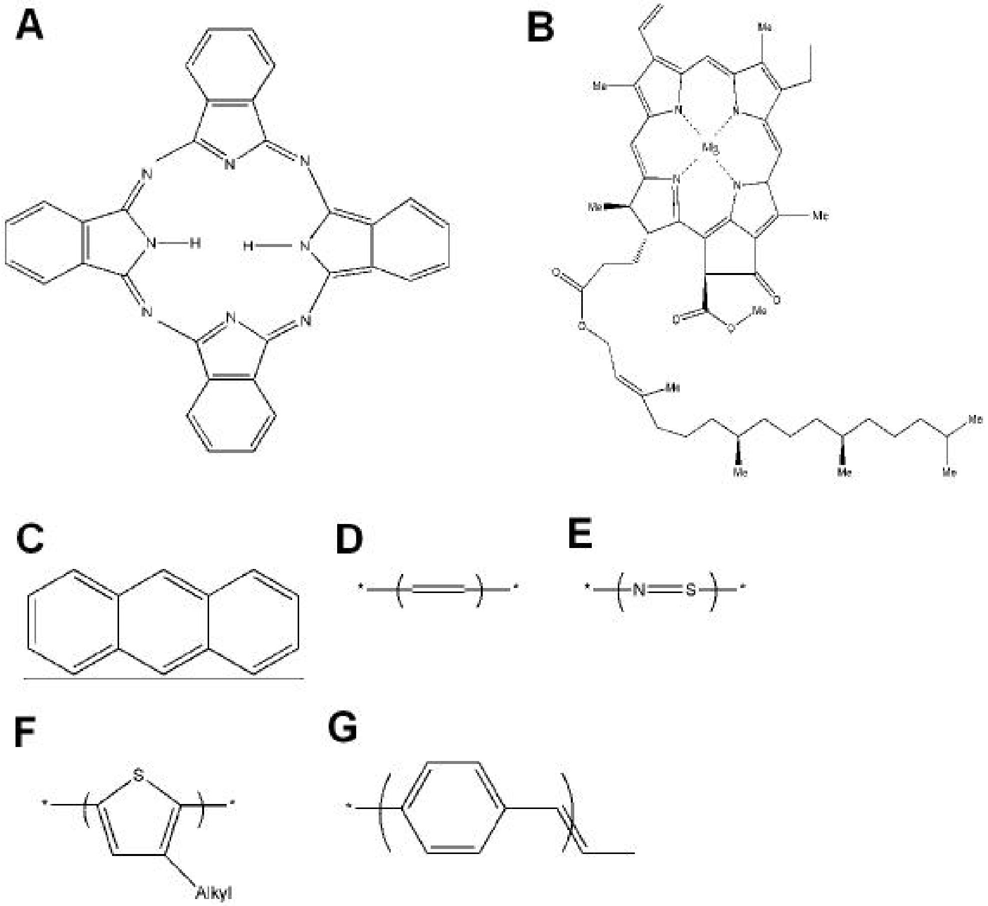

Figure 1.7: Chemical structure of phtalocyanine (A), Chl-A (B), anthracene (C), polyacetylene (D), poly(sulphur nitride) (E), poly(3-alkyl-thiophene) (F) and poly(p-phenylene vinylene) (G).

In Figure 1.8 a schematic of a single layer device is depicted, where an organic layer is sandwiched between two different electrodes (anode and cathode) obtaining a planar configuration. Incoming light will be absorbed by the organic layer, exciting an electron from the HOMO to the LUMO, creating an exciton (bounded electron hole pair). The resulting meta-stable electron-hole pairs may still be bound by Coulomb interactions. Asymmetrical work functions, i.e. the energy difference between the Fermi level[1] and the vacuum level, of the electrodes (Φ_{anode} and $\Phi_{cathode}$) results in an electric field causing exciton dissociation. In most cases the build-in potential induced by this electric field is not sufficient to break up the photogenerated exciton. Instead, the exciton diffuses towards the contact where it dissociates in separate charges because of the difference in electron affinity between the organic layer and the contact or recombines at the contact. Since, exciton diffusion lengths are typically 1-10 nm, this limits charge carrier generation in such devices. Therefore, low exciton dissociation was one of the reasons for the too low efficiency in single layer devices.

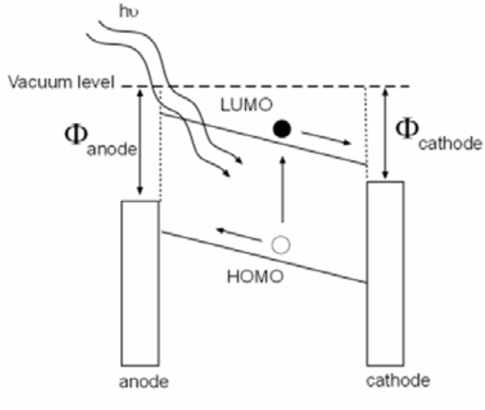

Figure 1.8: Schematic of a charge generation process in a single layer device.

1.4.3. Double layer devices

A significant breakthrough was achieved when Tang *et al.* introduced the bilayer concept in which two organic layers (see Figure 1.9 (a)), a p-type phtalocyanine derivative and an n-type perylene derivative are sandwiched between electrodes, and resulted in a 1% efficiency device.[26] This significant efficiency increase was attributed to the high dissociation rate of excitons into free charges at the donor acceptor interface. This increased generation of free charges was induced by the energy level offset between donor and acceptor material.

A schematic of the charge generation process in a double layer device is depicted in Figure 1.9 (b). Incoming light is being absorbed by the donor like molecule and excites the donor molecule, resulting in the creation of excitons. The acceptor phase can also absorb light, but for simplicity only the sunlight photons that are absorbed by the donor phase are considered here.

---

[1] The Fermi Level is defined for metals as the highest occupied molecular orbital in the valence band at 0 K

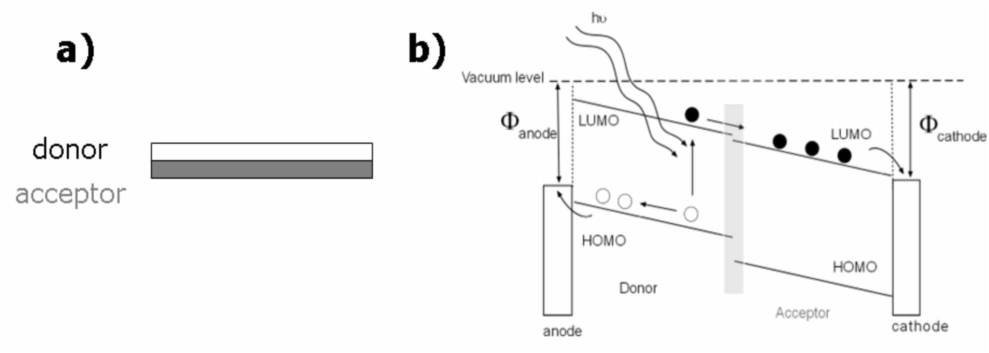

Figure 1.9: (a) Illustration of bilayer active layer and (b) schematic of charge generation in bilayer heterojunction structure.

To break the effective coulomb interaction between the bounded electron hole pairs, both materials should be chosen in such a way that the difference in electron affinity, corresponding to the HOMO and LUMO respectively, is large enough. If this condition is fulfilled, fast dissociation occurs when the exciton encounters an interface. A charge transfer is then occurring of an electron to the material with the larger electron affinity, e.g. acceptor material, and a hole to the materials with the smaller electron affinity, e.g. donor material. Subsequently, the separated free electrons (holes) are transported with the aid of an internal electric field, arising from the use of electrodes with different work functions. The electrons are transported towards the cathode and the holes are transported towards the anode.
However, the excitons can decay, yielding luminescence, if they are generated far from the interface. Thus, only excitons located within the diffusion length of the interface will contribute to the photovoltaic process. Since the exciton diffusion lengths in organic materials are much shorter, i.e. 1-10 nm, than the absorption depth of the film, this intrinsically limits the width of the effective light-harvesting layer.

From the different acceptor materials investigated for heterojunction cells, C_{60} is by far from the most used because of its high electron conductance and high electron affinity. Different conjugated polymers were used in combination with C_{60}. Sariciftci *et al.* were the first to report a bilayer cell consisting of C_{60} and a conjugated polymer, a PPV derivative.[27,28] The PPV-derivative was spincoated on an ITO coated glass substrate. The C_{60} was subsequently sublimated on top of PPV layer and covered with an evaporated Au contact. Adding the C_{60} layer, resulted in a 20 fold increase of the photocurrent indicating the strong influence of C_{60} in exciton dissociation rate. Additionally, it was found that the photocurrent is largely influence by the amount of light that reaches the interface.[29,30] The design of a bilayer solar cell is therefore based on a trade-off between the highest exciton dissociation rate and maximum light absorption, typically reached for 100 nm film. While the former would be ensured by thin semi-conducting layers, the latter promote the opposite. Yet, taking into account a much lower diffusion length of the exciton (1-10 nm), this intrinsically limits the photovoltaic efficiency of the layer, hence the performance of the cell.

1.4.4. Bulk-heterojunction solar cells

To overcome such limitations a new concept was proposed. In this system a donor and acceptor material were blended to form a 3D donor and acceptor nanoscale intermixed system. Hence the name dispersed or bulk heterojunction solar cell. While higher exciton dissociation rate is ensured by the higher density of donor acceptor interface, the charge transport is carried out by percolation paths in the materials towards the respective electrodes. An illustration of such a system is shown in Figure 1.10 (a).

Figure 1.10 (b) shows a schematic of the charge generation and transport in bulk heterojunction solar cells. The energy levels of the acceptor molecule are depicted as dashed lines while the ones from the donor molecule are shown as full lines.

Since the donor and acceptor material are mixed, the excitons created, as a consequence of the incoming photons are likely to cross a donor acceptor interface within their diffusion length in the bulk. If the length scale of the blend is similar to the exciton diffusion length, in the proximity of every generated exciton there is an interface where fast dissociation takes place, reducing the exciton decay processes dramatically. To obtain exciton dissociation, the energy level offset between donor and acceptor material still has to be large enough, as discussed with the bilayer structure. If there is a continuous pathway in each material between the interface and the respective electrodes, the light generated charges can travel along their corresponding energy levels to the electrodes. Hence, the photon-to-electron conversion efficiency and the photosensitivity is dramatically increased.

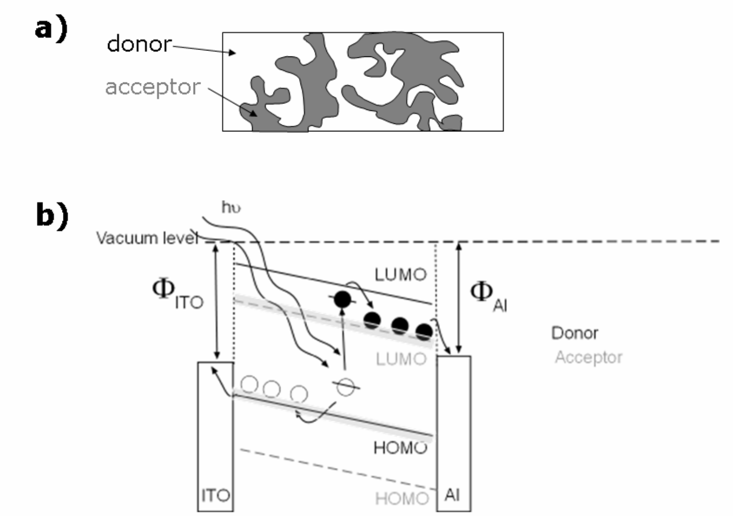

Figure 1.10: (a) Illustration of a bulk heterojunction active layer and (b) schematic of charge generation in a bulk heterojunction structure. The dashed lines are the energy levels of the acceptor, while the solid lines correspond to the energy levels of the donor material.

Several modes and techniques were used to accomplish a bulk heterojunction architecture. A major obstacle was the poor miscibility of the donor type semi-conducting polymers with the acceptor material. Therefore, fast solvent evaporation was essential to prevent phase separation of both components, accordingly spincoating was the ideal preparation method. Yu *et al.* was the first to report a dispersed polymer heterojunction, which consisted of poly(2-methoxy-5-(2'-ethyl-hexyloxy)-1,4-phenylene vinylene) (MEH-PPV), Figure 1.11 (middle), as a donor material, blended with an acceptor polymer poly(cyano-phenylene vinylene) (CN-PPV), Figure 1.11 (left).[31]

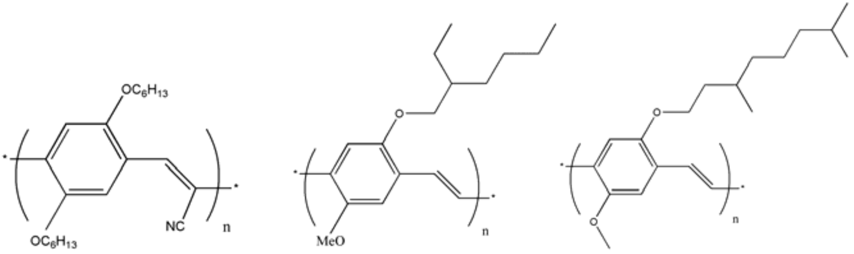

Figure 1.11: Chemical structure of CN-PPV, MEH-PPV and MDMO-PPV.

Yet, several attempts based on polymer:polymer bulk heterojunction solar cells only yielded low power conversion efficiencies.[32-34] As previously mentioned in 1.4.3, C_{60} exhibits a high electron affinity and charge carrier mobility making it an attractive material for bulk heterojunction solar cells. The use of C_{60} in bulk heterojunction solar cells was however first hampered by its low solubility in organic solvents and the tendency of C_{60} to crystallize. Therefore, a series of soluble derivatives was synthesized by Hummelen *et al.*, to improve not only solubility of the C_{60} but also miscibility with the soluble polymers used.[35] One of those C_{60} derivatives is a methanofullerene: [6-6]-phenyl C_{61} butyric acid methyl ester, better known as PCBM. The chemical structure is shown in Figure 1.12. Up to now, this is molecule is extensively used in bulk heterojunction solar cells.

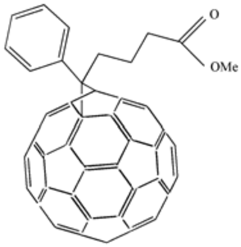

Figure 1.12: Chemical structure of [6-6]-phenyl C_{61} butyric acid methyl ester (PCBM).

Yu *et al.* was the first in 1995, to blend PCBM with MEH-PPV, resulting in a monochromatic conversion efficiency of 2.9% (illumination of 20 mW/cm²). Blends with PCBM resulted in homogeneous stable blends and PCBM concentrations up to 80% in weight could be achieved.[36] Power conversion efficiencies as high as 2%, were reported for MEH-PPV:PCBM blends under standard AM 1.5 illumination.[37] Yet not only the fullerene but also the polymer were subjected to change. By using a different PPV derivative, i.e. poly(2-methoxy-5-(3'-7'-dimethyloctyloxy)-p-phenylenevinylene) (MDMO-PPV), chemical structure shown in Figure 1.11 (right), even higher efficiencies could be obtained. By optimizing solvent choice and blending ratio of MDMO-PPV and PCBM, efficiencies as high as 2.5%, under standard AM 1.5 illumination, were first reported by Shaheen *et al.*[41] It was demonstrated that the morphology of the active layer plays a significant role in the performance of these bulk heterojunction solar cells. Later, other groups reported similar results and efficiencies reaching 3% for MDMO-PPV:PCBM material system.[38,39] Finally Munters *et al.* found by alternating the synthesis route of MDMO-PPV that the efficiency of the cell would be influenced, due to different chain defects in the polymer.[39] Both Munters *et al.* and Shaheen *et al.* therefore pointed out that the process of optimization of the performances of a cell is compelled to a better control and understanding of the mechanism driving the morphology of the blend.

1.5. Influence of morphology

Yang and Heeger were the first to study the morphology of the active layer of a bulk heterojunction solar cell based on a conjugated polymer and C_{60}.[40] Their detailed Transmission Electron Microscopy (TEM) study on different blend ratios revealed the presence of phase separated regions, resulting in nanoscale crystalline C_{60} regions. Further Shaheen *et al.*, specifically demonstrated the influence of morphology on the efficiency of solar cells.[41] A solar cell efficiency increase of 1.6% (from 0.9% to 2.5%) was obtained by changing the solvent from toluene to chlorobenzene. Chlorobenzene based spincoated blends, yielded smaller phase separated regions compared to the toluene casted ones, exhibiting an increase in interface area thus influencing solar cell properties. This research was the onset for several studies in which the different parameters influencing the morphology were explored: solvent choice, blending ratio, casting parameters and post-production annealing treatments. In the next paragraphs a thorough overview of the latest investigations is proposed.

1.5.1. Solvent choice

In the initial work of Shaheen *et al.* MDMO-PPV:PCBM 1:4 blended films from toluene solution were compared with chlorobenzene casted ones. While a 0.9 % power conversion efficiency was observed for the toluene casted ones, a 2.5 % efficiency was reported for the chlorobenzene ones.[41] This higher power conversion efficiency was mainly correlated to an increase in short circuit current, which was attributed by to the smaller phase separated regions and a more uniform distribution observed by atomic force microscopy. Figure 1.13, illustrates this effect, showing the typical atomic force microscopy (AFM) images of the 2D surface topography and 1D profiles of the two type of films. It is seen that clusters of the size of 500 nm could be observed for the toluene casted film in contrast to the 100 nm size clusters for chlorobenzene casted films. The large phase separation present in toluene casted films is one of the major reasons for a lower charge carrier generation efficiency considering the small exciton diffusion length (10-20 nm) compared to the large (200-500 nm) fullerene clusters.

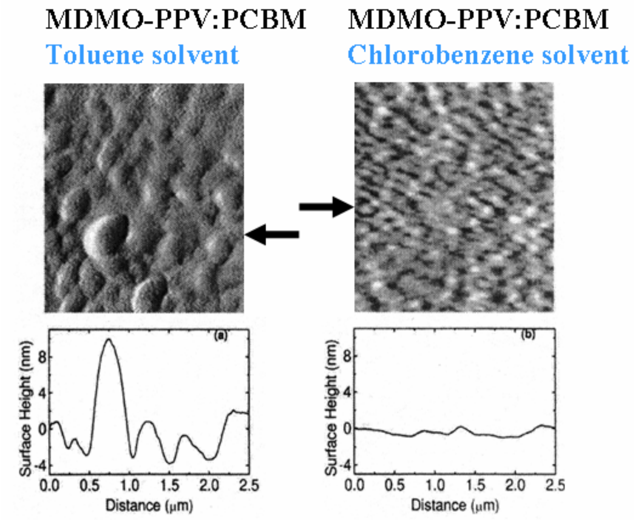

Figure 1.13: 2.5× 2.5 μm topography image of MDMO-PPV:PCBM 1:4 blend spincoated from toluene (left) and chlorobenzene (right). Below the height profiles are shown obtained at the position of the arrow.[reprinted from ref. 41]

Simultaneously, Liu *et al.* correlated the solar cell properties of a MEH-PPV: C_{60} blend to its morphology. A comparative study with different aromatic solvents (xylene, chlorobenzene and dichlorobenzene) and non aromatic solvents (chloroform and tetrahydrofuran) was performed.[42] It was claimed that by using non-aromatic solvents the intimate contact between the conductive conjugated backbones along MEH-PPV and the C_{60} molecules is prevented by the obstructive presence of the non-conductive side-chain groups of MEH-PPV, thus reducing the efficiency of the dissociation process, reducing the short circuit current and increasing the open circuit voltage.

Martens *et al.* performed Transmission electron microscopy (TEM) to investigate the morphology of MDMO-PPV:PCBM blends with different blend ratio and dissolved in chlorobenzene or toluene.[43-45] By combining planar and cross-sectional images a 3D view could be obtained. The TEM images are shown in Figure 1.14. A clear phase separation can be observed for the two systems. Because of the difference in density between MDMO-PPV and PCBM, the clusters observed by Shaheen *et al.* could now be identified as PCBM rich clusters imbedded in a MDMO-PPV:PCBM matrix (dark regions in Figure 1.14). Additionally, it was demonstrated that not only solvent choice influences the size of PCBM domains but also the blend ratio. Using chlorobenzene as a solvent, a blend ratio up to 1:2 MDMO-PPV:PCBM resulted in homogeneous mixing while the toluene casted one already showed phase separation.

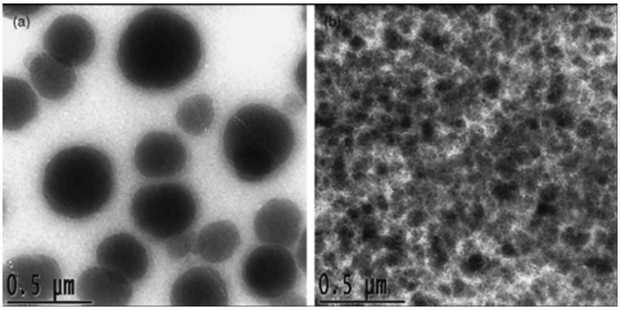

Figure 1.14: The 1:8 μm×1:8 μm TEM images of spincoated 1:4 MDMO-PPV:PCBM films from a toluene (a) and chlorobenzene (b) solution.[reprinted from ref. 43]

In addition, cross-sections of the MDMO-PPV blend were studied with high resolution Scanning electron microscopy (HR-SEM) revealing “nanospheres” of coiled MDMO-PPV.[46] The large PCBM clusters are shown to be surrounded by a polymer-rich matrix or skin-layer, as shown in Figure 1.15. In addition, the thin polymer skin reduces electron propagation to the electrode.

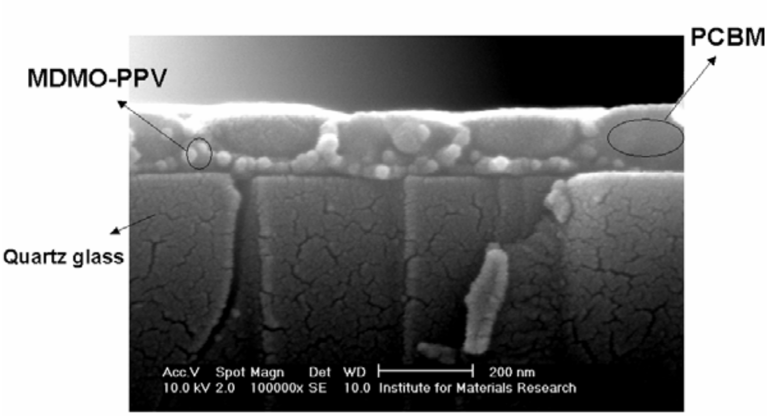

Figure 1.15: Scanning electron microscopy side view (cross-section) of MDMO-PPV:PCBM 1:4 blend dissolved in toluene prior to spincoating.

1.5.2. Blending ratio

In the first publications focussing on MDMO-PPV:PCBM and MEH-PPV:PCBM blends, 1:4 blend ratio was found to render the best solar cell characteristics.[36,41] Too low PCBM contents, led to an insufficient PCBM percolation path. As shown by Van Duren *et al.* in their extensive study of the morphology of MDMO-PPV:PCBM blends with different blend ratios, up to 50% PCBM contents a homogeneous mixing could be observed, resulting into poor photovoltaic properties of the corresponding device.[47] At higher PCBM concentrations an abrupt improvement of solar cell properties was evidenced together with the presence of phase separated regions. While increasing PCBM concentrations the phase separation is more pronounced and an increased device performance is observed. A maximum efficiency was obtained for 80% PCBM contents, confirming previous observations.[41] Changing the casting solvent, will imply that again the best blend ratio needs to be found to obtain the ideal morphology and the best percolation paths for both materials. Hence the optimal device properties will be reached. One can imagine that changing the material system will also imply a new extensive study for optimal blend ratio.

1.5.3. Casting parameters

Hoppe *et al.* demonstrated that not only the amount of fullerene fraction but also the total concentration of precursor solution will play a role in the extend of phase separation.[46] In addition, the influence of spinning frequency was also investigated. With increased spinning speed the mean size of the PCBM clusters was reduced while the homogeneity in cluster size remains comparable. Therefore it was demonstrated by Hoppe et al. that the phase separation is formed during film deposition and not beforehand in solution.

1.5.4. Post-production annealing treatments

While nano-sized crystals are encountered in the not annealed MDMO-PPV:PCBM blend. Yang *et al.* demonstrated recently that upon annealing the MDMO-PPV:PCBM blend, large PCBM micro-crystals were formed, destroying the original blend morphology.[48] During annealing micro-sized aggregates are formed which grow out to large PCBM crystals at the expense of surrounding PCBM clusters.[46,49] Hence, it was demonstrated that the morphology is instable at elevated temperatures. These results were also confirmed later by Bertho *et al.* who investigated the influence of the annealing process on the solar cell properties (see Figure 1.17) and the morphology (see Figure 1.16) during annealing of MDMO-PPV:PCBM blends.[50]

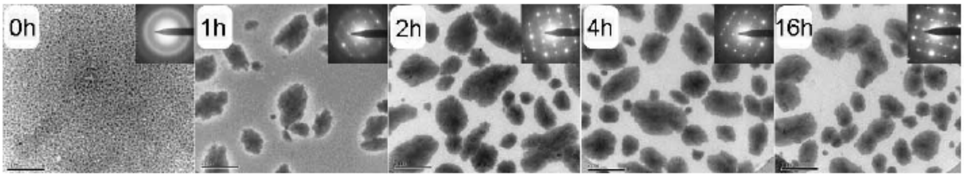

Figure 1.16: TEM images of MDMO-PPV:PCBM 1:4 blend in function of different annealing times (0h, 1h, 2h, 4h and 16h) at a temperature of 110°C (scale bar is 2 µm). [reprinted from ref. 50]

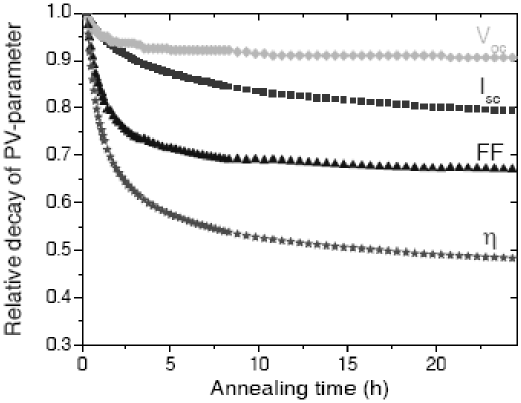

Figure 1.17: Relative decay of the short circuit current (Isc), open circuit voltage (Voc), fill factor (FF) and efficiency (η) of an MDMO-PPV:PCBM 1:4 solar cell at 110°C.[reprinted from ref. 50]

An overall monotonic decay of all solar cell parameters was observed with increased annealing time. More interesting the saturation effect, suggesting not complete damaging of the cells, or a non evolution of the morphology beyond a certain annealing time.

1.6. Aim of this thesis

The previous overview clearly points out how morphology plays a crucial role in the study of bulk heterojunction solar cells. At the start of this PhD study an important breakthrough was accomplished when MDMO-PPV was substituted by regioregular poly(3-hexylthiophene) (P3HT) (chemical structure shown in Figure 1.18).

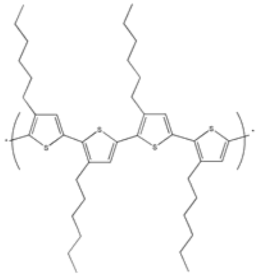

Figure 1.18: Chemical structure of regioregular P3HT.

P3HT is a polythiophene derivative which already was used extensively in other polymer based semiconductor research, as electrochromic material, organic LEDs and as a sensor material.[51-53] The insolubility problem of polythiophene was overcome when alkyl side chains were added. By 1992, first regioregular polyalkylthiophenes were fabricated. By attaching the sidechains in a fixed pattern, a high degree of order could be obtained.[54] The natural tendency of P3HT to crystallize and form ordered structures generated carrier mobilities beyond 0.1 cm²/Vs, i.e. the highest one reported for polymeric semiconductors.[55] In addition, the absorption spectra of P3HT was shown to better match the solar spectrum than MDMO-PPV. Hence, the good solubility, chemical stability, high charge carrier mobility and spectral match turned it into an ideal candidate to be used in bulk heterojunction solar cells.[56-58] In 2003, Padinger *et al.* achieved a power conversion efficiency of 3.5% for a P3HT:PCBM based blend solar cell.[59] For such power conversion efficiency post production annealing was required. It was the first time demonstrated that an annealing process could have such a large impact on the device efficiency (from 0.4% up to 2.5% and even 3.5% with additional dc voltage applied). Considering the crucial role played by the blend morphology in MDMO-PPV:PCBM blend solar cells, morphology study emerged as a key issue to be considered for further optimization of such new type of blends and therefore defined the first key point of this PhD.

In this thesis a thorough morphology study has therefore first been performed on the P3HT:PCBM system for different blend ratios and a broad range of annealing conditions. As casting solvent, chlorobenzene was used, since it gave the best results for the reference blend MDMO-PPV:PCBM. A further study of the influence of different solvents can be found in the PhD thesis of Peter Vanlaeke.[60] In order to better understand why this morphology is formed with annealing treatment and how it is formed, it is essential to perform thermal analysis on the blends. Up till now, the ideal morphology was only obtained by trail and error and a broad range of samples had to be made. In order to get clear and direct idea of what type of morphologies can be possible with different

weight ratios and different solvents it is essential to obtain a phase diagram for new material systems. Ideally, a 3D phase diagram should be made were the concentration of both materials are plotted in function of the solubility (choice of solvent). In this thesis only an initial state diagram (2D) has been obtained to get a coarse idea of how this blend system is behaving.
In addition to thorough morphology study of the blend it is important to understand the insufficiently known relationship between morphology and solar cell parameters, Scanning probe microscopy (SPM) characterization methods offer a wide variety of techniques which can be used to probe simultaneously the morphology and the local electrical properties of the blend at the nanoscale. In addition to the morphology characterization, different SPM techniques were applied in this work to explore locally the electrical properties of the P3HT:PCBM blend system. Additionally the MDMO-PPV:PCBM blend system was also electrically characterized with SPM. Since this material system is more known than the P3HT:PCBM, it was easier to use this system to test the different SPM techniques used and to get a clear insight of the conductivity properties of PCBM and of the donor-acceptor interface.

1.7. Outline

In the second chapter a thorough study of the blend morphology is presented for the state-of-the-art P3HT:PCBM blend casted from chlorobenzene. It first consists of a brief overview of the different techniques used to characterize morphology like Transmission Electron Microscopy (TEM), X-Ray Diffraction (XRD), Atomic Force Microscopy (AFM), confocal fluorescence microscopy and optical microscopy. A broad range of annealing conditions were applied to different blend ratios of the P3HT:PCBM blend. The resulting films were studied to obtain topographical, crystallographic and bulk morphological information. Finally, the structures formed by annealing are more closely studied to explore the nature of large PCBM crystals formed by annealing.

In chapter 3, a 2D state diagram is formulated for the P3HT:PCBM system in order to get further insight in the different morphologies encountered in chapter 2. The techniques used for thermal analysis like traditional and modulated Differential Scanning Calorimetry (DSC and MTDSC) are first described. Pure P3HT and PCBM are initially investigated, latterly followed by the P3HT:PCBM system with different blend ratios. The chapter ends with a presentation of the 2D state diagram. This work was performed in collaboration with the group of prof. dr. ir. Bruno Van Mele and prof. dr. ir. Guy Van Assche at the Vrije Universiteit Brussel (VUB).

In chapter 4 electrical properties of MDMO-PPV:PCBM and P3HT:PCBM blends were locally measured by means of Electrostatic Force Microscopy (EFM) and

Conductive AFM (C-AFM). The principles and detection systems of a conventional EFM system are first described in detail pointing out intrinsic advantages and drawbacks. A more suitable EFM set-up used to perform transversal conductivity measurements is then described and the results obtained on both MDMO-PPV:PCBM and P3HT:PCBM systems are presented and analyzed. In a second part C-AFM is thoroughly presented together with the results typically obtained across MDMO-PPV:PCBM and P3HT:PCBM blends. Further, by means of C-AFM, local IV-profiles have been recorded across P3HT. The results are compared with what obtained from conventional electrical characterization methods. This work was performed in collaboration with the group of prof. dr. Chris Van Haesendonck and dr. Alexander Volodin at the Katholieke Universiteit Leuven (KUL).

In a last chapter all conclusions are summarized again and future work is discussed.

1.8. References

[1] http://ocde.p4.siteinternet.com/publications/doifiles/012005061T020.xls
[2] http://ocde.p4.siteinternet.com/publications/doifiles/012005061T019.xls
[3] http://www.solarexpert.com/pvbasics2.html
[4] http://www.ecn.nl/zon/extra/waarom-zonne-energie/
[5] http://www.solarnavigator.net/solar_panels.htm
[6] http://www.ecn.nl/fileadmin/ecn/units/zon/docs/geschiedenis_van_de_zonnecel
[7] http://www.californiasolarcenter.org/history_pv.html
[8] M. Riordan, L. Hoddeson, *IEEE Spectrum*, 1997, 46.
[9] D. M. Chapin, C. S. Fuller, G. L. Pearson, *J. Appl. Phys.*, **25**, 1954, 676.
[10]http://southface.org/solar/solar-roadmap/solar_how-to/history-of-solar.htm
[11] http://www.nrel.gov/ncpv/thin_film/docs/kaz_best_research_cells.ppt
[12] M. Schwoerer, H. C. Wolf, Organic Molecular Solids, Weinheim, 2007, chapter one
[13] J. C. Kotz, P. Treichel, Chemistry and chemical reactivity, Saunders College publishing, chapter 10
[14] A. Pochettino, *Acad. Lincei Rend.*, **15** ,1906, 355.
[15] M. Volmer, *Ann. Physik*, **40,** 1913, 775.
[16] H. Kallmann, M. Pope, *J. Chem. Phys.*, **30**, 1959, 585.
[17] D. Kearns, M. J. Calvin, *Chem. Phys.*, **29**, 1958, 950.
[18] C. W. Tang, A. C. Albrecht, *J. Chem. Phys.*, **63**, 1975, 953.
[19] C. W. Tang, A. C. Albrecht, *J. Chem. Phys.,* **62,** 1975, 2139.
[20] M. Mabrouki, A. Oueriagli, A. Outzourhit, E. L. Ameziane, S. Hotchandani, R. M. LeBlanc, *Phys. Stat. Sol.,* **191**, 2002, 345.
[21] T. A. Skotheim, Handbook of Conducting Polymers, Dekker, New, York, 1986.
[22] H. Shirakawa, E. J. Lewis, A. G. MacDiarmid, C. K. Chiang, A. J. Heeger, *J. Chem. Soc. Chem. Commun.,* 1977, 578.
[23] C. K. Chiang, C. R. Fincher, Y. W. Park, A. J. Heeger, H. Shirakawa, E. J. Lewis, S. C. Gau, A. G. MacDiarmid, *Phys. Rev. Lett.*, **39**,1977, 1098.
[24] S. Glenis, G. Tourillon, F. Garnier, *Thin Solid Films*, **139**, 1986, 221.
[25] S. Karg, W. Riess, V. Dyakonov, M. Schwoerer, *Synth. Met.*, **54**, 1993, 427.
[26] C. W. Tang, *Appl. Phys. Lett.*, **48**, 1986, 183.
[27] N. S. Sariciftci, L. Smilowitz, A. J. Heeger, F. Wudl, *Synth. Met.*, **59**, 1993, 333.
[28] N. S. Sariciftci, D. Braun, C. Zhang, V. I. Srdanov, A. J. Heeger, G. Stucky, F. Wudl, *Appl. Phys. Lett.*, **62**, 1993, 585.
[29] J. J. M. Halls, K. Pichler, R. H. Friend, S. C. Moratti, A. B. Holmes, *Synth. Met.*, **77**, 1996, 277.

[30] J. J. M. Halls, K. Pichler, R. H. Friend, S. C. Moratti, A. B. Holmes, *Appl. Phys. Lett.*, **68**, 1996, 3120.
[31] G. Yu, K. Pakbaz, A. J. Heeger, *Appl. Phys. Lett.*, **64**, 1994, 3422.
[32] J. J. M. Halls, J. Cornil, D. A. dos Santos, R. Silbey, D.-H. Hwang, A. B. Holmes, J. L. Brédas, R. H. Friend, *Phys. Rev. B*, **60**, 1999, 5721.
[33] H. J. Snaith, A. C. Arias, A. C. Morteani, C. Silva, R. H. Friend, *Nano Letters*, **2**, 2002, 1353.
[34] A. J. Breeze, Z. Schlesinger, S. A. Carter, H. Tillmann, H.-H. Hörhold, *Sol. En. Mat. Sol. Cells*, **83**, 2004, 263.
[35] J. C. Hummelen, B. W. Knight, F. Lepec, F. Wudl, *J. Org. Chem.*, **60**, 1995, 532.
[36] G. Yu, J. Gao, J. C. Hummelen, F. Wudl, A. J. Heeger, *Science*, **270**, 1995, 1789.
[37] S. Alem, R. De Bettignies, J.-M. Nunzi, M. Cariou, *Appl. Phys. Lett.*, **84**, 2004, 2178.
[38] T. Aernouts, W. Geens, J. Poortmans, P. Heremans, G. Borghs, R. Mertens, *Thin Solid Films*, **403**, 2002, 297.
[39] T. Munters, T. Martens, L. Goris, V. Vrindts, J. Manca, L. Lutsen, W. De Ceuninck, D. Vanderzande, L. De Schepper, J. Gelan, N.S. Sariciftci, C.J. Brabec, *Thin Solid Films*, **403**, 2002, 247.
[40] C. Y. Yang and A. J. Heeger, *Synth. Met.*, **83**, 1996, 85.
[41] S. E. Shaheen, C. J. Brabec, N. S. Sariciftci, F. Padinger,
T. Fromherz, J. C. Hummelen, *Appl. Phys. Lett.*, **78**, 2001, 841.
[42] J. Liu, Y. Shi and Y. Yang, *Adv. Funct. Mater.*, **11**, 2001, 420.
[43] T. Martens, J. D'Haen, T. Munters, Z. Beelen, L. Goris, J. Manca, M. D'Olieslaeger, D. Vanderzande, L. D. Schepper and R. Andriessen, *Synth. Met.*, **138**, 2003, 243.
[44] T. Martens, Z. Beelen, J. D'Haen, T. Munters, L. Goris, J. Manca, M. D'Olieslaeger, D. Vanderzande, L. D. Schepper and R. Andriessen, *Proc. SPIE-Int. Soc. Opt. Eng.*, **40**, 2003, 4801.
[45] T. Martens, J. D'Haen, T. Munters, L. Goris, Z. Beelen, J. Manca, M. D'Olieslaeger, D. Vanderzande, L. D. Schepper and R. Andriessen, presented at the MRS Spring Meeting, San Francisco, 2002.
[46] H. Hoppe, M. Niggemann, C. Winder, J. Kraut, R. Hiesgen, A. Hinsch, D. Meissner, N. S. Sariciftci, *Adv. Funct. Mater.*, **14**, 2004, 1005.
[47] J. K. J. van Duren, X. Yang, J. Loos, C. W. T. Bulle-Lieuwma, A. B. Sieval, J. C. Hummelen, R. A. J. Janssen, *Adv. Funct. Mater.*, **14**, 2004, 425.
[48] X. Yang, J. K. J. van Duren, R. A. J. Janssen, M. A. J. Michels, J. Loos, *Macromolecules*, **37**, 2004, 2151.
[49] H. Hoppe, M. Drees, W. Schwinger, F. Schäffler, N. S. Sariciftci, *Synth. Met.*, **152**, 2005, 117.
[50] S. Bertho, W. Moons, G. Janssen, I. Haeldermans, A. Swinnen, L. Lutsen, J. D'Haen, E. Goovaerts, J. Manca, D. Vanderzande, MRS proceedings

[51] K. Hyodo, *Electrochimica Acta*, **39**, 1994, 265.

[52] D. H. Hwang, M. J. Park, C. Lee, *Synth. Met.*, **152**, 2005, 205.

[53] C. Bartic, B. Palan, A. Campitelli, G. Borghs, *Sensors and Actuators B-Chemical*, **83**, 2002, 115.

[54] R. D. McCullough, *Adv. Mater.*, **10**, 1998, 93.

[55] D. H. Kim, Y. D. Park, Y. Yang, H. Ynag, Y. H. Kim, J. I. Han, D. G. Moon, S. Park, T. Chang, C. Chang, M. Joo, C. Y. Ryu and K. Cho, *Adv. Funct. Mater.*, **15**, 2005, 77.

[56] Z. Bao, A. Dodabalapur, A. J. Lovinger, *Appl. Phys. Lett.*, **69**, 1996, 4108.

[57] H. Sirringhaus, N. Tessler, R. Friend, *Science*, **280**, *1998*, 1741.

[58] M. Raja, G. C. R. Lloyd, N. Sedghi, W. Eccleston, R. D. Lucrezia, S. J. Higgins, *J. Appl. Phys.,* **92**, 2002, 1441.

[59] F. Padinger, R. S. Rittberger, N. S. Sariciftci, *Adv. Funct. Mater.*, **13**, 2003, 85.

[60] P. Vanlaeke, “P3HT:PCBM bulk heterojunction organic solar cells electrical, optical and morphological results”, PhD thesis, 2006.

2. Morphology versus preparation techniques of model systems

In the previous chapter, it was clearly indicated that morphology of the active layer of bulk heterojunction solar cells can have a significant influence on the performance. Poly(alkylthiophenes) are among the most promising materials in the research of bulk heterojunction solar cells because of their good solubility, chemical stability and high charge carrier mobility. As previously mentioned, Padinger et al. were the first to enhance the performance of P3HT:PCBM by applying a post-production annealing.[1] At the start of this work, a thorough morphology study was lacking. No research had been done on the morphology change caused by this post-production annealing. It was therefore one of the main goals of this thesis to better understand this phenomenon through a systematic morphological study, as reported in the present chapter. In this chapter, the P3HT:PCBM material system is fully morphologically characterized and the influence of post-production annealing is demonstrated using transmission electron microscopy (TEM), X-ray diffraction (XRD), atomic force microscopy (AFM), confocal fluorescence microscopy, and optical microscopy. Topography and roughness information at smaller scale was probed by AFM. Optical microscopy was used to obtain information about morphology at larger scale. TEM provided an insight in bulk morphology and crystallographic information (Selected Area Electron Diffraction). Crystallographic information was also found by XRD. In the study of the active layer of bulk heterojunction solar cells, the use of confocal fluorescence microscopy was introduced, which enables us to locally identify materials. In addition, the formation of large needles was more closely studied with cross-sectional TEM imaging.

2.1. Experimental techniques

In the next paragraphs, the different techniques used for morphology study in this thesis and specimen preparation will be described.

2.1.1. Transmission electron microscopy (TEM)

Transmission electron microscopes are electron optical instruments analogues to light microscopes, where the specimen is illuminated by an electron beam. This requires operation in vacuum, since air scatters electrons. High resolution is possible because of the short wavelength of the electrons. Practically, only a resolution in the Å range can be obtained in traditional TEM, due to lens errors (chromatic, spherical).

2.1.1.1. Working principle

A Transmission electron microscope, see Figure 2.1, consist of a thermionic electron gun that creates a beam of electrons, accelerated towards the sample by applying a positive electric potential.

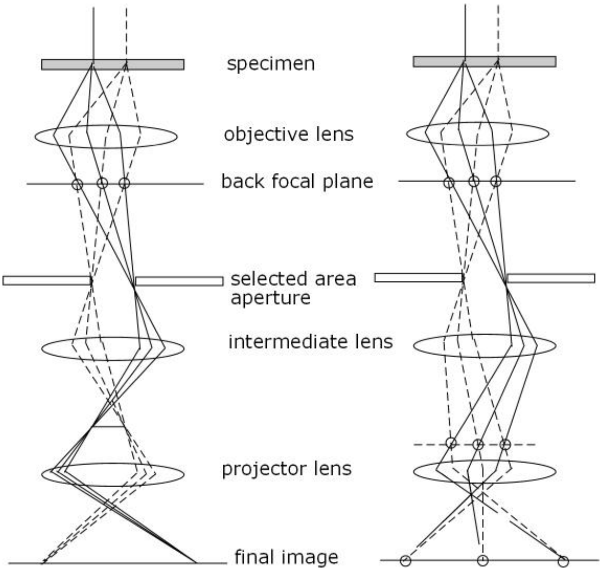

Figure 2.1: Schematic of Transmission Electron Microscopy in imaging mode (left) and diffraction mode (right).

This beam of electrons is passing through one or more condenser lenses to control the convergence, coherence and intensity of the beam falling on the sample. Consequently, the diverging transmitted electrons are focused by an objective lens, important in determining contrast and resolution of image. Next, an objective aperture enhances the contrast by blocking out all high angle diffracted electrons followed by a selected area aperture enabling the examination of the periodic diffraction of electrons by ordered arrangements of atoms in the sample. Last, an intermediate lens and a projector lens provides further magnification in order to collect the electrons on a phosphorous screen or a CCD camera. Adjusting the strength of projector and intermediate lenses, makes it possible to change from imaging mode (Figure 2.1 left) and diffraction mode (Figure 2.1 right). First, diffraction mode will be discussed.

2.1.1.2. Diffraction mode

The diffraction of electrons according to local atomic organization can be used in TEM to identify crystal structures and local orientation. In TEM, a single crystal will produce a diffraction pattern of sharp spots, while polycrystalline materials will form one or several ring patterns. An amorphous material will be displayed as a diffuse circular ring, correlated to near neighbour distances. However, in polymers crystallinity is caused by intra and/or interchain ordering. Polymer crystals are therefore often imperfect, giving fuzzy diffraction spots or broad rings comparable with the ones from oriented crystalline material. The bigger the crystalline polymer regions present, the sharper the rings while the amount of crystalline regions will influence the intensity of the diffraction rings.

In order to get diffraction, Bragg's law (equation 1-1) needs to be fulfilled:

$$2\ d \sin \theta = \lambda \qquad \text{equation 2-1}$$

With λ the wavelength of the incident electron beam, d the spacing between the planes in the atomic lattice and θ is the angle between the incident beam and the scattering planes. For electrons $\lambda << d$ makes θ very small, see Figure 2.2. Therefore, it is important to note that lattice planes that are almost parallel to the beam can only be measured.

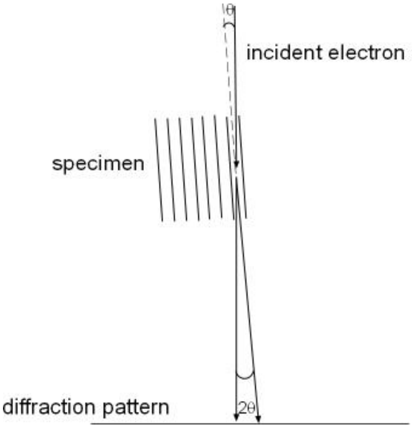

Figure 2.2: Schematic of a electron diffraction from a set of lattice planes, showing that the planes must be nearly parallel to the incident beam direction.

In selected area electron diffraction (SAED) in TEM, the selected area aperture, see Figure 2.1, is used to select a region of a few μm^2, of the specimen for diffraction.

2.1.1.3. Imaging modes

Different techniques can be used in TEM. Conventional imaging modes like bright field (BF) and dark field (DF) are being described here. TEM contrast is due to electron scattering and absorption. An objective aperture is used in the back focal plane to make images with the undiffracted (BF) or a selection of the diffracted electrons (DF). When the aperture is positioned to pass only transmitted electrons, a bright field image is formed. Amorphous materials will mainly give a mass thickness contrast image, where thicker denser areas will absorb more electrons and cause darker regions. While for crystalline materials, if a crystalline region diffracts the incident electrons according to the Bragg's law (see 2.1.2), it will be displayed as a darker region in the BF mode. In conclusion, a bright field image originates from absorption and diffraction effects. For DF imaging, large angle scattered electrons are collected, rendering images origination from local diffraction effects.

TEM experiments and SAED analysis were performed with a Philips CM12-STEM. Images shown here were taken in BF mode.

2.1.2. X-Ray diffraction (XRD)

X-ray diffraction is a powerful technique to characterize crystalline materials. It is based on the elastic scattering of X-rays from structures with long range ordering. An XRD, see Figure 2.3, consists of an X-ray source, with a certain wavelength λ, bombarding the sample. Some X-rays are reflected by the sample surface while others are reflected from a plane of atoms inside the sample. The distance traveled depends on the incident angle of the X-ray and the atomic plane distances. The reflected penetrating wave should have traveled a whole number of wavelengths while it was inside of the material, in order to get constructive interference with the reflected surface waves. This condition is described by Bragg's law (see equation 2-1). With λ the wavelength of the incident X-rays (λ_{Cu} = 0.154056 nm), d the spacing between the planes in the atomic lattice and θ is the angle between the incident ray and the scattering planes.

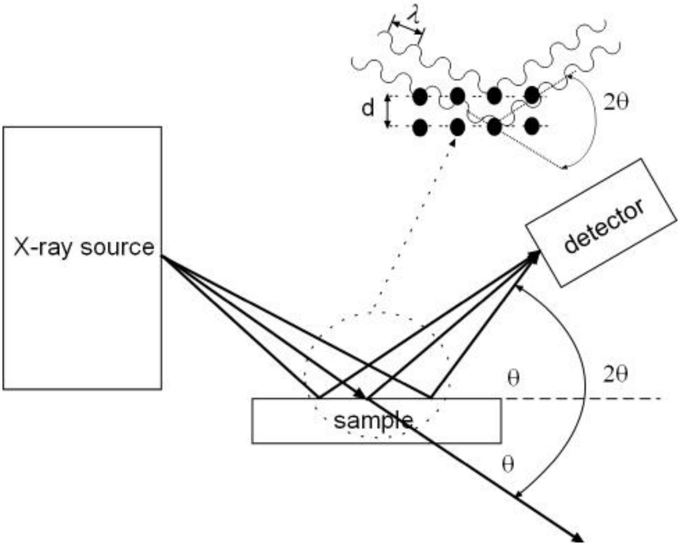

Figure 2.3: Schematic of an X-Ray diffraction set-up.

For XRD, the wavelength of the incident beam is in the order of the distance between the lattice planes. The θ-2θ mode makes it possible to measure lattice planes almost parallel to the substrate surface. Therefore in this thesis the lattice planes almost parallel to the substrate surface will be measured with XRD while with TEM the lattice planes transversal to the substrate will be measured, making both techniques complementary.

XRD measurements were done on a Siemens D5000 diffractometer in θ-2θ mode. The incident beam used is the $CuK_{\alpha1}$ line of a Ge(111) monochromator, having a λ = 0.154056 nm.

2.1.3. Atomic Force Microscopy

A typical set-up of an AFM system in given in Figure 2.4.

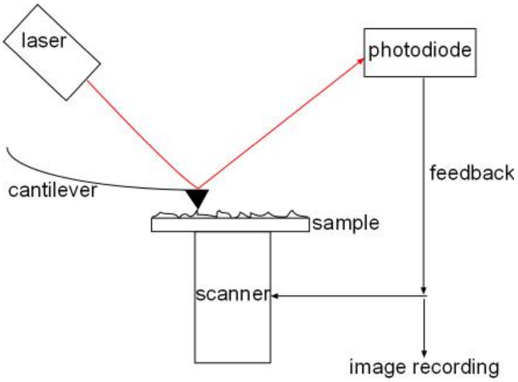

Figure 2.4: Schematic of a typical AFM set-up.

The atomic force microscope (=AFM), consists of a sharp mostly Si tip, a couple of microns long and often with a tip radius of about 10 nm, located at the end of a cantilever, that is 100 to 200 μm long. As the tip scans the surface of the sample, forces between the tip and the sample surface cause the cantilever to bend. An optical lever, consisting of a laser and a photodetector, measures the deflection of the cantilever. The tip sample interactions is kept constant by a feed-back circuit, enabling topography measurement. The AFM can operate in two scanning modes, i.e. contact and non-contact mode. In a contact mode scan, the tip is kept constant at a certain height above the sample. Topography probing occurs by means of cantilever deflection measurement. Constant-force mode is an alternative way to measure the topography in contact mode. A feedback circuit will keep the tip-sample interaction force constant. In non-contact mode, the cantilever is oscillating near its first mechanical resonance frequency. The feedback loop ensures a constant tip-sample distance by maintaining the resonant frequency of oscillation (i.e. frequency-modulation mode) or the amplitude of oscillation (i.e. amplitude-modulation mode).[2] A third scanning mode, semi-contact mode or tapping mode, combines previous modes enabling higher resolution imaging without damaging the sample. Spatial resolution of this technique depends on the kind of tip used, the sharper the probe the higher the resolution, probing in air or vacuum, and environmental conditions (humidity). Typical spatial resolution for tapping mode operating in air is 5 to 10 nm, assuming a tip radius of respectively 5 to 10 nm. The vertical resolution, controlled by the piezo-electric scanner, of this technique is below 1 nm.

AFM measurements were carried out with an Autoprobe CP from Park Scientific Instruments in tapping mode under ambient atmosphere. Tips of the NSC11 type B were supplied by MicroMash with a resonance frequency of 330 kHz and a springconstant of 48 N/m.

2.1.4. Confocal fluorescence microscopy

Confocal fluorescence microscopy is well suited to study in thin, up to 50 μm, optical slices the fluorescence emission of solid samples as well as living materials with a XY resolution of around 200 nm and a Z resolution of 600 nm. Upon laser illumination matching the absorption properties of a sample, fluorescence is observed when excited electrons return from the higher electronic state to the ground state under emission of light with a longer wavelength, as seen in Figure 2.5 .

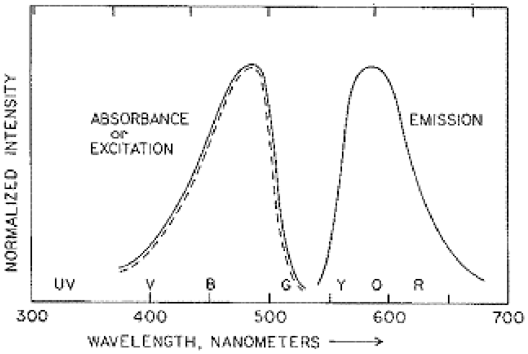

Figure 2.5: Absorbance and emission spectra.

The main advantage of a confocal microscope over other optical microscopes is its ability to collect fluorescence emission from a single in-focus optical plane while excluding out-of-focus fluorescence and stray light contributions rendering a crisper higher contrast image with much reduced background. To this end a confocal detector pinhole is essential. By scanning a stack of confocal slices a true 3D image is reconstructed. In Figure 2.6, a schematic is shown of a state-of-the-art confocal fluorescence microscopy set-up with infinity corrected optics.

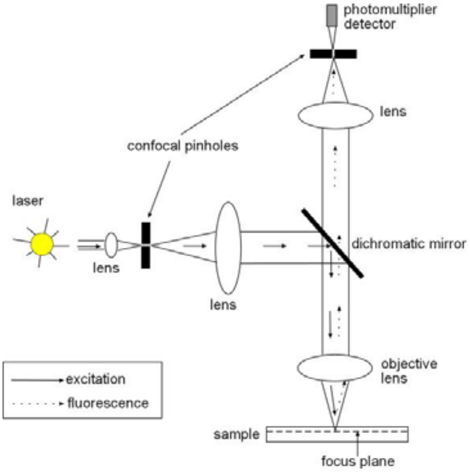

Figure 2.6: Schematic of confocal fluorescence microscopy set-up.

A carefully selected set of laser colors, which in excitation wavelength match commonly available fluorophores, travels through a single mode fiber optic acting as a confocal pinhole. After recollimation a dichroic mirror reflects the laser light, which is subsequently focused by the objective on to the sample. A certain fraction of the absorbed laser light is emitted as fluorescence by the specimen. The objective collects part of the fluorescence and this light passes through the dichroic mirror towards the detector. After passing through the adjustable pinhole in front of the detector, the fluorescent light is converted by a photomultiplier detector and electronics into a digital signal for image display and data storage.

Confocal images were collected with a Zeiss LSM-510 META inverted confocal microscope at room temperature with a long working distance LD 40x/0.6 corr objective. Illumination was with the Argon ion laser 488 nm with an extra 488 nm excitation interference filter inserted before the excitation fiber optic for spectral clean-up. Intensity on the sample was 10 – 20 µW. Upon intense laser illumination (minimal 1% of a 488 nm laser, rendering tens to hundreds kW/cm^2 in the focus spot) molecules can degrade. Hence upon scanning fluorescence emission will diminish, called photo bleaching. In the next experiments, no photo bleaching was observed under these conditions. Images were collected through a band pass emission filter. Image frame size, 512 x 512 pixels HxV, was 230.3 µm square with a pixel dwell time of 102 µs. Images were processed with the Zeiss supplied software and with ImageJ (NIH).

2.1.5. Sample preparation

Different ratios of regioregular (90%-93%) P3HT (Rieke, molecular weight (M_w) = 49886 g/mol and polydispersity of 2.2) were blended with PCBM (Nano-C). P3HT consists of a thiophene backbone with a hexyl side-chain, as shown in Figure 2.7. The relative position of the hexyl side-chain on the neighboring thiophene rings determines the degree of regioregularity. P3HT was dissolved in chlorobenzene and stirred overnight at a temperature of 50°C.

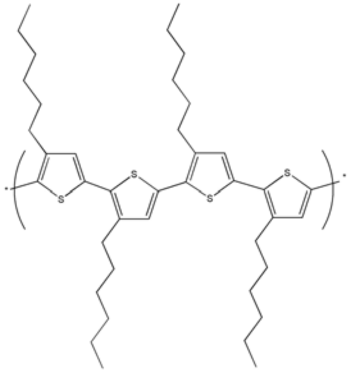

Figure 2.7: Chemical structure of regioregular P3HT.

By spincoating these solutions, films of around 100 nm, as determined by profilometry (Sloan Dektak^3 ST surface profiler), were obtained. Spincoating was performed in nitrogen atmosphere in order to prevent oxidation and degradation of the polymer. The P3HT:PCBM blends were spincoated on glass substrates, which had been cleaned by following pre-cleaning procedure:

- mechanical cleaning with soap soaked dust-free cleanroom wipes

- 30 min in ultrasonic bath in de-ionized (DI) water with detergent

- rinsing with DI water

- 10 min in ultrasonic bath with DI water

- rinsing with acetone

- 10 min in ultrasonic bath with acetone

- rinsing with isopropanol (IPA) water

- 10 min in boiling IPA

- blow drying with nitrogen flow

For the TEM measurements, thin freestanding films were prepared. Post-production annealing was carried out using a hotplate in nitrogen atmosphere for different annealing times at temperatures from 75°C-250°C, with an interval of 25°C.

2.2. P3HT:PCBM blends

2.2.1. *Ordering of P3HT*

P3HT is a semi-crystalline polymer. A schematic of the crystalline lattice formed by P3HT is given in Figure 2.8.

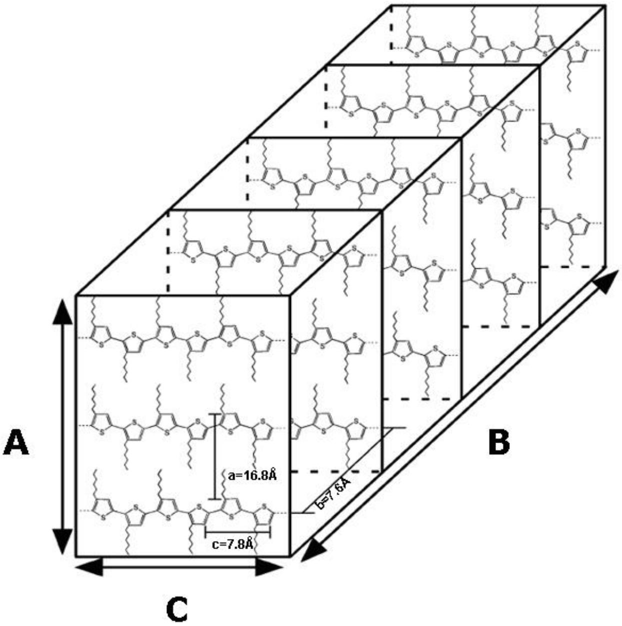

Figure 2.8: Schematic representation of molecular arrangement within P3HT.

Here, three axis, A,B and C, are going to be defined to characterize the unity cell of P3HT. The AC-plane corresponds to the plane formed by the polymer backbone and the corresponding side chains. The A-axis is in the direction coming from the thiophene ring to the corresponding sidechain, while the C-axis follows the direction along the main polymer backbone, which means from thiophene to thiophene ring. The B-axis, thus lies in the plane perpendicular to the one formed by A and C, and in the direction perpendicular to the polymer backbone. This unity cell can now be used to define the position of crystalline planes present. The position of a crystalline plane is defined by a set of three parameters (hkl), called Miller indices, correlated to the unity cell axes. When P3HT crystallizes, a lamellar structure is formed in which the main polymer chains are laterally packed, so parallel to the BC plane and perpendicular to A, which are separated by regions filled by the alkyl side chains, with an interdistance of 16.8 Å (a) (i.e. (100) plane). In the BC-plane, the stacking of thiophene rings in successive polymer chains is giving an ordering, parallel to the polymer backbone direction and in the AC-plane, with an interdistance of 3.8 Å (b) (i.e. (020) plane), also known as π-π stacking. Thirdly, sidechain ordering is occurring in the AB plane perpendicular to the polymer backbone direction, with an interdistance of 3.9 Å (half of distance indicated by c) (i.e. (002) plane).[3,6,9,11,13]

It is known from literature that an annealing of pristine P3HT above its glass transition temperature (T_g) (i.e. in the next chapter the Tg of P3HT was proven to be at 18.7 °C) induces an enhanced crystallization of the polymer.[4,5] To investigate whether this enhanced crystallization also takes place in P3HT:PCBM blends, an XRD and TEM-study has been performed on thin films of different P3HT:PCBM blend ratios and submitted to different annealing conditions. Both techniques, XRD and TEM, can be used complementary to characterize the three dimensional crystalline lattice of P3HT. As explained in paragraph 2.1.1.2 and 2.1.2, XRD in θ-2θ mode will be first used to characterize crystalline planes parallel to the substrate, secondly TEM will be used to characterize those perpendicular to the substrate surface.

2.2.1.1. X-Ray diffraction measurements

As a reference, diffractograms of pure P3HT and pure PCBM, as it was received from the supplier, were first measured for $2\theta<30°$, seen in Figure 2.9.

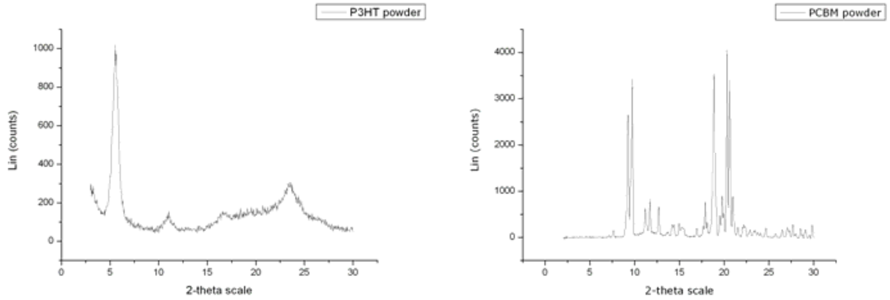

Figure 2.9: Pure P3HT (left) and pure PCBM (right) diffractograms.

The non-annealed pure P3HT shows a broad peak around 5.46° (2θ), attributed to the (100)-reflection of semi-crystalline P3HT, corresponds to an intermolecular spacing of 16.8 Å of well-organized lamellar structure, consistent with literature.[6-8] A small broad diffraction peak is encountered at 23.5° (2θ), corresponding to a spacing of 3.79 Å and the superposition of (020) and (002) planes.[4,7,14] When these diffractograms were measured, the pure material is randomly distributed over the Si sample holder. Hence, crystals are randomly orientated over the holder, making it possible to detect (020) and (002) plane in powder diffraction in XRD. In the powder diffraction diagram of PCBM five intense peaks appear: 9.28°, 9.72°, 18.8°, 20.32°, and 20.64°, corresponding to d-values of respectively 9.5 Å, 9.09 Å, 4.71 Å, 4.36 Å, and 4.29 Å, as was also found by Erb *et al.*.[9] XRD measurements were also performed on spincoated pure P3HT (Figure 2.10 top left) and pure PCBM (not shown). Distinct differences were encountered. The spincoated pure PCBM did not show any diffraction peaks at all. In the P3HT spincoated layer only a small diffraction peak was noticed at 5.46°, higher diffraction angle peaks were absent, which is consistent with literature reports.[4] With increased temperature treatment this peak increases, indicating more crystallization in the (100) direction is taking place.

In Figure 2.10, the XRD data are plotted for the P3HT:PCBM weight ratios 1:0, 1:1, 1:2 and 1:4. Because of the lack of higher angle diffraction peaks and the low intensity of the primary peak, the XRD data were only shown for $2\theta<10°$. Non-annealed samples were compared with samples annealed for 5 min at 125°C.

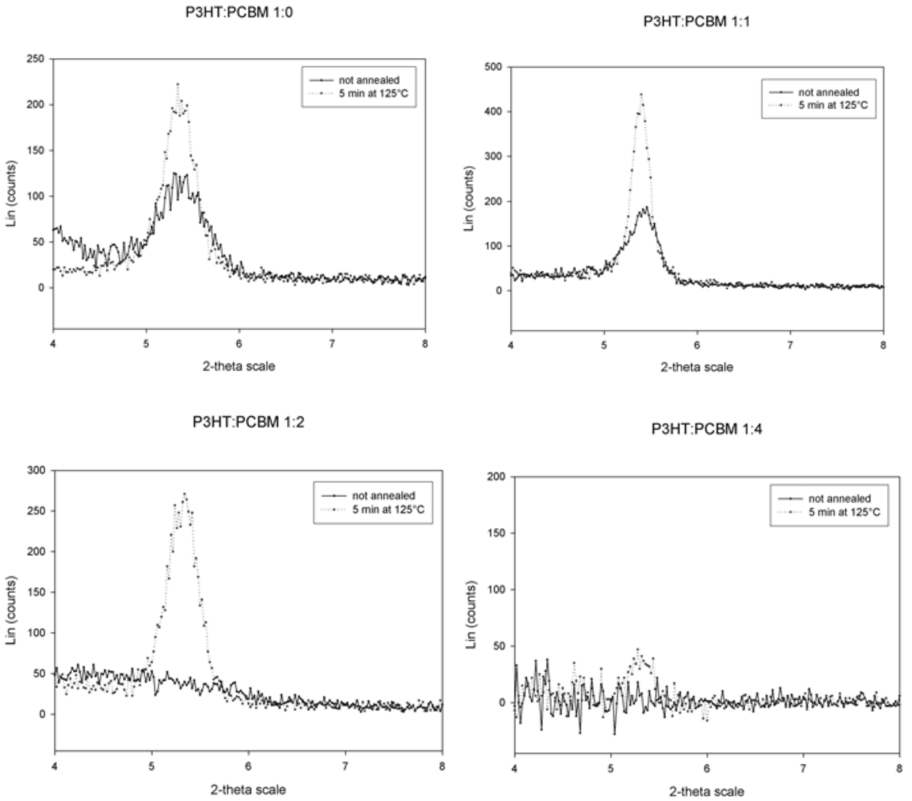

Figure 2.10: XRD data of pure P3HT and P3HT:PCBM blends not annealed compared to blends annealed for 5 min at 125°C as a function of blend ratio.

Compared to pure P3HT annealed for 5 min at 125°C more or larger regions of coherent scattering are present in the 1:1 blend annealed for 5 min at 125°C. A possible explanation could be found in the thickness variations of both films. Spincoated films can have a thickness variation across the substrate up to 20% (for a 100 nm thick film), depending on the viscosity of the solution. When a surplus (1:2 blend) of PCBM compared to P3HT is added, the crystallization of P3HT gets suppressed, which was also observed for P3HT blends dissolved in chloroform by Erb. *et al.*[9] For the 1:4 blend, only a very broad peak is present after annealing for 5 min at 125°C. It can thus be concluded that the enhanced crystallization with increased temperature that occurs in the pure P3HT can also take place in the P3HT:PCBM blend, but in the blend the ordering of P3HT is hampered by the amount of PCBM present.

2.2.1.2. TEM measurements

2.2.1.2.1. Pure P3HT and PCBM

As a reference, TEM images and corresponding diffraction patterns were obtained of the pristine spincoated P3HT (Figure 2.11 left) and PCBM. The results obtained from the pristine P3HT were compared with P3HT annealed for 5 min at 100°C and 125°C. The diffraction patterns suffer from a strong inelastic scattering contribution. In order to improve the signal-to-noise ratio, an integration over the complete diffraction ring was made. On the right side of Figure 2.11 the intensities are plotted as a function of incident beam angle, θ.

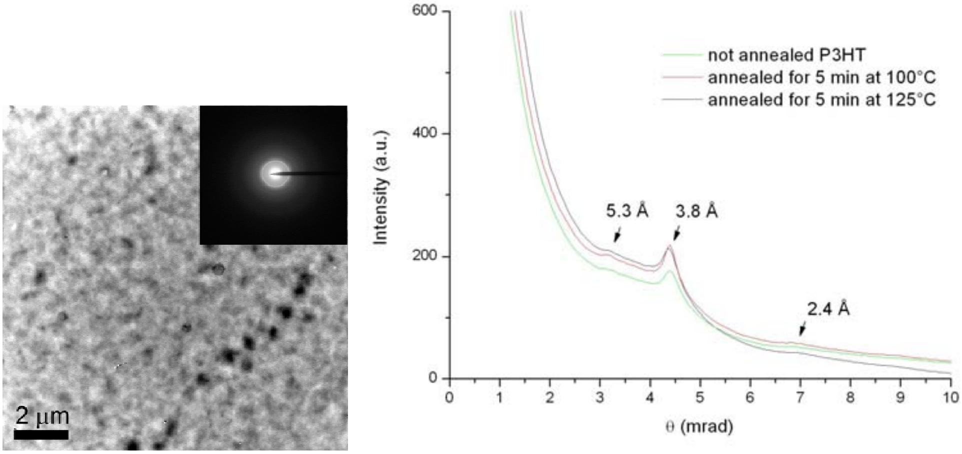

Figure 2.11: TEM image, corresponding diffraction pattern (left) of pristine P3HT and (right) intensity as a function of incident beam angle θ for pristine P3HT and annealed for 5 min at 100°C and 125°C.

The diffraction pattern of P3HT consists of a diffuse ring instead of distinct points, indicating the lack of crystallites. It is important to note that the diffuse ring present in non-annealed samples becomes a sharp diffraction ring at elevated temperatures, indicating the presence of more ordered regions. Having a look at Figure 2.11 right, a peak at 3.8 Å is found, attributed to the superposition of (020) and (002) plane.[11] Because both (020) and (002) reflections are close in the reciprocal space, they appear to merge into a single diffuse ring. Applying an annealing did not increase significantly the peak at 3.8 Å, although in the diffraction pattern the diffusive ring become more sharp with increased temperature treatment, indicating the intensity plot can only be analyzed qualitatively unless large differences are seen. At a d-value of 16.8 Å (100), no peak could be observed. SAED (see paragraph 2.1.1.2) is measured in transmission mode, making it impossible to locate the (100) plane. In addition to the peak at 3.8 Å, two smaller peaks are present at 5.3 Å and at 2.4 Å. The peak at 5.3 Å corresponds to two planes, i.e. (011) plane and (111) plane, while the peak at 2.4 Å corresponds to 8 planes, i.e. (20-3), (32-2), (013), (-113), (51-2), (700), (-213) and (30-3) plane. Since the diffraction pattern of P3HT consists of a diffuse ring it was impossible to address one single plane to the peak at 5.3 Å and one to the peak at 2.4 Å.

SAED was also performed on the spincoated PCBM, the corresponding intensities as a function of θ are shown in Figure 2.12. Three peaks are arising at 4.5 Å, 3.1 Å and 2.1 Å, which are in correspondence to the d-values found in literature reports for ordered PCBM molecules.[10] Our SAED observations are contradictory to the XRD measurements, which gave no evidence of crystalline material for spincoated PCBM. A possible explanation can be given by the small amount of material present in the sample, because only spincoated layers of 20 nm could be obtained with 1 weight % of solution. Thicker layers were hard to make because of solubility problems.

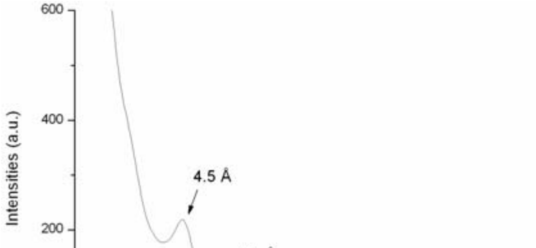

Figure 2.12: Intensity of diffraction pattern of spincoated pure PCBM as a function of θ.

2.2.1.2.2. P3HT:PCBM blends

In Figure 2.13, TEM images and corresponding diffraction patterns are shown for the 1:2 blend submitted to four annealing conditions: non-annealed, annealed during 5 min at 75°C, 100°C and 125°C. It is seen that the as-prepared non-annealed films are homogeneous: only a diffuse ring is seen in the corresponding selected area diffraction pattern. At lower annealing temperatures (i.e. 75°C and 100°C), small morphological differences are seen in the TEM images, indicated by the presence of brighter regions. These bright features increase in size with increasing temperature and become fiber-like structures at an annealing temperature of 125°C, Figure 2.13 (lower right). At an annealing temperature of 125°C, large needle shaped structures were seen (not shown) in addition to the fiber-like structures. These structures will be further described and investigated in the next paragraph.

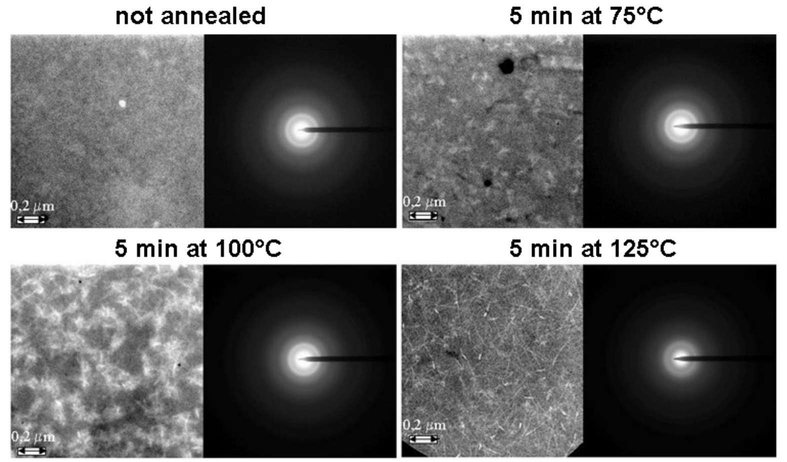

Figure 2.13: TEM images and diffraction patterns of P3HT:PCBM (1:2 blend) not annealed (upper left) and annealed during 5 min at 75°C (upper right), 100°C (lower left) and 125°C (lower right).

The intensity profiles are shown in Figure 2.14 (left) as a function of the incident beam angle θ. It is seen that it is hard to analyze these plots because of the large background signal present. To get a clearer view, the fitted inelastic scattering background, the one for amorphous materials gave the best fit, was subtracted from the intensity obtained in Figure 2.14. On the right side of Figure 2.14 the as-obtained residual intensities are plotted as a function of d-spacing.

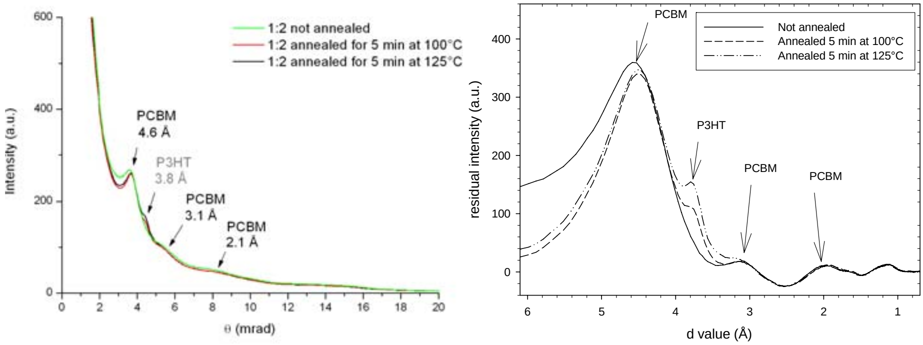

Figure 2.14: Intensity of TEM diffraction patterns of P3HT:PCBM 1:2 blend not annealed compared to annealed for 5 min at 100°C and 125°C as a function of θ (left) and corresponding residual intensities as a function of d-value (right).

Several peaks appear in Figure 2.14, which correspond to the diffraction rings, with average d-spacing at 4.6 Å, 3.8 Å, 3.1 Å and 2.1 Å. The broad peaks at 4.6 Å, 3.1 Å and 2.1 Å arise from the ordered PCBM molecules.[10] From the lack of micro-crystalline PCBM domains in the TEM images (Figure 2.13) and the presence of broad diffraction peaks, it can be concluded that nano-crystalline PCBM domains are homogeneously dispersed throughout the P3HT:PCBM film. For P3HT, an average interplanar distance (d-spacing) of 3.8 Å is found, attributed to the superposition of the (020) and (002) reflections from the crystal planes of semi-crystalline P3HT.[11] The intensity of the diffraction ring of P3HT at 3.8 Å clearly increases in intensity when the annealing temperature increased. This is attributed to the P3HT that is crystallizing during annealing. Secondly, the density of P3HT (1100 mg/cm^3)[12] is lower than the one from PCBM (1500 mg/cm^3)[13], so the brighter areas in TEM imaging probably correspond to P3HT-rich areas. Consequently, it can be assumed from these data that the bright features observed in Figure 2.13 are P3HT that crystallizes in the (020) and (002) direction, which are located perpendicular to the specimen (or parallel to the beam). Yang *et al.* and Savenije *et al.* also encountered a fiber-like formation of blended P3HT dissolved in 1,2-dichlorobenzene and chloroform.[14,15] Crystallization in the (100) plane could not be detected with SAED, because it measures in transmission, enabling to characterize only crystal planes perpendicular to BC plane of Figure 2.8. The TEM and XRD results suggest that the BC plane of the P3HT is parallel to the surface.

In the next paragraph, it will be demonstrated that prolonged annealing not only enhances the order of P3HT but will also lead to the crystallization of PCBM.

2.2.2. Crystallization of PCBM

The TEM-diffraction results presented in the previous paragraph did not only indicate the presence of ordered P3HT, but also the presence of nano-crystalline PCBM. Additionally, when the 1:2 P3HT:PCBM blended film was annealed for 5 min at 125°C, TEM showed the presence of large needle shaped structures (not shown in the previous paragraph). Therefore, optical microscopy was performed to investigate whether these large needle shaped structures also occurred in different blend ratios. On the optical microscopy images of the non-annealed films (Figure 2.15), the films annealed for 5 min at 75°C, and the films annealed for 5 min at 100°C, nothing special was noticed. Figure 2.16 shows the optical microscopy images of the P3HT:PCBM matrix with various PCBM ratios annealed for 5 min at 125°C, 150°C and 175°C.

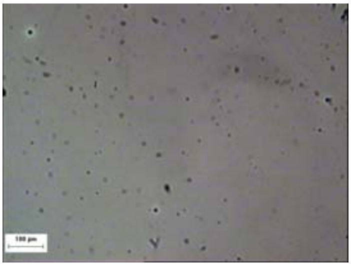

Figure 2.15: Optical microscopy image of the 1:1 P3HT:PCBM blend not annealed.

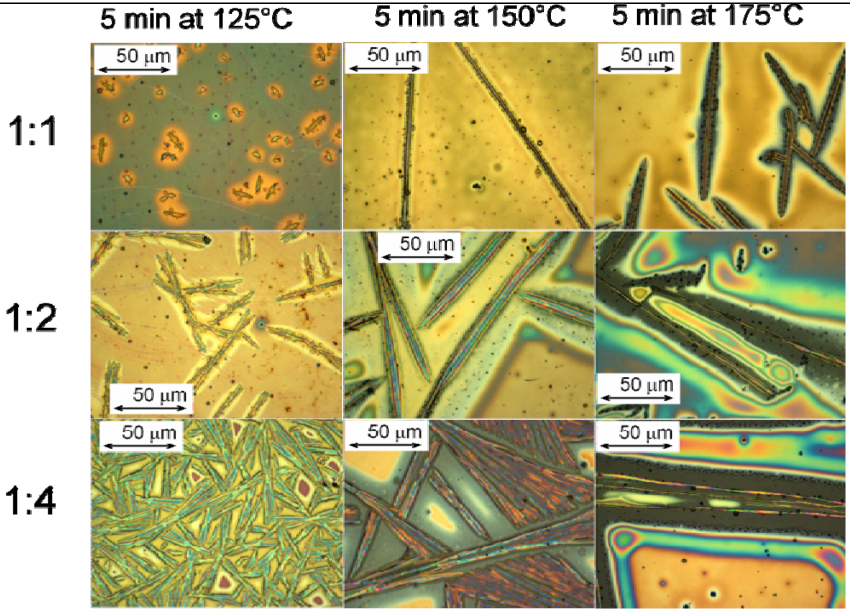

Figure 2.16: Optical microscopy images of spincoated P3HT:PCBM blend submitted to various annealing temperatures.

At a temperature of 125°C and a P3HT:PCBM ratio of 1:1, needle-like structures appear of a few 10 μm in length. These needles grow out to form a compact network for the 1:4 blend annealed for 5 min at 125°C, with lengths up to 100 μm. From these optical microscopy images the distribution of the length of the needles can be determined, as seen in Figure 2.17.

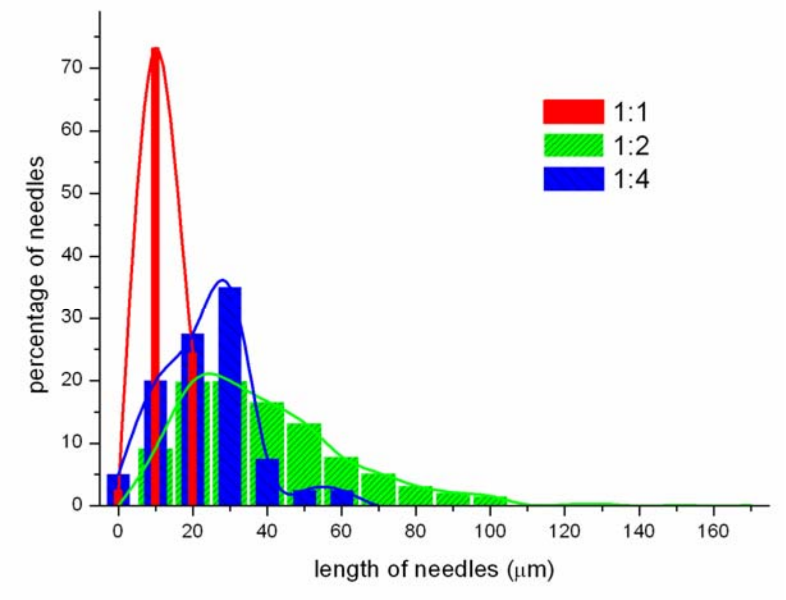

Figure 2.17: Distribution of the length of needles of 1:1, 1:2 and 1:4 P3HT:PCBM blends annealed for 5 min at 125°C.

Increasing the PCBM content from a 1:1 to a 1:2 ratio increases the average length of the needles from 10 μm to 30 μm with a broader distribution. A further increase of the PCBM content from 1:2 to 1:4 gives rise to a more narrow distribution of the needle length. The increase in average length of the needles with increasing PCBM content (from 1:1 to 1:2) is already an indication that the needle-like structures consist of PCBM. In the 1:2 blend, the needles are free to develop further upon annealing. For the 1:4 blend, the PCBM concentration is too high, limiting their free expansion upon annealing, resulting in a smaller uniform distribution of the average needle length and a corresponding two-dimensional network of PCBM needles. At higher temperatures (i.e. 150°C and 175°C), as expected, the needles exhibited much larger sizes.

AFM was used to characterize the height of these structures. Figure 2.18 shows the variations of height of the needles as a function of PCBM content for an annealing of 5 min at 125°C.

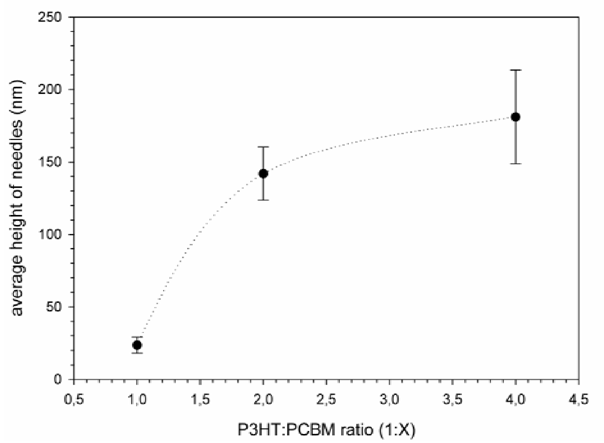

Figure 2.18: Average height of needles versus PCBM content for samples annealed for 5 min at 125°C.

The height, relative to the film surface, of these structures increases from 20 nm for the 1:1 blend to 180 nm for the 1:4 blend. The latter value is much larger than the initial film thickness of 100 nm, suggesting that as formed needles fully cross down to the glass substrate. During these experiments, a good reproducibility was obtained for the growth and the dimensions of these needles. Based on the reproducibility and the results of Figure 2.17 and Figure 2.18, it is therefore possible to tune the dimensions and spatial distribution of the needles through the appropriate choice of blend ratio and annealing conditions.

In order to determine the crystalline nature of these needle-like structures, SAED was performed on a needle (Figure 2.19 (B)). A clear electron diffraction pattern composed of many well-aligned spots is observed, indicating crystalline ordering in the needles observed in the TEM image (Figure 2.19 (A)).

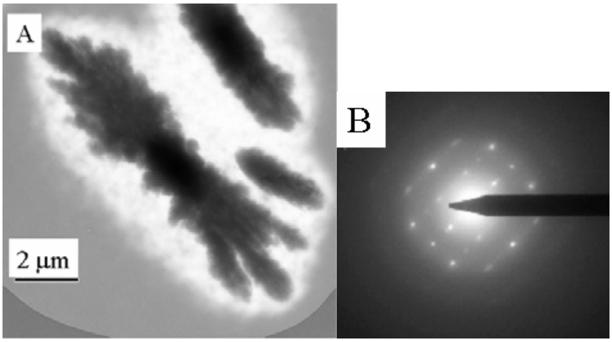

Figure 2.19: TEM image (A) and SAED diffraction pattern (B) of a needle in a P3HT:PCBM 1:2 blend annealed for 5 min at 125°C.

The d-values derived from this diffraction pattern are in agreement with literature data for triclinic PCBM[10], confirming that the observed needles are elongated PCBM crystals.

Annealing of the P3HT:PCBM blend does not only lead to crystallization of P3HT but also to the formation of large PCBM crystals. Dual crystallization is thus occurring. In literature, no reports have been given on structures of these dimensions. Nevertheless, much smaller PCBM crystals are confirmed by Chirvase *et al.* and Savenije *et al.* for P3HT:PCBM blends spincoated from chloroform.[15,16]

2.2.3. PCBM needles: diffusion

In order to elucidate the formation mechanism of these needles, samples were submitted to longer annealing times and investigated by different analytical techniques. First a closer look is taken to a PCBM needle formed when the blend was annealed for 4 hours at 100°C, shown in Figure 2.20 (A,B and C). Figure 2.20 (A) reveals that next to the crystalline PCBM needle a brighter region (region 2 in Figure 2.20) is seen, followed by a darker area (region 1 in Figure 2.20). Looking in more detail, Figure 2.20 (B,C) reveals the presence of a dense region with in-between a brighter region with nano-phase clusters (Figure 2.20 (C)).

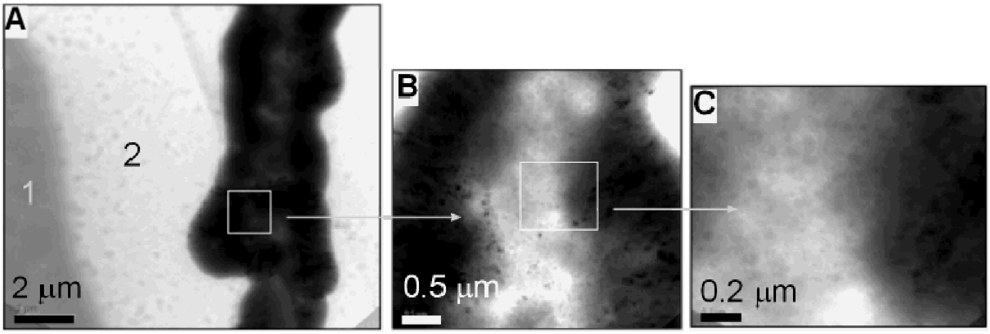

Figure 2.20: P3HT:PCBM 1:2 blend annealed for 4 hours at 100°C. Region 1: P3HT:PCBM matrix, region 2: brighter region next to the needle.

In TEM images, bright regions can be attributed to a lower mass density and/or a thinner film layer. The variations in thickness were investigated, using profilometry measurements. The height profile, obtained across two needles, is shown in Figure 2.21.

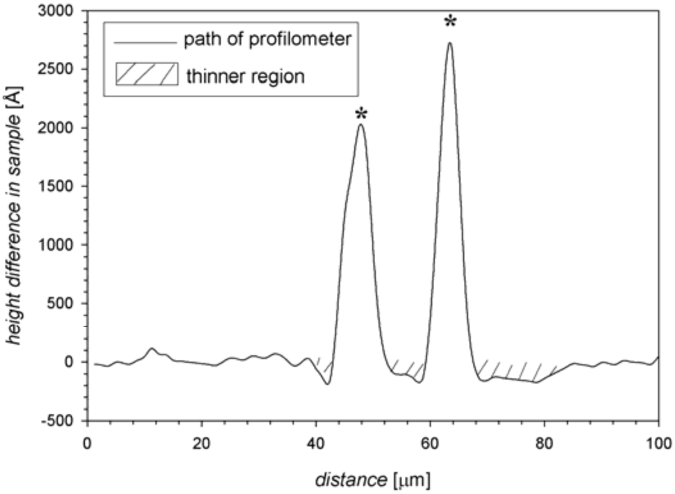

Figure 2.21: Profilometry measurement of two PCBM needles (*) present in a P3HT:PCBM (1:4) blend annealed for 5 min at 125°C. The height (in Å) is plotted versus the distance travelled by the profilometer needle (in μm).

The full line indicates the path of the profilometer. Next to the needle (shaded region), the film is 10-20 nm thinner than in the bulk. This thinning effect is even larger with increased temperature treatment and increased PCBM contents. Thus the diffusion of PCBM next to the needle occurs in a higher extend than the surrounding areas, where the PCBM content remains rather uniformly distributed. This depletion region was also encountered by Zhong *et al.* for PCBM crystals in MDMO-PPV:PCBM blends.[17] Furthermore, the lower mass density of P3HT in comparison with PCBM suggests that the bright region around the needle (region 2 in Figure 2.20) is a PCBM-depleted area.

Both explanations therefore suggest that the PCBM needles are formed by combination of local diffusion and crystallization of PCBM. SAED-patterns were taken to investigate the assumption that the bright region around the needle is a PCBM-depleted region. The intensities of the diffraction patterns at spot 1 and 2 in Figure 2.20 are shown in Figure 2.22 as a function of the incident beam angle. As a reference the intensities of the diffraction images of pure PCBM and P3HT are also plotted.

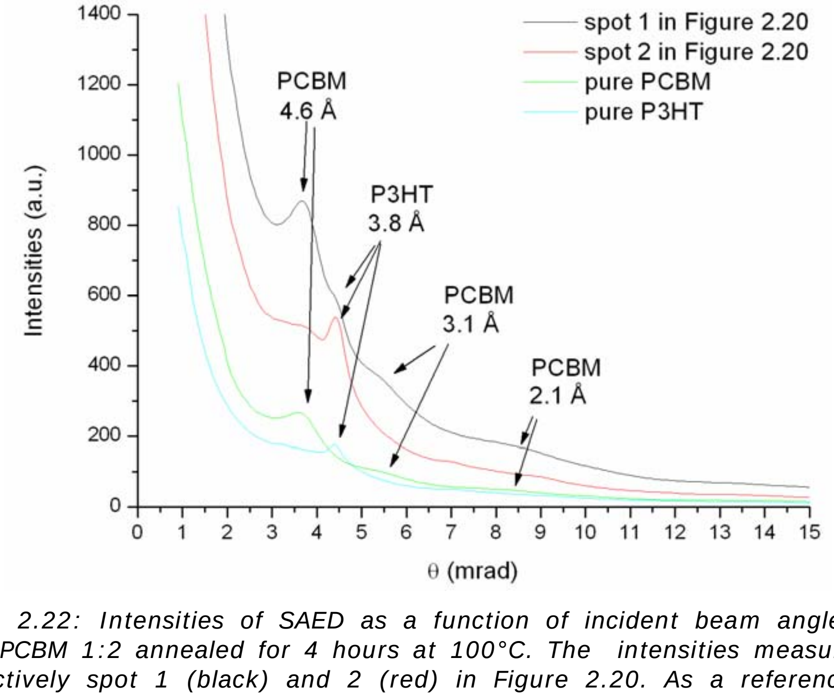

Figure 2.22: Intensities of SAED as a function of incident beam angle θ of P3HT:PCBM 1:2 annealed for 4 hours at 100°C. The intensities measured at respectively spot 1 (black) and 2 (red) in Figure 2.20. As a reference the intensities of pure PCBM (green) and pure P3HT (blue) are also plotted.

For spot 1 in Figure 2.22, three peaks appear at 4.6 Å, 3.1 Å and 2.1 Å corresponding to nano-crystalline PCBM molecules.[10] At an average interplanar distance (d-spacing) of 3.8 Å the profile exhibits a shoulder, attributed to the superposition of the (020) and (002) reflections from the crystal planes of semi-crystalline P3HT.[11] In the SAED pattern of the brighter region (region 2 in Figure 2.20), the peak at 3.8 Å has increased in intensity with a remaining shoulder at 4.6 Å, the PCBM peak position. The peak at 3.1 Å, originating also from PCBM has vanished, while the one at 2.1 Å still remains but is very broad. A possible explanation is that the peak at 3.1 Å is concealed by the large P3HT peak. So, the bright region consists of highly crystalline P3HT and few crystalline PCBM is remaining. This indicates that the bright region, surrounding the needles, is a PCBM-depleted area with highly crystalline P3HT, suggesting a diffusion-controlled growth of the PCBM needles.

Due to the kinetic nature of a diffusion process, the evolution of the morphology upon different annealing times was also investigated, see Figure 2.23.

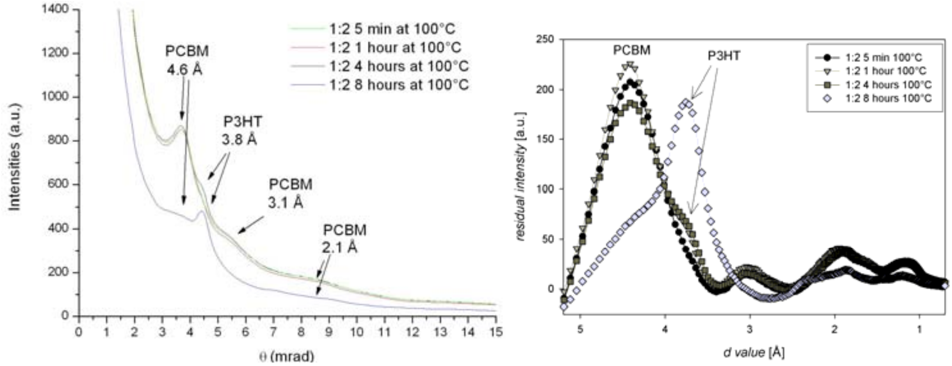

Figure 2.23: Comparison of residual intensity of SAED versus d-spacing of P3HT:PCBM 1:2 annealed for 5 min (•), 1 (▽), 4 (□) and 8 (◊) hours at 100°C.

The P3HT:PCBM 1:2 blend was annealed from 5 min to 8 hours at 100°C. Similar to the results shown in Figure 2.20 and Figure 2.22, TEM images and corresponding SAED analysis were performed away from the needles, i.e. in regions initially containing both P3HT and PCBM in the expected proportions, region 1, the so-called matrix, in Figure 2.19. The intensities and residual intensities of these SAED patterns are shown in Figure 2.23 (left and right corresponding). The major conclusion to be drawn from this figure is that after 8 hours almost all the PCBM has diffused out of the region, leaving highly crystalline P3HT in the “matrix”. The crystallization of P3HT (indicated by the presence of a peak at 3.8 Å) is shown to occur after 1 hour, and seems to contradict previous TEM observations (see Figure 2.13 and Figure 2.14) suggesting that this process already started after 5 min annealing. This appearing inconsistency is explained by the low intensity of the P3HT peak and therefore its ability to disappear in the large PCBM peak. Furthermore, the intensities were calculated by integrating over the diffraction rings, therefore some information can be lost. This implicates that the interpretation of these kinds of plots can only be qualitative and additional techniques should be used.

Because of this qualitative character and the possible loss of information during SAED analysis, a complementary technique is being used, i.e. confocal fluorescence microscopy. The fluorescence properties of P3HT combined with the large size of PCBM crystals allowed the characterization of the local spatial variations in emission.

Absorption measurements were performed on annealed and pristine pure P3HT, pure PCBM and the blended P3HT:PCBM 1:1 and 1:2 film, to determine the ideal excitation wavelength (Figure 2.24).

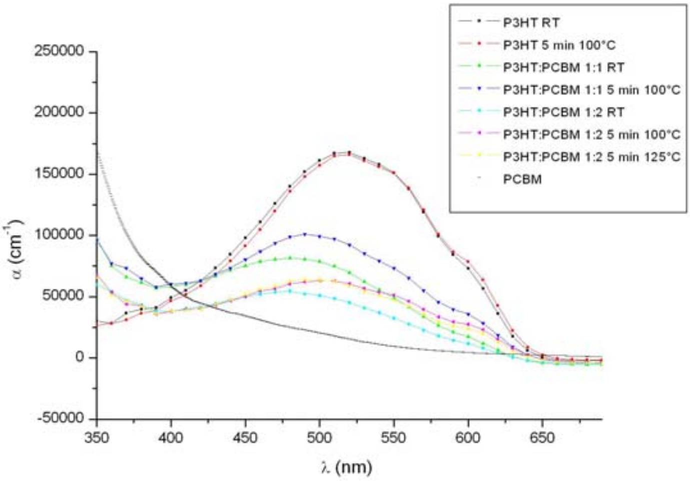

Figure 2.24: Absorbance(α) of pure P3HT, PCBM, P3HT blends not annealed and annealed for 5 min at 100°C and 125°C.

The pure non-annealed P3HT shows an absorption peak (λ_{max}) at 520 nm with a shoulder around 600 nm. With annealing this shoulder increases slightly in intensity, attributed to a more ordered P3HT. The absorption measurements show distinct differences upon blending with PCBM. A clear blue-shift of λ_{max} is observed when blended with PCBM, which is attributed to a reduced order in the semi-crystalline P3HT. In addition, the peak intensity lowers significantly. Figure 2.25 shows the influence of blending PCBM with P3HT on the fluorescence properties of P3HT, high fluorescence emission is depicted as yellow while the more fluorescence quenching observed the darker the image. It is shown that with addition of PCBM the fluorescence of P3HT (Figure 2.25 (a),(b) and (c)) is quenched and no fluorescence emission is observed for PCBM, shown in Figure 2.25 (d), under illumination of the Argon ion laser with a wavelength of 488 nm.

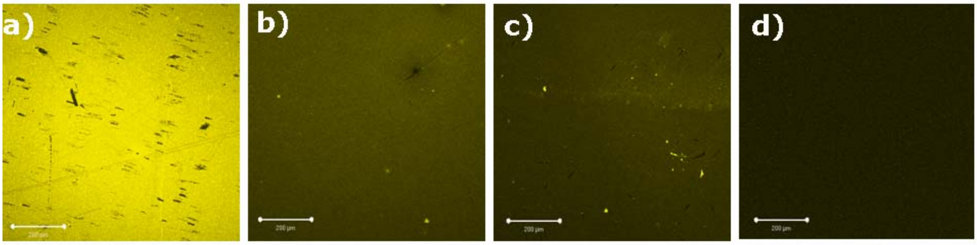

Figure 2.25: Fluorescence images of pristine (a) P3HT, (b) 1:1 P3HT:PCBM, (c) 1:2 P3HT:PCBM and (d)PCBM.

With annealing, the spectra of the blended P3HT resemble more and more those of the pure material. Hence, order in P3HT can be regained by annealing, as observed in the previous paragraphs. The emission was detected through a high pass filter of 505 nm. Figure 2.26 shows the transmission images (A,C) and fluorescence images (B,D) of the P3HT:PCBM 1:2 film annealed for 4 hours (A,B) and 8 hours (C,D) at 100°C.

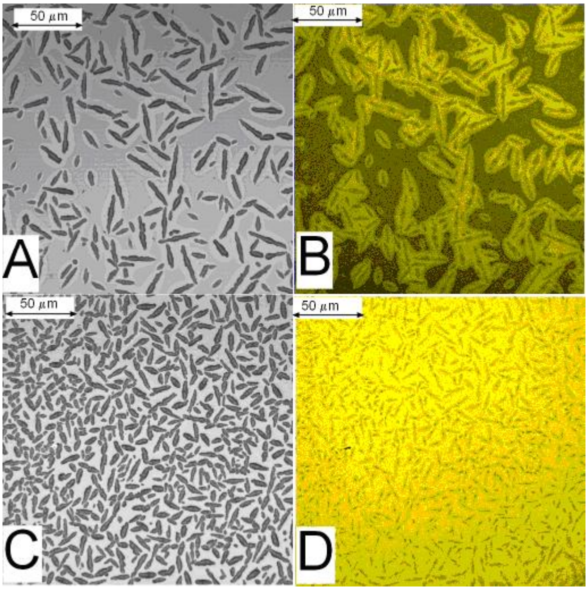

Figure 2.26: Transmission (A,C) and fluorescence (B,D) images of P3HT:PCBM 1:2 annealed for 4 hours (A,B) at 100°C and for 8 hours (C,D) at 100°C.

In Figure 2.26 (B), around to the PCBM needles little fluorescence quenching is observed. This confirms the TEM observation that this region is in fact a PCBM-depleted region. Next to these bright regions, P3HT:PCBM areas are found with a very low fluorescence emission. Their intensity is about the same as for the pixels related to the PCBM needles. The sample annealed for 8 hours at 100°C (Figure 2.26 (C,D)), reveals a highly fluorescent matrix, thus pure P3HT and low fluorescent PCBM needles. The fluorescence measurements are therefore complementary to the previous SAED analysis, and reveal that after sufficiently long annealing most of the PCBM crystallized in the needles.

2.2.4. Formation of PCBM needles instead of blob-like PCBM crystals

It is confirmed by Yang *et al*. that pure PCBM can crystallize when slow evaporation is used, while for MDMO-PPV blended systems additional annealing was used.[17-20] The formation of PCBM crystals in the MDMO-PPV blend arises from long annealing times (i.e. 60 min) at high temperatures (i.e. 130°C). The shape of the crystalline structures obtained in both systems appear like spherical blobs on the order of a few micrometers in size.

Question still remains whether the crystalline organization of P3HT enhances the formation of PCBM needles instead of blobs as observed in MDMO-PPV blends. To clear out this issue, regiorandom P3HT, see Figure 2.27, was blended in different (1:1, 1:2 up to 1:4) ratios with PCBM and submitted to equal annealing conditions as for the regioregular P3HT blends.

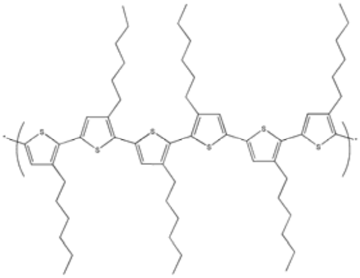

Figure 2.27: Chemical structure of regiorandom P3HT.

Because of the random positioning of hexyl side chains for regiorandom P3HT, its ability to crystallize is hampered. Steric hinderance of the alkyl side-chains makes it impossible to organize. In contrary to the regioregular blend, the regiorandom blend did not show any needle formation in the 1:1 blend for all annealing conditions. However, the 1:2 and 1:4 blend ratio, for which the optical images are given in Figure 2.28, did show similar structures as encountered for the regioregular blend, disproving the assumption that the crystallization of

P3HT is responsible for the formation of the PCBM needle-like structure in the regioregular blend (instead of blobs).

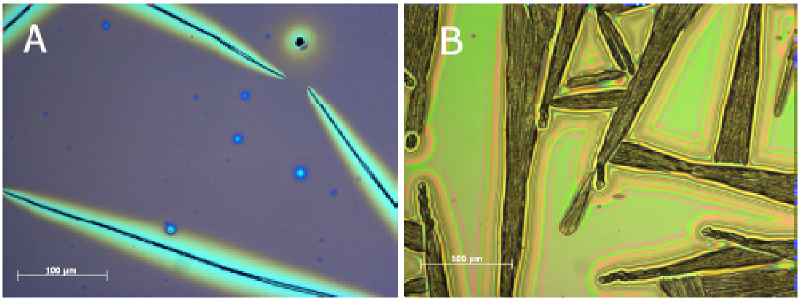

Figure 2.28: Optical microscopy images of regiorandom P3HT:PCBM annealed for 5 min at 150°C in a 1:2 blend ratio (A) and a 1:4 blend ratio (B).

So it can be concluded that the crystallization of regioregular P3HT does not act as a kind of template to form these needle-like structures. A possible explanation, for the difference in structures encountered when blended with MDMO-PPV, can be found in the start morphology of both systems. For MDMO-PPV blended with PCBM, phase separation occurs in the film and thus a PCBM-rich phase is formed. Hence, PCBM crystal growth within PCBM rich phase is favored, making it easier to form blob-like crystals. Blended with P3HT, the PCBM is almost equally dispersed over the film. Additionally, MDMO-PPV has a higher T_g (around 50°C) and M_w than P3HT (around 12°C) therefore being less mobile at temperatures of around 130°C.

2.2.5. Cross-sections of P3HT:PCBM solar cell

In the previous paragraphs morphology study was always performed on P3HT:PCBM layer spincoated on glass substrates. Hence, the question arose whether these PCBM needles would also be encountered in solar cell devices. A full solar cell with a blend ratio of 1:2 P3HT:PCBM was fabricated, as described in chapter 4 paragraph 4.2.2.2. The solar cell was annealed on a hotplate in nitrogen atmosphere for 24 hours at 100°C to be sure that the PCBM crystals would be present. Figure 2.29 (a) shows the solar cell obtained after annealing for 24 hours at 100°C. It is seen that the Al contact has blistered. A closer look has been taken with optical microscopy, shown in Figure 2.29 (b), revealing the presence of PCBM crystals. This was also observed by Chirvase *et al.*.[16]

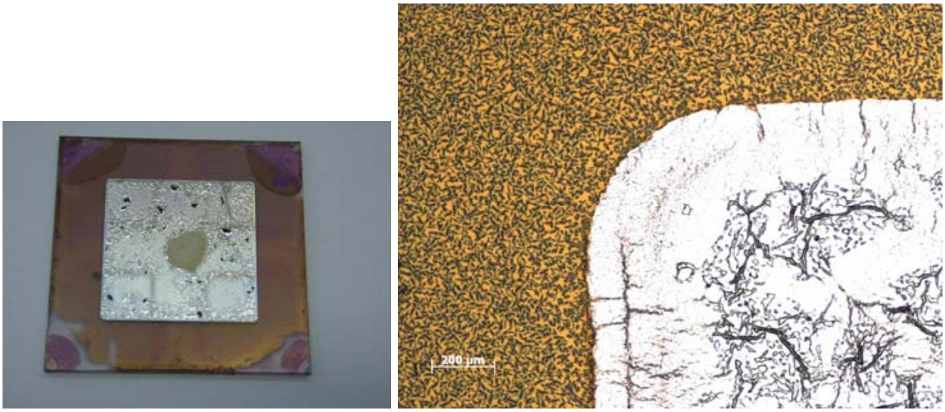

Figure 2.29: Photo of the P3HT:PCBM 1:2 solar cell annealed for 24 hours at 100°C (a) and corresponding optical microscopy image (b).

With focused ion beam (FIB) a cross section was made, which was studied with TEM, as shown in Figure 2.30 (a, b and c). Figure 2.30 (b) and (c) show the cross-section across a PCBM needle. The PEDOT:PSS layer is indicated by the region between the dotted vertical lines, a thickness of around 50 nm is found. On top of this layer a 100 nm thick P3HT:PCBM layer is found (between dashed and full line). A PCBM needle is indicated by the region between the full line and the white line in Figure 2.30 (b). A gradual height transition is observed out of the P3HT:PCBM blend.

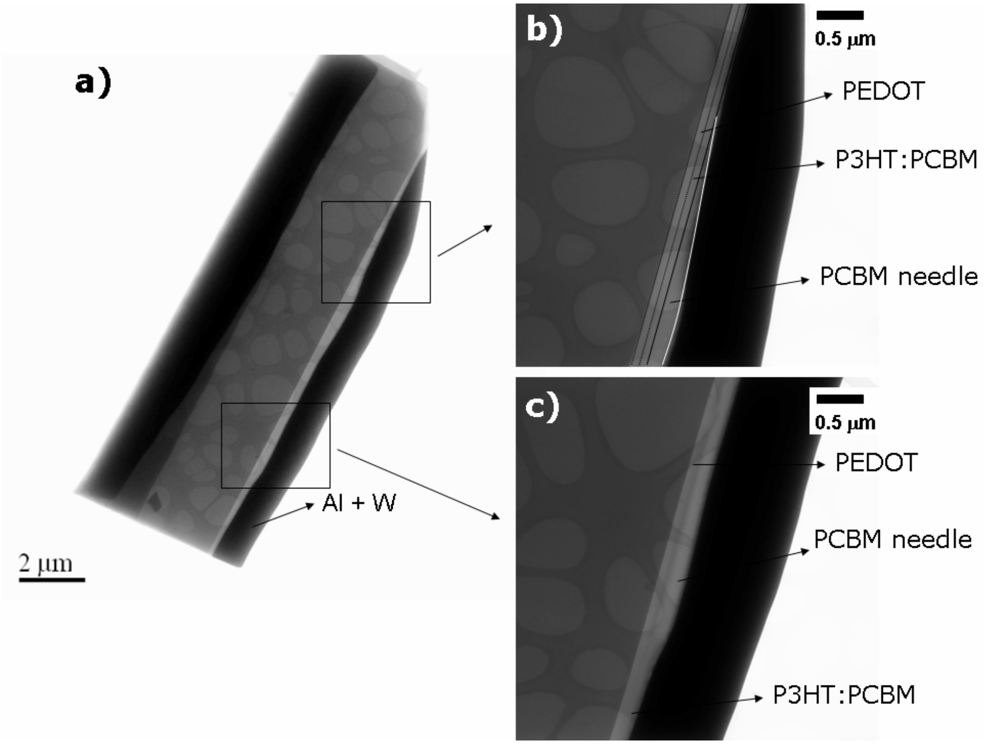

Figure 2.30: TEM image of FIB cross section of 1:2 P3HT:PCBM solar cell annealed for 24 hours at 100°C.

2.3. Conclusion

A systematic morphology study was performed on the P3HT:PCBM system for different blend ratios and various annealing conditions. The P3HT:PCBM film morphology was probed with optical microscopy, AFM, XRD, TEM and confocal fluorescence microscopy imaging. Three cases can be described. First, the non-annealed pure P3HT can be described as a semi-crystalline polymer. With addition of PCBM, this crystallization is hampered resulting in an amorphous blend for the 1:4 blend ratio. For 1:1 and 1:2 blends, the P3HT retains some crystalline order and PCBM is present as nano-crystalline regions, as seen in Figure 2.31.

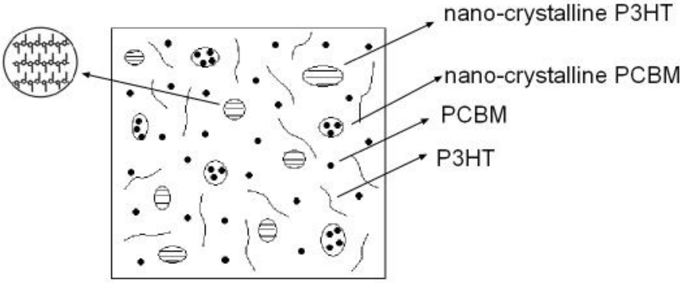

Figure 2.31: Schematic drawing of P3HT:PCBM blend morphology non-annealed.

Secondly, when mild (i.e. 5 min at 100°C and 125°C) annealing conditions are applied, P3HT regains more crystalline order.

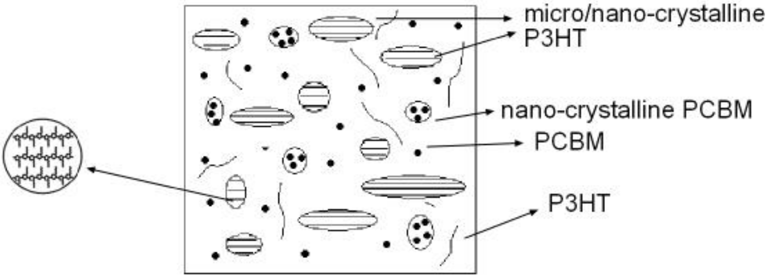

Figure 2.32: Schematic drawing of P3HT:PCBM blend morphology submitted to mild annealing conditions.

Thirdly, additionally to the crystallization of P3HT, PCBM starts to form needle-like crystals, as seen in Figure 2.33, at a temperature treatment of 5 min at 125°C. With addition of PCBM and increased annealing temperature, these needles grow and can even form fan-shaped structures and a compact network. Structures of a few mm in length and up to 180 nm in thickness, were obtained in this way. Changing blend composition and annealing treatments can be used to tune the dimensions of these structures.

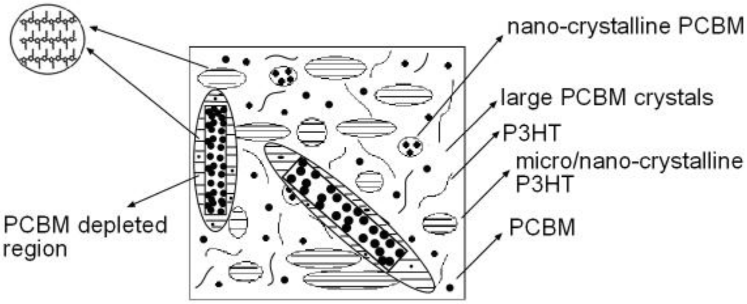

Figure 2.33: Schematic drawing of P3HT:PCBM blend morphology submitted to severe annealing conditions.

The needle itself consists of a dense border with in-between nano-crystalline PCBM regions. The crystalline nature of the needle was demonstrated by SAED to be conform with the triclinic lattice of PCBM. The needle was found to be surrounded by a thinner PCBM-depleted region, consisting of highly crystalline P3HT. With annealing treatment, the PCBM diffuses thus out of the matrix towards the needle. At short elevated temperature treatments and long (typically a few hours) treatments at lower temperatures, a morphology with almost pure highly crystalline P3HT regions in-between of large PCBM crystalline needles is achieved.

The formation of these PCBM needle crystals instead of blob shaped crystals, encountered with MDMO-PPV blends, can be attributed to the difference in starting morphology of MDMO-PPV in combination with the lower T_g of P3HT. Hence, it was proven that it is not the crystallization mechanism of P3HT that is responsible for the shape of the PCBM crystals.

Finally, it was proven that these crystals are also formed in solar cell devices. A cross section could be made and was studied with TEM. The crystals grow trough the Al contact, resulting in blisters and cracks in the Al, impeding a correct operation of the solar cell.

It can be concluded that although this system gives rise to the highest efficiencies ever obtained in this class of solar cells, the morphology of the

P3HT:PCBM system can drastically change during annealing. Therefore it is not at all a thermal dynamic stable system and thus not an ideal candidate for bulk-heterojunction solar cells with a long-term stability and reliability. Nevertheless, the demonstrated ability to tune the dimensions of needle-like PCBM crystals through appropriate blend ratio and annealing conditions opens a new route to obtain (nano-)structuring. Since (nano-)structuring is of great importance for novel organic and hybrid electronic applications, future work will consist of ordering in two or even three dimensions of these crystalline needles.

2.4. References

[1] F. Padinger, R. S. Rittberger, N. S. Sariciftci, *Adv. Funct. Mater.*, **13**, 2003, 85.
[2] http://www.spmtips.com
[3] J. A. Merlo, C. D. Frisbie*, J. Phys. Chem. B,* **108,** 2004, 19169.
[4] S. Hugger, R. Thomann, T. Heinzel, T. Thurn-Albrecht, *Colloid Polym. Sci.*, **282**, 2004, 932.
[5] Y. Zhao, G. Yuan, P. Roche, M. Leclerc, *Polymer*, **36**, 1995, 2211.
[6] T. A. Chen, X. Wu, R. D. Rieke, *J. Am. Chem. Soc.*, **117**, 1995, 233.
[7] R. D. McCullough, S. Trtstram-Nagle, S. P. Williams, R. D. Lowe, M. Jayarman, *J. Am. Chem. Soc.*, **115**, 1993, 4910.
[8] M. J. Winokur, T. J. Prosa, J. Moulton, P. Smith, A. J. Heeger, *Macromolecules,* **25**, 1992, 4364.
[9] T. Erb, U. Zhokhavets, G. Gobsch, S. Raleva, B. Stuhn, P. Schilinsky, C. Waldauf, C.J. Brabec, *Adv. Funct. Mater.,* **15**, 2005, 1193.
[10] M. T. Rispens, A. Meetsma, R. Rittberger, C. J. Brabec, N. S. Sariciftci, J. C. Hummelen, *Chem. Commun.*, **17**, 2003, 2116.
[11] K. J. Ihn, J. Moulyon, P. Smith*, J. Polym. Sci. Part –B Polym. Phys.*, **31**, 1993, 19714.
[12] T. J. Prosa, M. J. Winokur, J. Moulton, P. Smith, A. J. Heeger, *Macromolecules* **25**, 1992, 4364.
[13] C. W. Bulle-Lieuwma, W. J. van Gennip, J. K. Van Duren, P. Jonkheijm, R. A. Janssen, J. W. Niemantsverdriet, *Appl. Surf. Sci.*, **203**, 2003, 547.
[14] X. N. Yang, J. Loos, S. C. Veenstra, W. J. H. Verhees, M. M. Wienk, J. M. Kroon, M. A. J. Michels, R. A. J. Janssen, *Nano Lett.,* **5**, 2005, 579.
[15] T. J. Savenije, J. E. Kroeze, X. N. Yang, J. Loos, *Adv. Funct. Mater.,* **15**, 2005, 1260.
[16] D. Chirvase, J. Parisi, J. C. Hummelen, V. Dyakonov, *Nanotechnology,* **15**, 2004, 1317.
[17] H. Zhong, X. Yang, B. deWith, J. Loos, *Macromolecules,* **39**, 2006, 218.
[18] X. Yang, J. K. J. Van Duren, M. T. Rispens, J. C. Hummelen, R. A. J Janssen, M. A. J. Michels, J. Loos, *Adv. Mater.*, **16**, 2004, 9.
[19] X. Yang, J. K. J. Van Duren, R. A. J. Janssen, M.A. J. Michels, J. Loos, *Macromolecules,* **37**, 2004, 2151.
[20] X. Yang, A. Alexeev, M. A. J. Michels, J. Loos, *Macromolecules,* **38**, 2005, 4289.

3. State diagram of P3HT:PCBM system

From the morphological investigations in chapter two on P3HT:PCBM blends, dual crystallization behavior of both blend components upon annealing was observed. In order to clearly understand why this type of morphology is formed and how it can be tuned, the phase behavior needs to be described in terms of the underlying thermodynamic mechanisms. A first step in this study, is obtaining a state diagram of P3HT:PCBM blend. Therefore, in this chapter first an introduction is given of how the phase diagram should look like for this type of polymer blend systems. Secondly, the techniques used for thermal analysis like Differential Scanning Calorimetry (DSC) and Modulated Temperature DSC (MTDSC) are described. Results are presented, beginning with the pure components, followed by the experiments performed on blends ranging from 0% to 100% PCBM. The evolution of the glass transition temperature, crystallization temperature and melting temperature for different P3HT:PCBM ratios was found and as conclusion an experimental state diagram is shown.

3.1. Phase diagram of conjugated polymer:PCBM blends

In chapter one, a detailed description was made of all the morphology studies performed until now on the “reference” blend system MDMO-PPV:PCBM and the different parameters influencing morphology like solvent choice, blending ratios, annealing and processing parameters. Hoppe *et al.* was the first to report how a phase diagram for this type of blend should be composed.[1] A ternary phase diagram is needed according to Hoppe *et al.*, as seen in Figure 3.1. A constant temperature and pressure was assumed. The black dot indicates a solution with an initial concentration of solvent (2), polymer (3), and fullerene (1). Since it is know that MDMO-PPV:PCBM blend can phase separate, a two phase region is indicated on the phase diagram. The limited solubility of PCBM leads to the solubility limit indicated in Figure 3.1. For ternary solutions within the 2-phase region, phase separation will occur, leading to the precipitation of PCBM. Since phase separation is a time and temperature dependent process, the morphology of a MDMO-PPV:PCBM blend can be rapidly frozen in by fast solvent evaporation (spincoating), giving a meta-stable state. This meta-stable state can consist of phase separated regions or a perfectly homogeneous blend depending on the solvent evaporation speed and the initial concentration of fullerene and polymer. When slow evaporation is used, as with dropcasting, the polymer and fullerene are mobile for a longer time, enabling the phase separation to proceed. Nevertheless, even for a frozen in homogeneous blend, applying a temperature treatment can still increase the mobility of the fullerene and MDMO-PPV molecules enabling the diffusion of PCBM and the formation of PCBM crystals.

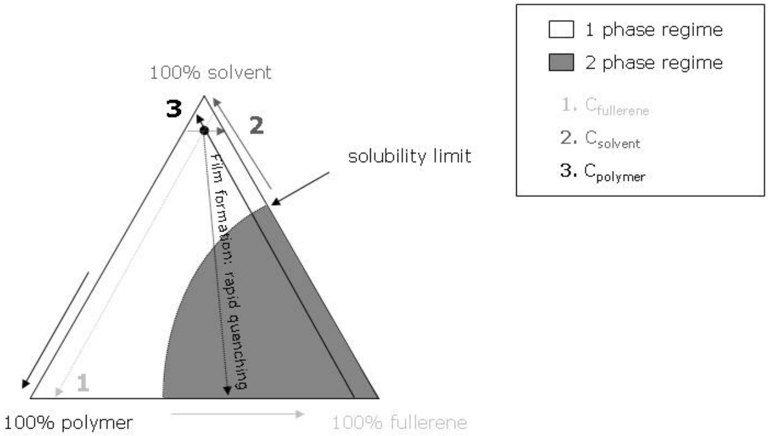

Figure 3.1: Ternary phase diagram of MDMO-PPV:PCBM:solvent system at a constant pressure and temperature. The arrows indicate the direction of increased concentration and point 1, 2 and 3 are the initial concentration of fullerene, solvent and polymer respectively in the solution. During film formation a quenching of the solution takes place towards solid state blend upon evaporation of the solvent.

The MDMO-PPV:PCBM blend was shown to phase separate, in contrast to the P3HT:PCBM blend were, as demonstrated in chapter two, only crystallization occurs of both components. Hence, the P3HT:PCBM system will have a totally different phase diagram. In the ternary phase diagram of Hoppe *et al.*, the temperature was assumed to be constant and the morphology development results from the solvent evaporation-induced phase separation. In our study, the morphology development results from crystallization, and thus the temperature will play a crucial role. The influence of solvent will be disregarded. Since, it is a quite complex system and no full thermodynamic studies have been performed, it is hard to give an intuitive overview of how the phase diagram will look like. Here the initial results will be shown for DSC and MTDSC measurements with one type of solvent, resulting in a 2D state diagram which already will give a good impression of how this blend behaves thermodynamically.

3.2. Differential scanning calorimetry (DSC)

3.2.1. *Traditional differential scanning calorimetry*

Differential scanning calorimetry (DSC) is a technique used to study thermal transitions in a polymer.[2] The difference in heat flow (HF) between a sample and an inert reference is monitored while applying a linearly changing or isothermal temperature program. Qualitative and quantitative information about physical and chemical changes that involve endothermic or exothermic processes, or heat capacity changes (only valid for non-isothermal measurements), are obtained in this way.

Heat flux DSC and power compensation DSC are two main types of differential scanning calorimeters (Figure 3.2).[3,4] In a heat flux DSC, the sample crucible and reference crucible, with a comparable weight as the sample crucible, are positioned symmetrically on a shared heat flux plate, generating a controlled heat flux from the furnace wall to the sample and reference. Using a thermocouple, the temperature difference between the crucibles is measured, which can be related to the heat flow to the sample by the following relationship:

$$\frac{dQ}{dt} = \frac{\Delta T}{R} \qquad \textit{equation 3-1}$$

With: dQ: the amount of heat (in Joule) transferred to the sample in a time interval dt (in seconds)

R: the thermal resistance of the cell (in Kelvin.Watt^{-1})

ΔT: the temperature difference between sample and reference

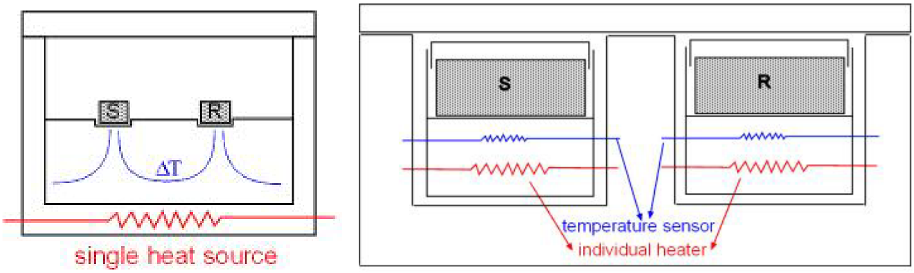

Figure 3.2: Schematic drawing of a heat flux DSC (left) and power compensation DSC (right) with S (sample) and R (reference) crucibles.

In contrast to heat flux DSC, sample and reference are isolated from each other in a power compensation DSC. The sample crucible as well as the reference crucible, have their own heating and temperature sensing element. The heating flux of the samples is externally controlled to obtain a constant heating rate of the sample and the reference. Both the sample and reference are maintained at the same temperature while monitoring the electrical power used by their heaters. The heat flux to the sample is the difference in power applied to sample and reference.

For both techniques, the resulting heat flow signal can be described with following equation:

$$\frac{dQ}{dt} = c_p \frac{dT}{dt} + f(t,T) \qquad \textit{equation 3-2}$$

With c_p the baseline heat capacity, dT/dt the heating rate of the experiment and f(t,T) the time- and temperature-dependent contribution describing the kinetic response of any physical or chemical transformation (in Watt). The first term is heat capacity related, while the second term contains kinetic information on thermal processes in the material.

3.2.2. Modulated temperature differential scanning calorimetry (MTDSC)

For measurements of the glass transitions, modulated temperature differential scanning calorimetry (MTDSC) was used. MTDSC is a variation of traditional DSC were a sinusoidal wave, with an amplitude A_T (K) and an angular frequency ω (s^{-1}), is superimposed on the isothermal or linearly changing temperature program [5,6]:

$$T = T_0 + \beta t + A_T \sin(\omega t) \qquad \textit{equation 3-3}$$

With T the temperature (K), T_0 the initial temperature (K) at the beginning of the experiment, t the time (s) and β the heating rate (K/s). The modulated heating rate will be given by the time derivative of equation 3-3:

$$\frac{dT}{dt} = \beta + A_T\, \omega \cos(\omega t) = \beta + A_{HR} \cos(\omega t) \qquad \textit{equation 3-4}$$

Hence, the modulated heating rate consists of the original (underlying) heating rate β plus an alternating heating rate A_{HR} cos(ωt). Consequently, this modulated temperature program (input) results in a modulated heat flow response (output),[5,6] using equation 3-2 and 3-4, of:

$$\frac{dQ}{dt} = c_p(\beta + A_T\, \omega \cos(\omega t)) + f(t,T) \qquad \textit{equation 3-5}$$

Or if [1] is fulfilled:

$$\frac{dQ}{dt} = c_p\,\beta + c_p\,A_T\,\omega\cos(\omega t) + f'(t,T) + A_K\,\sin(\omega t) \qquad \textit{equation 3-6}$$

with f'(t,T) the average underlying response of a kinetic phenomenon once the effect of the sine wave is subtracted and A_K the amplitude of the kinetic response to the sine wave modulation. In traditional DSC, the sum of the heat capacity term as well as the kinetic term are being measured, making it sometimes impossible to interpret results when two or more transitions are occurring at the same time or temperature. In MTDSC this is overcome by calculating both components. The modulated heat flow is measured (Equation 3-6) and can be separated in two contributions: the total heat flow depending on the average underlying temperature is obtained by applying an averaging process that effectively subtracts the effect of modulation:

$$\frac{dQ}{dt}_{tot} = c_p\,\beta + f'(t,T) \qquad \textit{equation 3-7}$$

, which corresponds to the signal obtained by conventional DSC, and the cyclic heat flow, obtained by subtracting the total heat flow (equation 3-7) from the modulated heat flow (equation 3-6):

$$\frac{dQ}{dt}_{cycl} = c_p\,A_T\,\omega\cos(\omega t) + A_K\,\sin(\omega t) \qquad \textit{equation 3-8}$$

To evaluate the magnitude of this cyclic component, the amplitude of the first harmonic is calculated using a Fourier deconvolution. Comparing the amplitude of the cyclic heat flow, A_{HF}, and the amplitude of the cyclic heating rate, A_{HR} (= $A_T\omega$), gives rise to an additional signal, i.e. the MTDSC heat capacity $c_{p,MTDSC}$ in J/K:

$$c_{p,MTDSC} = \frac{A_{HF}}{A_{HR}} = \frac{A_{HF}}{A_T\,\omega} \qquad \textit{equation 3-9}$$

This signal also called reversing or complex heat capacity will be further noted as heat capacity or c_P.

---

[1] Equation 3-6 is correct if the assumption is made that the temperature modulation is small and that over the interval of modulation the response of the rate of kinetic process to temperature is linear.

The reversing heat flow ($\frac{dQ}{dt}_R$ in W) is subsequently given by the multiplication of the heat capacity and the imposed underlying heating rate:

$$\frac{dQ}{dt}_R = c_p \beta \qquad \textit{equation 3-10}$$

The non-reversing heat flow ($\frac{dQ}{dt}_{NR}$ in W) is obtained by subtracting the reversing heat flow from the total heat flow:

$$\frac{dQ}{dt}_{NR} = \frac{dQ}{dt}_{tot} - \frac{dQ}{dt}_R \qquad \textit{equation 3-11}$$

The simultaneous monitoring of heat flow and heat capacity is a major advantage of MTDSC, as it allows detecting overlapping thermal events (e.g. glass transition and enthalpy relaxation).[7] In addition, a good signal-to-noise ratio is obtained for the heat capacity signal, because it is calculated from the cyclic signals. Hence, the detection of small heat capacity changes over long time spans is feasible.

3.2.3. *Observation of transitions by DSC and MTDSC*

The glass transition, melting and crystallization are the three major transitions that can occur in polymers. Glass transitions (T_g) occur as the temperature of an amorphous solid is increased. Below the glass transition, the amorphous polymer is in a glassy solid-like state. As the temperature is increased the thermal energy of the polymer molecules increases. At a certain temperature the thermal energy of the molecules will be sufficient to enable the cooperatice movement of 30-50 chain segments. As a result, the polymer changes to a viscous melt or rubbery state. The gain in mobility leads to a step increase in heat capacity. As the temperature further increases, an amorphous solid will become less viscous. A glass transition appears as a step in the baseline of the recorded DSC signal (Figure 3.3). This is due to the sample undergoing a change in heat capacity, but no formal phase change occurs.[1,3]

At some point during heating the molecules will obtain enough freedom of motion to spontaneously arrange themselves into a crystalline form (for crystalizable polymers only). This is termed cold crystallization, in contrast to melt crystallization that occurs upon cooling from the melt state. This transition from amorphous solid to crystalline solid is an exothermic process, and results in a peak in the DSC signal, as seen in Figure 3.3. As the temperature increases, the sample eventually reaches its melting temperature (T_m). The melting process results in an endothermic peak in the DSC curve (Figure 3.3 (left)). In

MTDSC, the heat capacity increase at T_g is observed in the heat capacity signal (Figure 3.3 (right)).[4] As the signal-to-noise ratio of this signal is higher, the transition is more easily observed than in conventional DSC. Crystallization is observed in the non-reversing heat flow. Melting in observed in both heat capacity and non-reversing heat flow.

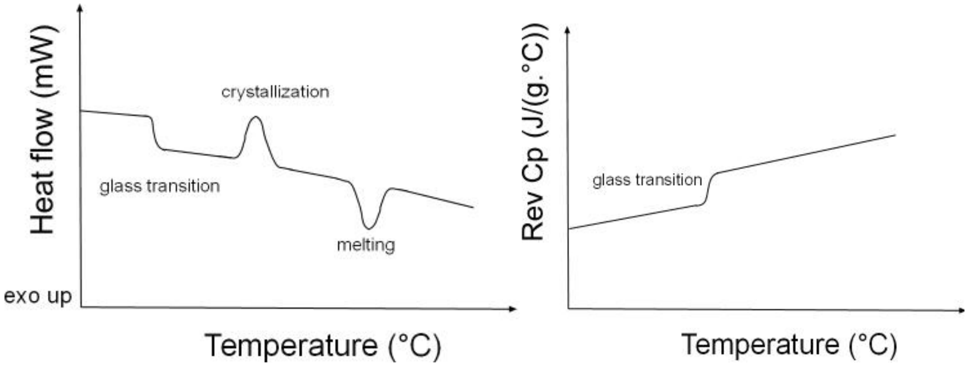

Figure 3.3: Schematic DSC curve (left) demonstrating the appearance of several common features occurring upon heating a crystallisable polymer that was rapidly cooled to an amorphous glassy state. Schematic of MTDSC (right) of heat capacity signal demonstrating the appearance of a glass transition.

3.3. DSC analysis

3.3.1. Experimental

3.3.1.1. Sample preparation

Blends of different weight ratios P3HT (Merck, M_w = 35000 g/mol and PD = 1.842) with PCBM (Solenne), from 0 wt% to 100 wt% PCBM, were dissolved in chlorobenzene and dropcasted on large glass plates. The samples were dried in a nitrogen atmosphere at room temperature for 50 hr to remove the remnant solvents. The remaining solid films were scratched off, giving the blends in powder form.

3.3.1.2. Thermal analysis

DSC measurements in both standard and modulated modes were made on TA Instruments 2920 DSC equipped with a Refrigerated Cooling System, and purged with helium (50 ml/min). Indium was used for temperature (combined with a second material cyclohexane or gallium) as well as enthalpy calibration. The heat capacity was evaluated with respect to poly(methyl methacrylate) (PMMA) as a standard. About 5 mg samples were sealed in perforated aluminum crucibles (Mettler, 40 µL). Oxidation of the sample was avoided by using perforated crucibles in the helium-purged DSC cell. For the standard DSC measurements, the scanning rate was set to 10 °C/min for both heating and cooling runs. First, all the samples were heated up from -50 °C to 310 °C and kept at 310 °C for 1 min to get a completely molten state. Subsequently, they were cooled down to -50 °C. Finally, they were heated up to 310 °C again. To determine the maximum heating temperature, the thermal stability was checked with DSC and Thermogravimetric analysis. Due to the complicated thermal history of the as-prepared samples and their poor contact with the crucibles in the first heating, the first cooling and the second heating are used for discussion. For the MTDSC measurements, the modulation amplitude was set to 0.5 °C with a period of 60 seconds. Samples of 3-5 mg were introduced in perforated aluminium crucibles (Mettler, 40 µL). First, all samples were molten at 300 °C for 3 min. Subsequently some of them were quenched in the DSC cell at about 100 °C/min directly to -50 °C. Finally, they were heated up to 300 °C at 2.5 °C/min. And then some of them were quenched in DSC cell at about 100 °C/min directly to -50 °C. Finally, they were heated up to 300 °C at 2.5 °C/min. Besides, some pure PCBM samples were quenched to 103 °C and kept isothermal for 4 000 min. After physical aging, they were quenched to -50 °C and then heated to 300 °C at 2.5 °C/min to see the glass transition and the enthalpic relaxation peak.

3.4. DSC results

First the pure blend components P3HT and PCBM will be discussed, with their crystallization behaviour, melting behaviour and glass transition, followed by the blends.

3.4.1. Pristine P3HT

3.4.1.1. Crystallization and melting behaviour

P3HT from the bottle as well as dropcasted P3HT was investigated, showing similar thermograms. Hence, the results obtained from the dropcasted P3HT are discussed.

In Figure 3.4, the second heating and subsequent cooling curve is shown of pristine P3HT. The second heating curve of pristine P3HT exhibits an endothermic peak at 209°C, significantly higher than the 178°C found by Zhao *et al.*[10] and the 170°C-190°C found by Shimomura *et al.*[8], with a high melting enthalpy of 15.2 J/g. This melting peak exhibits a shoulder around 220°C, probably originating from the presence of different crystal structures. In the first heating curve no cold crystallization was observed. Upon cooling a single exothermic peak is observed at 179°C, exhibiting also a shoulder, being consistent with literature.[9] The crystallization enthalpy compares well with the melting enthalpy.

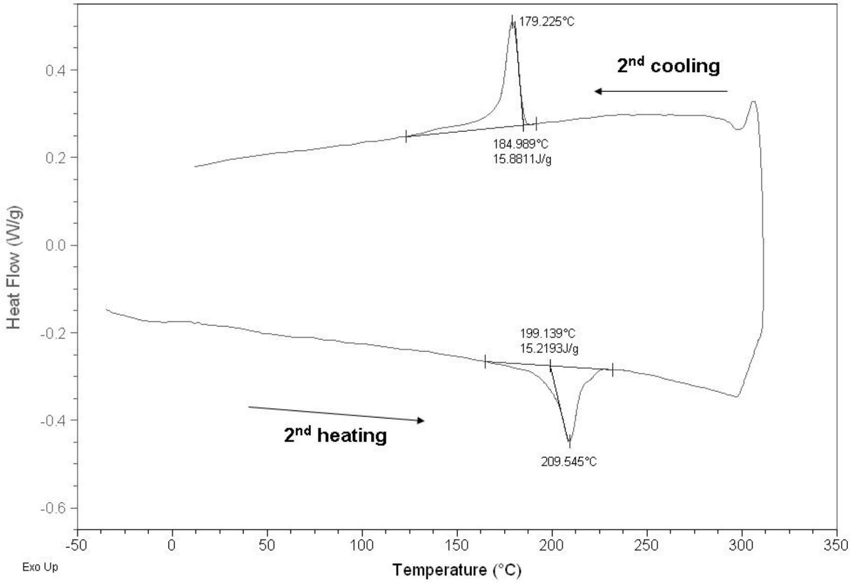

Figure 3.4: DSC thermogram of pristine dropcasted P3HT with heating/cooling rate of 10°C/min. The second heating and cooling cycle is imaged.

3.4.1.2. Glass transition

Starting measurements at –80°C, much lower than the T_g found in literature (i.e. 12°C),[10] should have enabled the T_g determination of P3HT. However, it is generally know that the T_g determination is not straightforward for conjugated polymers. Furthermore, the semi-crystalline nature of P3HT implies a difficult determination of the T_g, because only a fraction of the material is amorphous and because the increase in molecular motion in the amorphous regions at the T_g is hampered by the crystalline regions. Two methods were tried to obtain amorphous P3HT. First, heating the samples above their melting temperatures and subsequently quenching in liquid nitrogen caused condensation of water in the pan. Thus, a large melting peak around 0°C appeared. Secondly, quenching to room temperature did not result in a better determination of T_g with traditional DSC. P3HT crystallizes too fast. Finally, MTDSC was performed on quenched P3HT. Still, it was quite difficult to get an idea of the T_g due to its high crystallinity even for the quenched sample. Obviously, the quench rate is not high enough. Besides, room temperature is above the T_g and causes some crystallization during the storage of the quenched sample. The reverse c_p was plotted, Figure 3.5, as a function of the temperature, revealing a T_g of about 18.7 °C, which is consistent with literature reports.

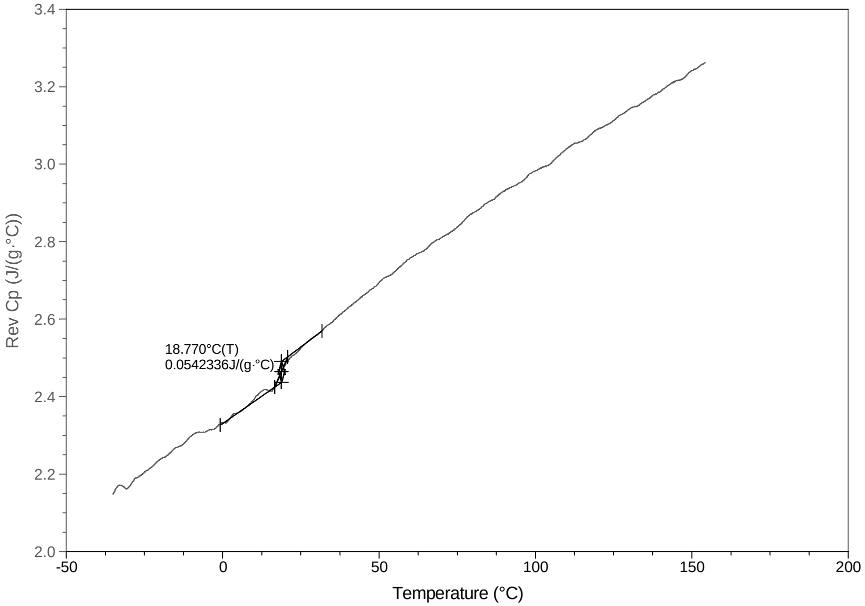

Figure 3.5: : MTDSC of the reversing heat capacity signal of pure P3HT.

3.4.2. Pristine PCBM

3.4.2.1. Melting and crystallization behaviour

For PCBM, thermograms obtained of the dropcasted PCBM samples showed distinct differences with the ones obtained from the powder directly from the bottle. First, the dropcasted samples will be discussed.

The first heating curve (not shown), exhibits a cold crystallization peak around 193°C originating from the meta-stabile condition of dropcasted PCBM. A single melting peak is occurring at 284°C (with an area of 18.5 J/g) with a shoulder at 282°C and a higher one at 288°C, probably attributed to different crystal structures. A very small (0.18 J/g) perturbation at 264°C, perhaps a melting peak, is preceding the melting peak of 284°C. A crystallization peak during cooling was observed around 231°C, with an area of 12.9 J/g. In Figure 3.6, the second heating curve of pure PCBM revealed two endothermic peaks, a small one at 266°C and a larger one at 287°C, with a melting enthalpy of 1.9 J/g and 12.9 J/g, respectively. These areas are comparable with the area of the crystallization peak and much smaller than the melting enthalpy of the melting peak in the first heating curve. The crystals of the first heating curve had more time to be formed during dropcasting, compared to the ones from the second heating curve, formed during DSC measurement, explaining the difference in melting enthalpy between first and second heating curve. Similar results were also evidenced by Warman *et al.*, although no clear explanation was given for the presence of two melting peaks and a single crystallization peak.[11]

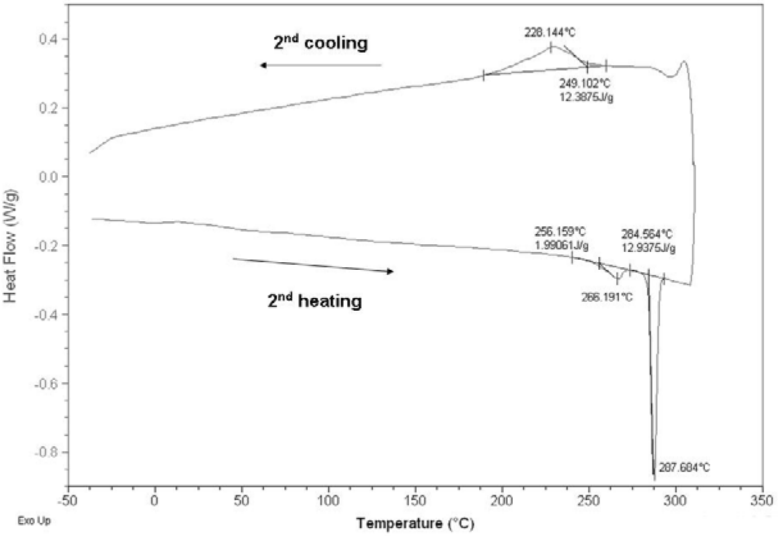

Figure 3.6: DSC thermogram of dropcasted PCBM with heating/cooling rate of 10°C/min. The second heating and cooling cycle is imaged.

It can be stated that the small perturbation in the first heating curve increases significantly in area and that the shoulders present in the second melting peak disappear. No cold crystallization was observed during the second heating, so all material was crystallized during cooling. The presence of two melting peaks can originate from two crystalline forms which are evidenced in powder form. Ripens *et al.* evidenced two different crystal forms (monoclinic or triclinic) of PCBM crystallized out of respectively chlorobenzene or orthodichlorobenzene.[12] In order to check these presumptions, XRD and EBSD measurements were performed on the dropcasted sample, but this did not result in a clear answer. Additionally, the large melting peak, at 288°C in first heating, decreased significantly in area and shifted to a lower value in the second heating.

3.4.2.2. Glass transition

On the dropcasted and PCBM from the bottle, MTDSC was performed in order to get an idea of a T_g. It is worth noting that the glass transition for a polymer can be seen as an increase in the cooperative mobility involving 30-50 segments of the chain. For the PCBM molecules, the glass transition could correspond to the gaining of cooperative movement of several molecules. Since, it was difficult to determine the Tg from the derivative of the heat capacity signal, the Tg will be determined from the c_P signal, as displayed in Figure 3.7 (left). A clear glass transition can be seen around 130°C. A similar result was obtained with the PCBM from the bottle. To confirm that the step change in the reverse c_P is due to a glass transition, a further experimental evidence is shown in Figure 3.7 (right). The first heating, after physical ageing at 103 °C for 4 000 min of quenched pure PCBM, is displayed. The difference in thermal history with dropcasted PCBM is erased because it was molten and subsequently quenched. It can be seen that for the quenched pure PCBM after physical aging, there was an endothermic enthalpic relaxation peak appearing in both MTDSC total HF and non-reversing HF (at about 129.1 °C with an area of about 1.6 J/g) plots. This enthalpic relaxation during annealing below the T_g is a unique phenomenon of amorphous phases due to its non-equilibrium thermodynamic state.[13] Therefore, the properties of amorphous phase can be studied by observing its enthalpic relaxation behaviour.[14] From Figure 3.7 (right), a well-defined glass transition at about 130.8 °C can be seen in the reverse c_P traces, which is consistent with the result shown in Figure 3.7 (left). This is an indicative feature that the step in the reverse c_P signal of pure PCBM shown in Figure 3.7 (left) is a glass transition without any doubt.

The exothermic peak in the non-reversing heat flow at about 159.0 °C with an area of about 4.8 J/g and in the total HF trace are the cold crystallization. In the reverse signal, in Figure 3.7 (left), this transition is evidenced as a drop due to the lower c_P of the crystals formed. The big endothermic peak at around 287 °C in all three signals (HF, non-reversing HF and reversing c_P) is the melting of PCBM.

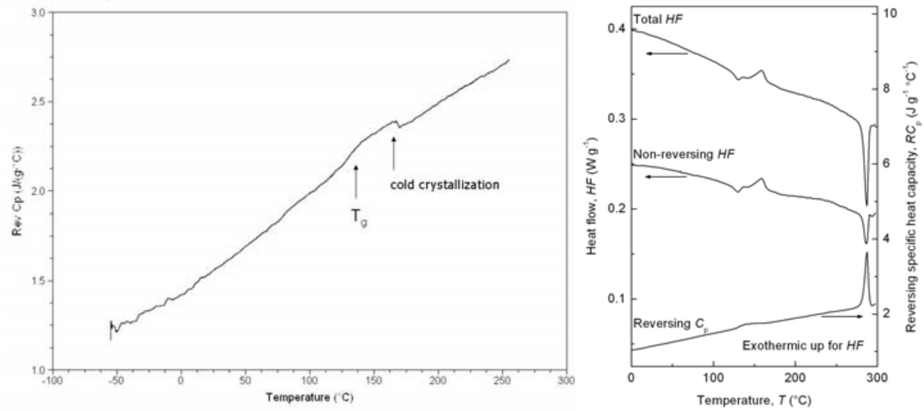

Figure 3.7: MTDSC (left) c_p signal of quenched dropcasted PCBM and (right) HF, non-reversing HF and c_p signals of quenched pure PCBM after physical aging at 103 °C for 4 000 min. HF curves are shifted vertically for clarity.

3.4.3. Dropcasted and pristine PCBM

In Figure 3.8, the first heating and cooling curve of dropcasted PCBM is compared to the pristine PCBM (or PCBM straight from the bottle).

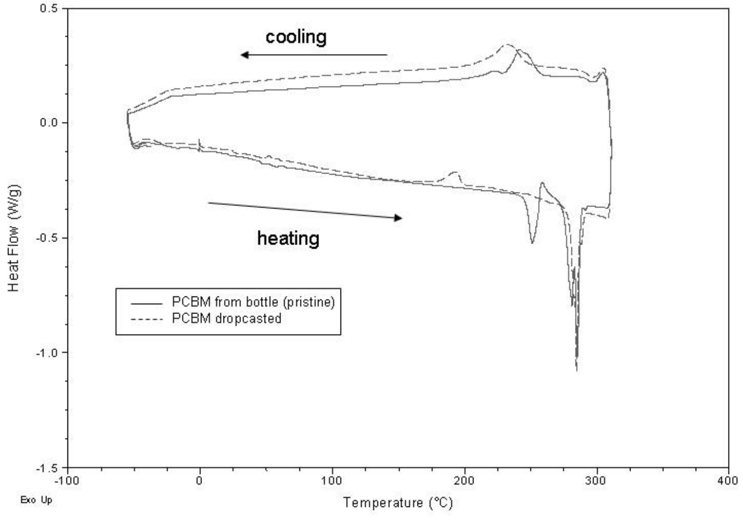

Figure 3.8: Comparison of first heating and cooling curve of PCBM from bottle (pristine) and dropcasted PCBM.

Pristine PCBM is in its crystalline state, so no cold crystallization could be evidenced, in contrast to dropcasted PCBM. In the melting behavior a significant dissimilarity is seen. The pristine PCBM shows a first endothermic peak at 251°C (with an area of around 8 J/g), which is absent in the dropcasted version. It is followed by a exothermic peak at 258°C. The crystals that are melted in the first peak are probably reorganizing and can melt again in the second large (24.3 J/g) double melting peak. In comparison to the peak at 285°C, the main peak for the dropcasted PCBM, the peak at 281°C is larger for the pristine PCBM. The shoulder in the dropcasted PCBM at 288°C is hardly visible in pristine PCBM. During cooling, a crystallization peak at 241°C with a shoulder followed by a smaller one at 221°C is shown in pristine PCBM. The single peak for dropcasted PCBM can possibly be a superposition of two peaks, because upon heating two melting peaks are observed. In the second heating, no significant differences were encountered, while the second cooling again showed two crystallization peaks for the pristine PCBM compared to one for the dropcasted. It is clear that the dropcasting procedure has a lasting influence on the PCBM crystallization. The formation of complexes with the solvent was thought to be at the origin of the formation of different crystal forms after crystallization from different solvents. Why an effect of the solvent is still present after solvent removal and repeated heating and cooling cycles is unclear.

3.4.4. P3HT:PCBM blends

3.4.4.1. Crystallization and melting behaviour

Figure 3.9 displays the first cooling curve of the P3HT:PCBM blends from 0% up to 100% PCBM contents. As discussed in paragraph 3.4.1, the first cooling run for pure P3HT showed an exothermic peak of melt crystallization at about 179 °C with an area of 15.6 J/g. Adding PCBM to P3HT influences not only the position but also the width of the crystallization peak. The onset of the exothermic peak shifts to lower values by adding PCBM, meaning that adding PCBM impedes the crystallization of the P3HT component and less perfect crystals are formed. For the blend with 40 wt% PCBM, the melt crystallization appeared at about 128.5 °C with an area of about 6.4 J/g (or 10.6 J/g polymer). Although for the blend with 50.0 wt% PCBM, a very broad melt crystallization peak at about 112.1 °C with an area of about 2.3 J/g (or 4.6 J/g polymer) was still visible, no melt crystallization of P3HT could be seen for the blends from 60 wt% up to 80 wt% PCBM. This could be said to be in contradiction with the XRD results shown in chapter 2. It was observed that for 66 wt% PCBM and 80 wt% PCBM blends, P3HT does crystallize with increased temperature treatment. In order to clarify this issue, measurements with a heating rate of 20°C/min were also performed, which revealed two melt crystallization peaks for 60 wt% PCBM blends up to 80 wt% PCBM blends, indicating that in both blends P3HT can in fact crystallize. It was confirmed by Zhao *et al.* that with decreasing cooling rate the melt crystallization peak of pure P3HT shifts to higher temperatures and becomes broad, making it more difficult to observe the transition.[10] At a cooling rate of 1°C/min, the melt crystallization peak of P3HT could not be observed, and P3HT crystallized very slowly over a large temperature range. This behaviour is noted to be very unusual, because normally the broadening of the exothermic peak occurs with increasing cooling rate. When the PCBM concentration increased to 90 wt%, there is a new broad melt crystallization of the PCBM component appearing at about 205 °C, with an area of about 6.0 J/g. With a further increase of PCBM concentration, the onset of this peak shifts to higher temperatures, coupled with an increasing area and a sharpening of the peak. Hence, P3HT in his turn impedes the crystallization of PCBM. For pure PCBM, the melt crystallization peak appeared at about 231 °C with an area of about 14.8 J/g.

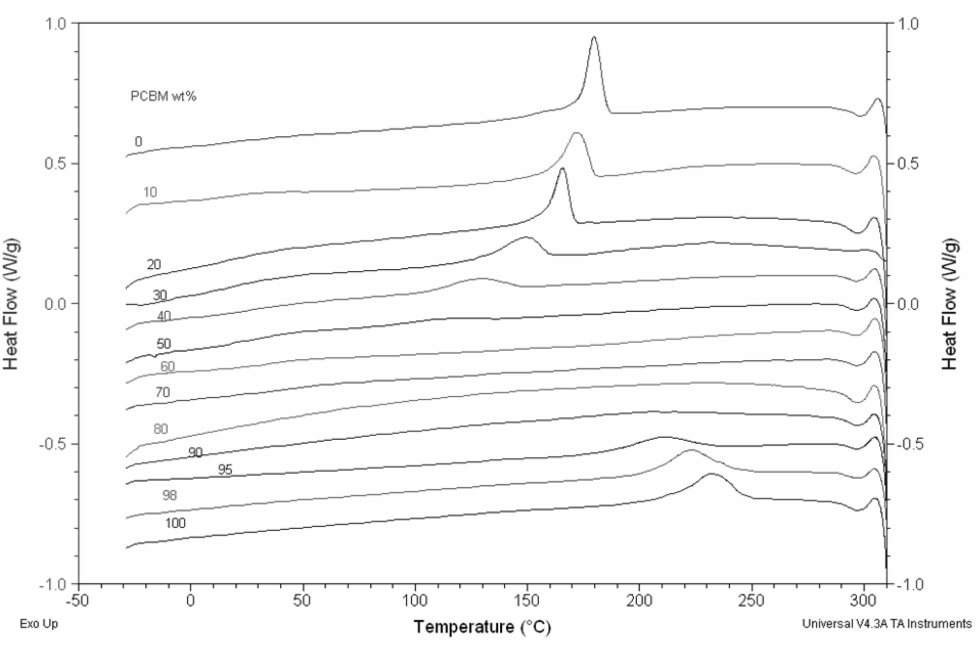

Figure 3.9: DSC thermogram of dropcasted P3HT:PCBM blends with cooling rate of 10°C/min. The first cooling curve is displayed. The wt% of PCBM in the blend is given on the left above the respective graph. The curves are shifted vertically for clarity. All curves are originally located at a heat flow of around 0.5 W/g.

From Figure 3.10, it can be seen that in the second heating run, a melting peak appeared at about 209 °C followed by an upper shoulder at about 220 °C for pure P3HT, as described in section 3.4.1.1. The total peak area was about 16.7 J/g. With the addition of PCBM, the melting peak of P3HT in the blends becomes broader and shifts to lower temperatures, indicating less perfect crystals were formed during the melt crystallization. The shoulder, present in the pure P3HT, becomes more pronounced with addition of PCBM. For the blend with 20 wt% PCBM, the melting peak consists of a larger peak at 197°C and a smaller one at 209 °C, with a total area of about 11.2 J/g (or 14 J/g polymer). When the PCBM concentration increased to 60 wt%, the double melting peaks had shifted to about 170°C and 187°C respectively, with a total area of 5 J/g (or 12.5 J/g polymer). For this blend, the double peaks of P3HT were quite broad, but still visible. Additionally, a broad double melting peak originating from the PCBM component becomes visible at about 263°C and 277°C, with an enthalpy of 1.1 J/g (or 1.84 J/g PCBM), indicating that for a 60 wt% blend both components can crystallize. With a further increase of PCBM concentration, the double melting peaks of P3HT disappear, while those of PCBM become more pronounced: they increase in area and become more sharp. It can hereby be concluded that the crystallization of P3HT is hampered with increased PCBM contents and visa versa, which is in good correspondence with XRD results presented in chapter 2. The 60 wt% PCBM blend is the most amorphous. It is remarkable that a cold crystallization peak of PCBM appears for blends with 80 wt% and 90 wt% PCBM only. The former blend did not show any melt crystallization in the previous cooling run, see Figure 3.9. The latter one only showed a very broad melt crystallization around 204°C.

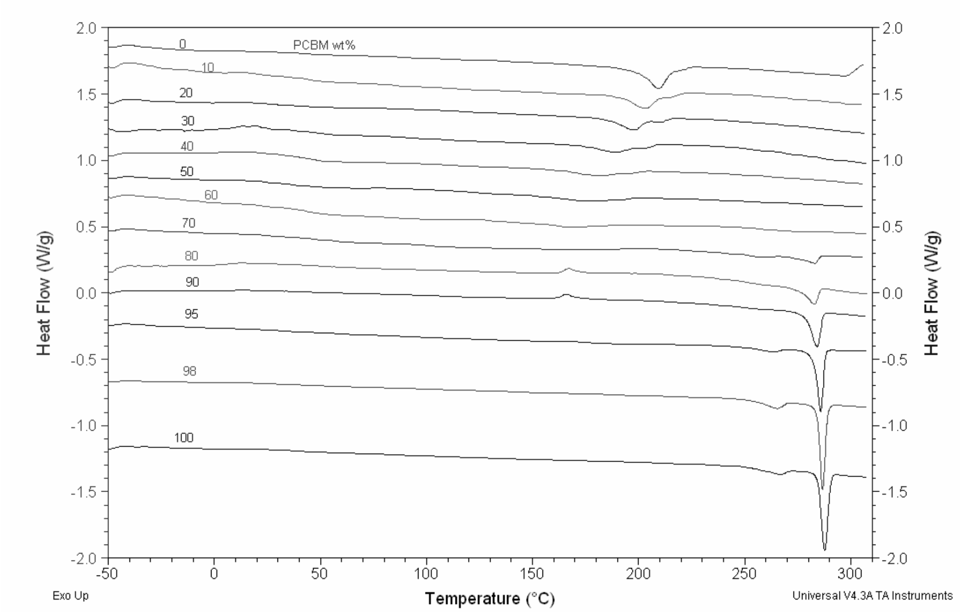

Figure 3.10: DSC thermogram of dropcasted P3HT:PCBM blends with heating rate of 10°C/min. The second heating curve is displayed. The wt% of PCBM in the blend is displayed on the left above the respective graph. The curves are shifted vertically for clarity. All curves are originally located at a heat flow of around -0.5 W/g.

3.4.4.2. Glass transition

The glass transition of all blends was measured by MTDSC. Since crystallization hinders a correct T_g determination, as already indicated in 3.4.1.2 for the T_g determination of pure P3HT, all blends were first brought in the molten state followed by rapid quenching in an attempt to obtain a (largely) amorphous material. Figure 3.11 shows the MTDSC reversing heat capacity (c_p) signal and its temperature derivative (dc_p/dT) of quenched P3HT/PCBM blends with various compositions. In the c_p signal, the T_g is seen as a gradual transition while in the derivative signal the T_g can be found as the maximum of the signal, indicated by an open star on the graphs. Depending on the concentration of blends, and thus also the quality of signal obtained, one or both methods were used to get an idea of the T_g. In the 19 wt% PCBM blend a spike is present, indicated by the arrow in Figure 3.11 (b), which is probably originating from the machine so the maximum can be found as the maximum of the red curve. A single glass transition is observed for all the samples and it shifted to higher temperatures with an increase of PCBM content. The T_g's of pure P3HT and PCBM, were determined in section 3.4.1.2 and section 3.4.2.2 as 18.7°C and 131.2°C, respectively. For the blends with a high PCBM concentration, e.g. 94.8 wt%, and pure PCBM, a drop in c_p followed the glass transition. This drop is attributed to the cold crystallization and is observed as an exothermic peak in the total HF traces, as seen in Figure 3.7 (right).

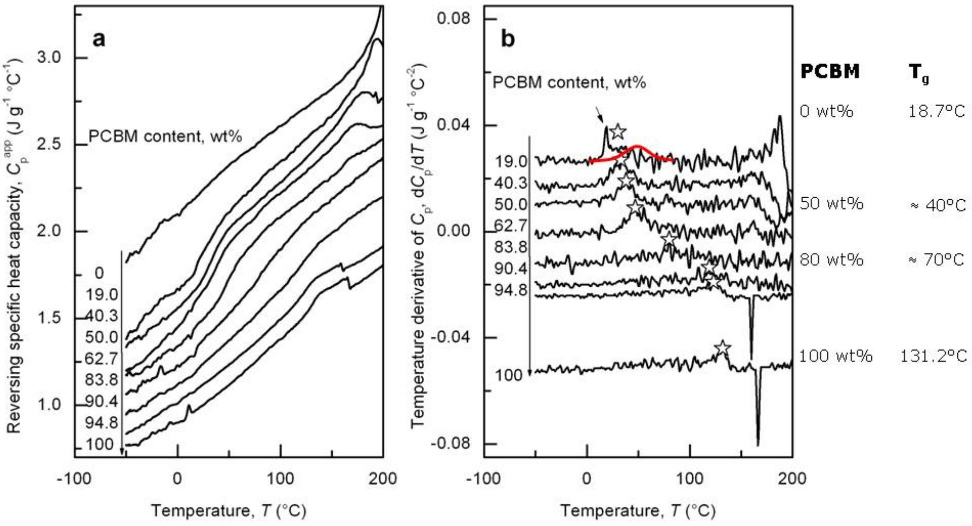

Figure 3.11: (a) MTDSC c_P and (b) its temperature derivative, dc_p/dT of quenched P3HT:PCBM blends. The open stars in part b indicate the T_g. The wt% of PCBM in the blend is displayed on the left above the respective graph. The curves are shifted vertically for clarity.

3.5. Conclusion: state diagram

From the results obtained in section 3.4.4.1 and section 3.4.4.2, a state diagram could be composed. First the crystallization behaviour and melting behaviour is discussed, followed by the glass transition behaviour.

From the results obtained in section 3.4.4.1, a 2D state diagram could be obtained, as displayed in Figure 3.12. It is clearly seen that with increased PCBM content, the melt crystallization temperature and the melting temperature of P3HT shifts to lower values, the former decreasing more quickly. In addition, when the amount of P3HT added to PCBM is increased, the melt crystallization temperature of PCBM lowers significantly, in contrast to the melting temperature, which decreased much less. It was thus demonstrated that with increased PCBM content the crystallization of P3HT is hampered and visa versa, which is consistent with our findings in chapter 2. The most amorphous blend is thus obtained with a 60% weight concentration of PCBM. In addition, phase separation in the melt state was not observed.

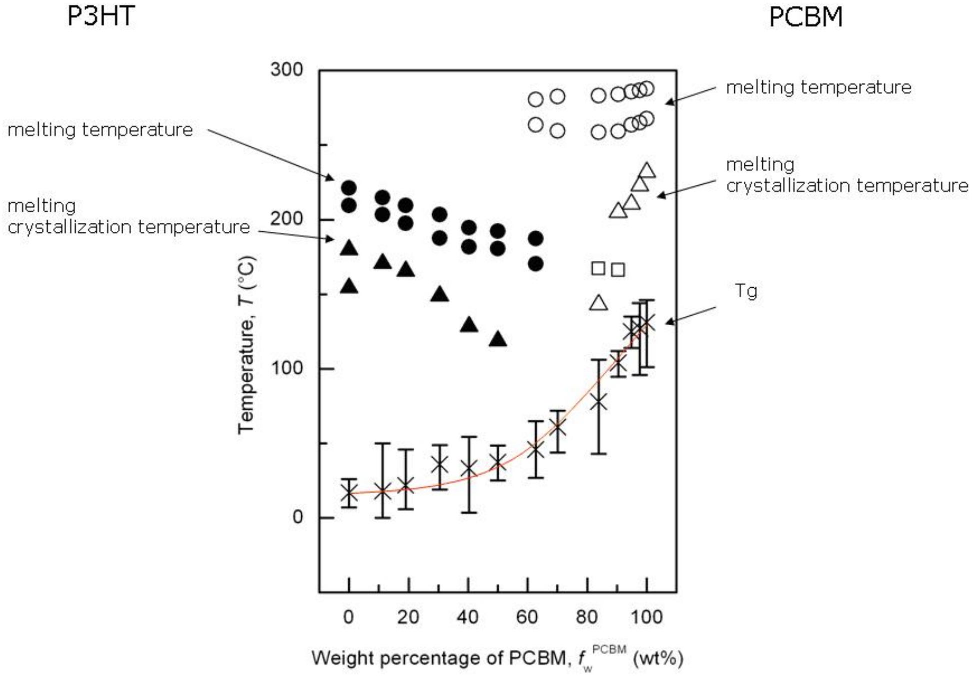

Figure 3.12: State diagram of P3HT:PCBM blends: melt crystallization temperature (▲) and melting temperature (●) of P3HT; melt crystallization temperature (Δ), cold crystallization temperature (□), and melting temperature (○) of PCBM. Glass transition (x), determined at half height, of P3HT:PCBM system as a function of PCBM concentration. The vertical bars indicate the onset and the end of the glasstransition.

Figure 3.12 shows also the trend of the glass transitions for blends with different weight percentages of PCBM. The bars indicate the onset and end of the glass transition. The squares are the T_g determined at half height. It is clearly seen that with increased PCBM contents the T_g shifts to higher temperatures. The most important observation is the fact that the T_g of the blends shifts continuously from the T_g of P3HT till the T_g of PCBM, indicating the existence of a homogenous phase for all blend compositions down to a scale of 10 nm.[15,16] Thus, only phase separation induced by the crystallization of either P3HT or

PCBM could be found, no “intrinsic” liquid-liquid phase separation is observed. Moreover, the end of the glass transition of the amorphous phase will be an important parameter as it defines the lower limit of the temperature window for annealing (increasing the cristallinity or changing the morphology). It is worth noting that at 80°C, a possible operating temperature of solar cells for outdoor applications, only amorphous phases containing 90 wt% PCBM or more are in the 'stable' glassy state, and even for these compositions, physical ageing could occur. For an optimum performance and stability, it would be best if the desired structure could be obtained at a temperature above the maximum operating temperature (e.g. 80°C) and that the material would be fully glassy at the maximum operating temperature. In other words, the use of a conducting polymer with a higher T_g (100°C or more) might be desirable.

3.6. References

[1] H. Hoppe, N. S. Sariciftci, *J. Mater. Chem.*, **16**, 2006, 45.

[2] R. Pieters, “Kinetics of phase transformations in polymer blends by means of Modulated Temperature DSC“, PhD thesis, oct 2005, VUB.

[3] G. van der plaats, “The practice of thermal analysis”, Mettler.

[4] E. Pungor, “A Practical Guide to Instrumental Analysis”, Boca Raton, 1995, 181–191.

[5] B. Wunderlich, Y. Jin, A. Boller, *Thermochimica acta*, **238**, 1994, 277.

[6] M. Reading, A. Luget, R. Wilson, *Thermochimica acta*, **238**, 1994, 295.

[7] N. A. Bailey, J. N. Hay, D. M. Price, *Thermochimica acta*, **267**, 2001, 425.

[8] M. Shimomura, M. Kaga, N. Nakayama, S. Miyauchi, *Synthetic metals*, **69**, 1995, 313.

[9] A. Zen, M. Saphiannikova, D. Neher, J. Grenzer, S. Grigorian, U. Pietsch, U. Asawapirom, S. Janietz, U. Scherf, I. Lieberwirth, G. Wegner, *Macromolecules,* 2006, **39**, 2162.

[10] Y. Zhao, G. Yuan, P. Roche, M. Leclerc, *Polymer*, **36**, 1995, 2211.

[11] J. M. Warman, M. P. de HAAS, T. D. Anthopoulos, D. M. de Leeuw, *Adv. Mat.* , **18**, 2006, 2294.

[12] M. T. Rispens, A. Meetsma, R. Rittberger, C. J. Brabec, N. S. Sariciftci, J. C. Hummelen, *Chem. Commun.,* **17**, 2003, 2116.

[13] J. M. Hutchinson, *Prog. Polym. Sci.,* **20**, 1995, 703.

[14] J. Zhao, J. Wang, C. Li, Q. Fan, *Macromolecules,* **35**, 2002, 3097.

[15] W. J. MacKnight, F. E. Karasz, “Comprehensive Polymer Science: The Synthesis, Characterization, Reactions & Applications of Polymers”, Volume 1, Chapter 4, Eds. Sir Allen G FRS, Bevington JC, Pergamon Press, New York, 1989.

[16] D. S. Kaplan, *J. of Appl. Polym. Sci.*, **20**, 1976, 2615.

4. Local electrical properties

Previous chapters covered the morphological characterization of the P3HT:PCBM blends. As this kind of blends is one of the most promising and widely used in bulk heterojunction solar cells, it is of great importance to be able to further correlate the morphology and the electrical properties of the system. Until now, the relationship between morphology and electrical properties is insufficiently known. Scanning probe microscopy (SPM) offers several methods to map simultaneously morphology and local electrical properties with a high spatial resolution. These methods have been first developed to face specific issues in conventional semiconductor nanotechnology. Scanning spreading resistance microscopy (SSRM)[1] and scanning capacitance microscopy (SCM)[2] provided major contribution for high resolution carrier profiling in the last generations of Si and III-V based electronic and optoelectronic materials and devices.[3-5] Conductive AFM (C-AFM)[6] exhibited significant contribution in the characterization of pin-holes in high-k dielectrics, while Kelvin probe force microscopy (KPFM)[7] demonstrated its usefulness in the characterization of III-V laser diodes and chalcopyrite solar cells and ferroelectrics based structures.[8-11] Interestingly upon the last few years, growing interest has been shown towards the use of these methods for the characterization of plastic electronics materials and devices, such as bulk heterojunction solar cells.

In this work, electrostatic Force Microscopy (EFM) extended with additional sample internal biasing has been applied to probe the local lateral conducting properties of the current-carrying surface of reference blends, typically made of MDMO-PPV:PCBM and P3HT:PCBM mixtures. A MDMO-PPV:PCBM blend has been characterized to get a clear insight of the conductive properties of PCBM and to analyze the donor-acceptor interface in phase separated systems.[12] Conductive atomic force microscopy (C-AFM) has also been applied to perform two dimensional current mapping of sample conductivity of P3HT:PCBM and MDMO-PPV:PCBM blends. Local spectroscopy (I-V profile) has been used to analyze transversal charge transport mechanisms in pure P3HT films. Finally, the sensitivity of C-AFM to photocurrent has been explored.

In this chapter, the working principles and the detection systems of these three methods will be thoroughly described. The most significant results obtained on the samples of blends will be presented and discussed. Finally, the methods will be compared pointing out the current experimental and physical limitations.

4.1. EFM

4.1.1. Definition of technique

The non-contact operating mode of electrostatic force microscopy (EFM) makes this method an ideal candidate to probe soft conjugated polymers and blends.[13-16]

EFM can measure simultaneously the topography of the sample and the electrostatic interactions originating from the surface potential difference between the conductive tip and the sample surface, thus leading to a 2D electrical mapping of sample surface properties. First, the principle of contact potential difference will be explained in order to facilitate the understanding of the physical principles of standard EFM (4.1.1.2).

4.1.1.1. Principle of contact potential difference measurement

The determination of the contact potential difference (CPD) between two conductive materials can be performed by means of the Kelvin probe method. The basic principles of this method is illustrated in Figure 4.1.

Two separated materials are electrically neutral. When these two materials, with different work functions[1], come in close vicinity of each other, electrons will flow from the material with the lower work function to the one with the higher work function, until their Fermi-levels[2] are aligned.[17] This results in the appearance of an electric field at the interface. Hence, a potential variation is observed at the vacuum level. This variation of potential must be equal to the difference of work function between the two metals and is called contact potential difference.[18] The application of a voltage between the two materials will shift the Fermi-levels apart again.

---

[1] The work function of a material is the minimal energy needed to remove an electron from the ground state in a given material

[2] The Fermi Level is defined as the highest occupied molecular orbital (HOMO, see chapter 1) in the valence band at 0 K

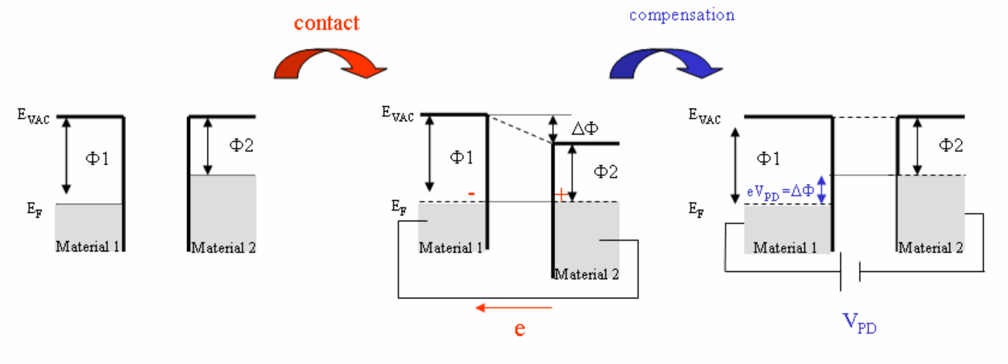

Figure 4.1: The principle for measuring the CPD of two metals. Φ_1: work function of the first material, Φ_2: work function of the second material, Ef: Fermi-level, E_{vac}: vacuum level, V_{PD}: contact potential difference.[18]

This is a well known effect used in standard Kelvin probe force microscopy (KPFM) detection system to determine the contact potential difference between two materials. Replacing one of the two materials by a conductive tip probe, it is therefore possible to perform local mapping of the sample surface potential. The application of an external voltage, contact potential difference (V_{PD}), between the two materials to nullify the field should therefore be equal to the difference of work function, given by equation 4-1.

$$V_{PD} = \frac{\Delta\Phi}{q} = \frac{\left(\Phi_{sample} - \Phi_{tip}\right)}{q} \qquad \textit{equation 4-1}$$

with q the magnitude of the elementary charge (no unit), Φ_{sample} and Φ_{tip} the work function of the sample and tip respectively.[19]

4.1.1.2. Physical principles of standard EFM

In standard EFM, a combined voltage bias signal, consisting of a alternating current (ac) and direct current (dc), is applied between the tip and sample. The resulting total voltage between tip and sample V(t) given by:

$$V(t) = V_{dc} + V_{PD} + V_{ac}\sin(\Omega t) \qquad \textit{equation 4-2}$$

with V_{dc} the dc offset voltage, V_{PD} the contact potential difference between tip and sample, V_{ac} and Ω are respectively the amplitude and frequency of the applied ac voltage signal.[20]

Applying a V_{ac} results in an electrostatic field, causing an oscillation of the cantilever with the frequency Ω. The tip-sample system can be seen as a simple capacitor. Hence, the electrostatic force F, as a result of the electrostatic field E, between tip and sample can be expressed by following equation:

$$F = -\frac{1}{2}\frac{\partial C}{\partial z} \times V^2 \qquad \textit{equation 4-3}$$

where V the applied voltage, C the tip-sample capacitance and z the direction normal to the sample surface. The capacitance depends on the distance between the tip and the sample and on the geometry of the system and specially the probe. Since V is the sum of the contact potential difference, the ac (V_{ac}) and dc (V_{dc}) voltages (see equation 4-2), equation 4-3 becomes:

$$F = -\frac{1}{2}\frac{\delta C}{\delta z}\left[V_{PD} + V_{dc} + V_{ac}\sin \Omega t\right]^2 \qquad \textit{equation 4-4}$$

Combining now equation 4-1 and 4-4 results in:

$$F(t) = \underbrace{\boxed{-\frac{\delta C}{\delta z} \times \left[\frac{1}{2}\left(V_{dc} - \frac{\Delta\Phi}{q}\right)^2 + \frac{V_{ac}^2}{4}\right]}}_{A} \underbrace{\boxed{-\frac{\delta C}{\delta z} \times \left(V_{dc} - \frac{\Delta\Phi}{q}\right) \times V_{ac}\sin \Omega t}}_{B} \underbrace{\boxed{+\frac{\delta C}{\delta z}\frac{V_{ac}^2}{4}\cos(2\Omega t)}}_{C} \qquad \textit{equation 4-5}$$

In the above equation three terms are present: the dc term (=A), corresponding to the static deflection of the cantilever, the first harmonic or Ω term (=B) and the second harmonic or 2Ω term (=C). The three terms can be independently recorded by means of lock-in based detection system. The dc term is positive and corresponds to the deflection of the cantilever. The term C is positive and can be used to determine the effective capacity between the tip and the sample. Since term A and C both are positive and depend on V_{ac} , a low ac amplitude is usually required to minimize the electrostatic contribution to the topographical signal. The B term is directly proportional to $(V_{dc} - \frac{\Delta\Phi}{q})$, and can therefore nullified by applying an appropriate dc bias.

Depending on the type of system used, EFM can operate using two techniques, i.e. two pass or one pass technique. In the two pass technique, the sample is scanned twice recording subsequently the topography and the electrostatic force. Upon the first scan only the topography is recorded. This serves to operate at fixed tip-sample distance, i.e. to obstruct the topographical contribution from the electrostatic signal. The corresponding detection system is based on a simple lock-in detection method operating at one given frequency, typically the resonance frequency of the cantilever for sake of maximum sensitivity. In the one pass technique, topography and electrical signals are recorded simultaneously operating at two different frequencies, by means of two independent lock-in detection systems. In this thesis all EFM measurements were performed using a one pass technique system. To separate the topography signal from the electrostatic force signal, the first resonance frequency of the cantilever ($f_1 = \omega_1/2\pi$) is used to control the tip height. The EFM signal is then measured independently from the topography using another frequency Ω. The typical lateral resolution that can be obtained with EFM is 50 nm using a tip with a radius of 10 nm.[21]

4.1.1.3. Physical principles on lateral EFM

In this work, the standard EFM was adapted to perform lateral electrical measurements. A substrate consisting two Au electrodes is used. One contact is grounded while the other one is biased with V_{dc}, as shown in Figure 4.2. Hence, a voltage distribution V(x,y) is produced, instead of a constant dc between tip and sample in standard EFM. An ac voltage V_{ac} is then applied to a conductive tip. The tip is then scanned across the sample surface, while the variations of the local electrostatic interactions between the current-carrying sample and tip are recorded. The changing first harmonic component (term B in equation 4-5) of the electrostatic force is shown to be proportional to V_{ac} as well as to $\left(V - \frac{\Delta\Phi}{q}\right)$. Here, V is the local dc voltage applied between the tip and the sample. The tip then acts as a local voltmeter. Local changes in this voltage distribution can then be correlated to local conductivity differences. Using this mode of operation of the EFM set-up, it becomes possible to simultaneously map the topography, the voltage distribution V(x,y) over a current-carrying film, as well as the work function distribution of the film, allowing to directly compare morphological structure and local electrical properties.

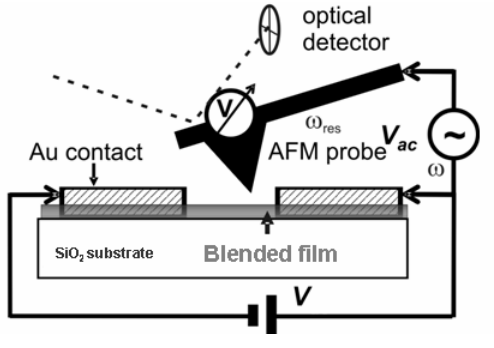

Figure 4.2: AFM based set-up for the lateral EFM measurements on current-carrying MDMO-PPV:PCBM and P3HT:PCBM blended polymer film surfaces.

4.1.2. Experimental set-up

The lateral EFM measurements were performed with a commercial atomic force microscope (AFM) system Autoprobe M5 (Veeco Instruments). The AFM is operated in non-contact mode with the cantilever oscillating near its first resonant frequency ($f_1 = \omega_1/2\pi \sim 90$ kHz) at a fixed height (10 – 40 nm) above the sample. A dc voltage V is applied between the electrodes (Figure 4.2). An ac voltage V_{ac} is applied to the conductive AFM tip, a $PtIr_5$ metal-coated etched Si tips (Ultralever, Veeco Instr.). The first harmonic detection of the electrostatic force is performed at $\Omega \sim 3$ kHz. The applied dc voltage V was in the range of 0 - 10 V, the ac voltage was $V_{ac} = 2$ V. The EFM signal is converted into a potential (in volts) assuming a linear decrease of the potential across the two electrodes (Figure 4.2).

4.1.3. Sample preparation

Two interdigital structures were used. The first one is a Si substrate coated with an Au finger structure with spacing's from 2.5 μm up to 20 μm. MDMO-PPV (Covion):PCBM (Nano-C) 1:4 ratio blends dissolved in toluene and P3HT (Merck, $M_w = 35000$ g/mol and PD = 1.842) blended with PCBM (Nano-C) in a 1:1 ratio dissolved in chlorobenzene were spincoated on top of it. Prior to spincoating, the samples were subsequently rinsed with subsequently soap, demineralised water, acetone and isopropanol. The major drawback of the Au finger structure lies in the large distance between the electrodes. Therefore, in order to create a sufficiently large lateral electric field to enable the effective EFM measurements, two electrodes with a more narrow slit between them had to be fabricated on the sample surface. Using e-beam lithography (EBL) two parallel gold electrodes, separated by a distance of 1 μm, are fabricated on the Si/SiO_2 sample surface. The Si/SiO_2 substrate was cleaned in isopropyl alcohol (IPA) in an ultrasonic bath and was coated with bilayer of polymethyl methacrylate (PMMA)/co-PMMA e-beam resist. The pattern was defined using EBL on the resist layer. Exposed area of electron beam resist was developed with a 1:1 mixture of methylisobutylketone (MIBK) and IPA. Afterwards a Au film with a thickness of 30 nm was sputtered as contact electrodes followed by lift-off process. Finally, MDMO-PPV and P3HT blends were spincoated on top of it. Figure 4.3 shows the optical microscopy image (a) and an AFM image (b) of the sample surface.

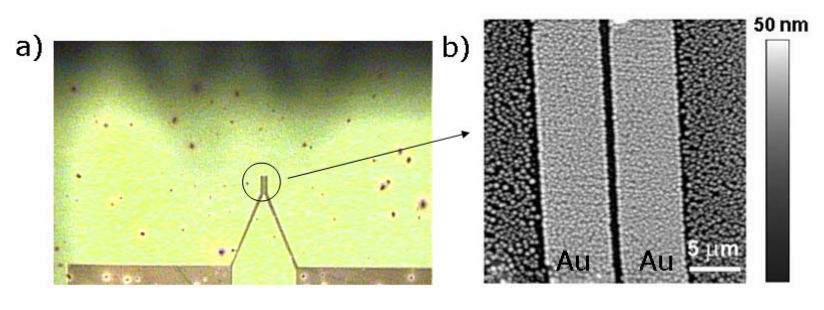

Figure 4.3: (a) 810×520 µm optical image of Au electrodes fabricated by e-beam lithography with interspacing of 1 µm. (b) 25×25 µm² AFM (height) image of a MDMO-PPV:PCBM polymer film spincoated on Si/SiO$_2$ substrate.

4.1.4. Lateral EFM on MDMO-PPV:PCBM blends

Figure 4.4 shows the topography (a) and the high resolution EFM signal (b) simultaneously recorded across a MDMO-PPV:PCBM 1:4 blend. In the topography image (Figure 4.4 (a)), larger phase separated regions (300 nm up to 500 nm) are evidenced on the Au electrodes compared to the region in between of the Au electrodes (around 200 nm). A poor contrast is observed between the contacts probably induced by the large topography differences at the Au electrodes.

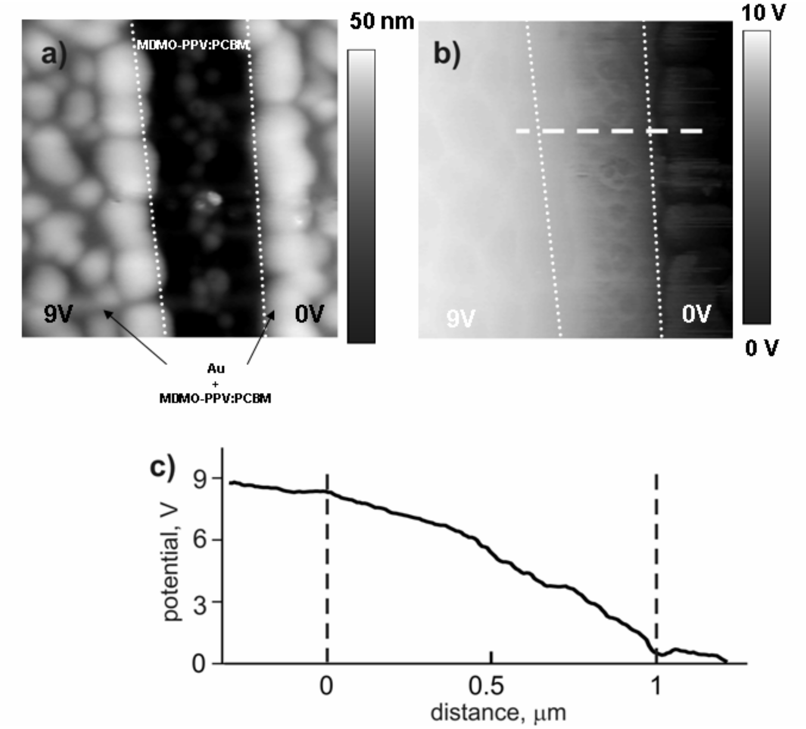

Figure 4.4: (a) 2×2 μm^2 AFM (height) image and (b) corresponding lateral EFM image of the current-carrying MDMO-PPV:PCBM polymer film structure (V = 9 V). (c) Electric potential profile obtained across the dashed line indicated in (b), the two dashed vertical lines indicate the positions of the edges of the electrodes.

The EFM contrast gradient across the scanned area (Figure 4.4 (b)) corresponds to lateral electrical potential drop generated between the two Au electrodes. The lateral potential profile is shown in Figure 4.4 (c). Interestingly, the voltage drops at the electric contacts are small, indicating low injection barrier between the Au electrode and the blended polymer film. The average potential distribution across the blended polymer film between the two Au electrodes is however clearly non-linear, indicating that the layer behaves as a diffusive conductor, with voltage dependant conductivity.

In Figure 4.5 the results of the EFM measurements on the current-carrying MDMO-PPV:PCBM film are presented, to further investigate the variations of the

EFM signal within the blend.

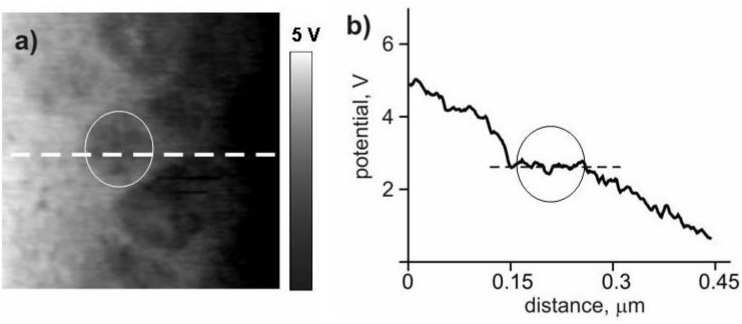

Figure 4.5: (a) 0.45×0.45 μm^2 EFM image of the current-carrying MDMO-PPV:PCBM polymer film surface between the electrodes (V = 9 V). (b) Electric potential profile obtained across the dashed line indicated in (a). The contribution of the PCBM cluster in the surface potential is indicated by a circle in both (a) and (b).

It is noteworthy that the small interelectrode distance (1 μm) allows reliable observation of the drop of potential at a scale comparable with a typical PCBM cluster size (Figure 4.5 (a)). The EFM profile, shown in Figure 4.5 (b), exhibits a constant potential across the whole PCBM cluster region, in clear contrast with the monotonic drop in potential across the surrounding blend. One possible explanation could be that, the drop of potential along the PCBM cluster is very small due to considerably higher conductivity of the cluster.

4.1.5. Lateral EFM on P3HT:PCBM blends

Figure 4.6 shows the topography (a) and the corresponding EFM image (b) of a P3HT:PCBM 1:1 annealed for 30 min at 125°C. It was annealed to create large PCBM needles, described in chapter 2, in order to study the conductive properties of individual PCBM needle-shaped crystals by EFM.

Similarly to the MDMO-PPV:PCBM blends, the average potential drop along the P3HT:PCBM is monotonic and small potential variations are observed at the Au-polymer interface, indicating a low injection barrier between the Au electrodes and the blended polymer interface. Furthermore, the potential drop along the structure is non linear, indicating diffusive conductor properties of the blend, i.e. a structure with a voltage dependant conductivity.

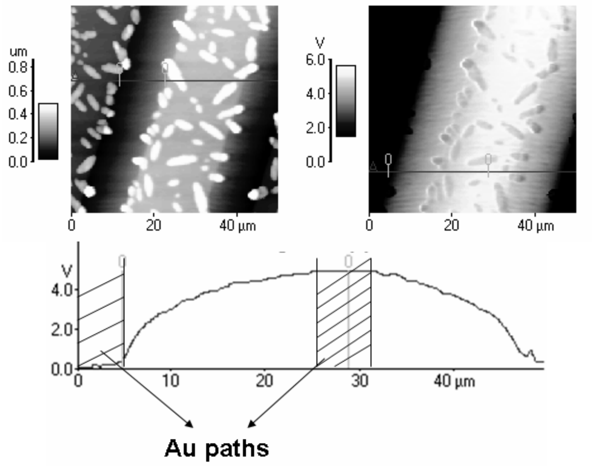

Figure 4.6: (a) 50×50 μm^2 AFM (height) image and (b) corresponding EFM image of the current-carrying P3HT:PCBM 1:1 polymer film structure (V = 5 V). (c) Electric potential profile obtained across the line indicated in (b), the two vertical lines indicate the positions of the edges of the Au electrodes.

In Figure 4.7 a closer look has been taken to the electrical properties across the P3HT:PCBM blend itself away from the large PCBM needles. The height profile and the corresponding EFM image are given in Figure 4.7 (a) and (b), respectively. The electrostatic profile across the horizontal line in Figure 4.7(b) is shown in Figure 4.7(c). Topography variations in the order of 10 nm are observed and voltage variations of 0.2 V. From the EFM image, different contrast is observed from the topography variations indicating that part of the contrast emerges from variations in the electrostatic interaction between the probe and the sample. Possible variations in the surface potential can be attributed to local crystalline P3HT regions. Nevertheless, the homogeneity of the film and the small topographical variations combined with the low surface potential variations recorded hampered further EFM characterization of these P3HT:PCBM blends. C-AFM has therefore naturally applied for its high sensitivity and higher spatial resolution.

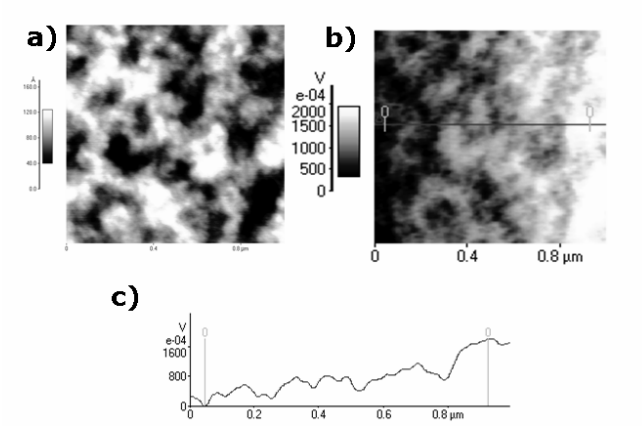

Figure 4.7: (a) 1×1 μm² AFM (height) image and (b) corresponding EFM image of the current-carrying P3HT:PCBM 1:1 annealed polymer film structure (V = 5 V). (c) Electric potential profile obtained across the line indicated in (b).

In addition to the EFM measurements on the annealed P3HT:PCBM blend, attempts were done to evaluate the conductive properties of individual PCBM needle-shaped crystals by EFM. As described in chapter two, these needles are obtained upon a post annealing process of 5 min at 125°C. Unfortunately it was not possible to grow the PCBM crystals in between of the Au contacts to provide their convenient arrangement for the EFM measurements. A preferential growth on Au is favoured because of the higher thermal conductivity of Au compared with SiO_2. Besides, the high (up to 180 nm) topographic variations across a PCBM needle considerably influence on the EFM contrast. This stressed the need for other SPM based electrical characterization methods likely to handle large topographical variations. This further motivated the use of C-AFM to characterize this type of blend.

4.2. Conductive-AFM

4.2.1. Physical principles and detection system with EFM

The variations of the surface potential imaged are only indirectly related to the conductive properties of the blends.[22] The ability of C-AFM to directly map the local conductivity of semiconducting materials with high sensitivity renders it a suitable alternative for further electrical characterization of organic blends. The electrical sensitivity of 100 fA enables the measurement of high resistive materials, such as semi-conductive polymers.[23] In this method, a dc voltage is applied between the probe and the sample and the induced current flowing throughout the film is measured (Figure 4.8). A feedback loop ensures constant deflection of the cantilever, i.e. constant tip-sample contact forces, and yield the topography of the sample surface. The resulting current passing through the sample, is being measured by a low-noise linear current amplifier. Current and topography are therefore simultaneously but independently recorded. In addition to local two dimensional current mapping, I-V profiles can be obtained by holding the tip at a fixed location while sample bias is ramped up and down. Hence, charge transport mechanisms can be characterized and mobility and injection barriers can be determined. In contrary to EFM (lateral probing), C-AFM therefore performs a transversal probing of the conducting properties of the film. The simple physical principles and direct quantitative measurement of conductive properties render, in addition, C-AFM a more accessible technique compared to EFM. Finally, a spatial resolution comparable to the tip radius (20 nm) can be achieved.

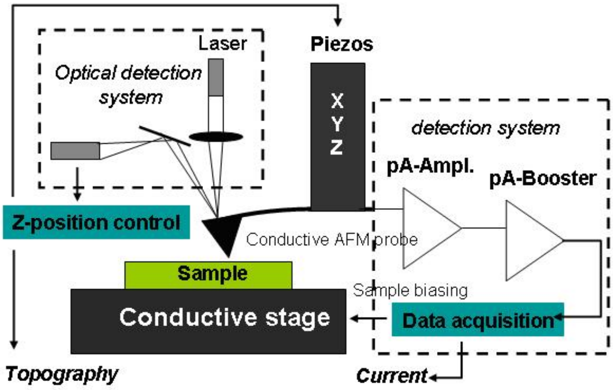

Figure 4.8: Schematic of conductive AFM set-up. In dashed squares the two independent detection systems are depicted, enabling simultaneous characterization of surface topography and current.

4.2.2. Experimental

4.2.2.1. C-AFM samples

MDMO-PPV:PCBM and P3HT:PCBM blended films were dissolved in correspondingly toluene and chlorobenzene and stirred over night at a temperature of 50°C prior to spincoating. The MDMO-PPV (Covion):PCBM (Nano-C) and P3HT (Merck, M_w = 35000 g/mol and PD = 1.842):PCBM (Nano-C) blended films were spincoated on the ITO coated glass substrates (Merck Display Technologies Ltd., R_{sheet} = 47 Ω/□), yielding a thickness of 100 nm as determined by profilometry measurements. Following cleaning procedure of the ITO substrates was performed prior to spincoating:

- mechanical cleaning with soap soaked dust-free clean room wipes

- 30 min in ultrasonic bath in de-ionized H_2O with detergent

- rinsing with de-ionized H_2O

- 10 min in ultrasonic bath with de-ionized H_2O

- rinsing with acetone

- 10 min in ultrasonic bath with acetone

- rinsing with IPA water

- 10 min in boiling IPA

- blow drying with nitrogen flow

- 15 min in an oxygen plasma oven

The oxygen plasma treatment is motivated to burn out all remnant organic traces delivering bare ITO surface. Moreover, the workfunction of ITO is shown to be modified by this treatment from 4.2 up to 4.7 eV, presumably by the incorporation of additional oxygen atoms.[24] Moreover the surface of ITO is more hydrophilic so that water based solutions, like PEDOT:PSS (used in the P3HT devices), can better spread over the ITO layer. The annealing procedures were performed on a hotplate in nitrogen atmosphere.

4.2.2.2. P3HT devices

For the fabrication of the P3HT devices, a 60 nm thick poly(3,4-ethylenedioxythiophene-polystyrenesulfonate (PEDOT:PSS), supplied by Bayer was spincoated on top of the ITO substrate in nitrogen atmosphere. The substrates were dried for 20 min on a hotplate at 120 °C and P3HT (Merck, M_w = 35000 g/mol and PD = 1.842) was then spincoated on top of the PEDOT-PSS layer. The film thickness was shown to be around 100 nm as determined by DEKTAK profilometry. As a last step, an Al top electrode of 80 nm was evaporated on top of the active layer. The IV-characteristics were measured with an Oriel solar simulator in dark conditions.

4.2.2.3. Measurement system

C-AFM measurements were performed in ambient atmosphere using a Multimode (Veeco) microscope equipped with the Nanoscope III controler and extended with the C-AFM/TUNA module. C-AFM allows the measurement of currents in the range of 1 pA to 1 µA, while Tunneling AFM (TUNA) can map ultra-low currents in the range of 100 fA to 100 pA. The electrical tip-sample circuit was completed by means of ITO coated glass substrates (Merck Display Technologies Ltd., R_{sheet} = 47 Ω/□) serving as the electrical back contact. $PtIr_5$ coated etched Si tips attached to a very soft cantilever (spring constant of 0.2 N/m) were chosen to avoid tip induced topographical damage.

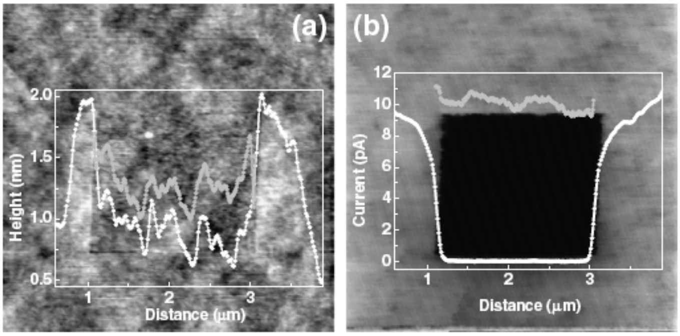

Figure 4.9: (a) 4×4 µm² AFM (height) image and (b) corresponding current image of the P3HT:PCBM 1:1 film not annealed. A dc tip bias of -1V was applied.

Figure 4.9 shows the impact of the scanning on to the topography and the conductivity of the sample. A 2×2 µm² scan (not shown) was preliminary performed with a dc tip bias of -1 V. A second 4×4 µm² scan at the same location was then performed to control the impact of the tip on the 2×2 µm² scan. Very small topographical variations (less then 1 nm) are observed at the border between the freshly scanned regions and the previously scanned regions. Furthermore, no real morphological change is observed between the first (light gray) and second (white) scan within the original 2×2 µm² region, indicating very negligible topographic damage using soft probes. This clearly demonstrates the possibility to use contact mode operating SPM methods for soft structures such as polymers. However, a clear conductivity contrast can be observed in the current image, indicating local electrical damage induced by the probe while performing the preliminary scan. This was expected to originate from local oxidation/reduction of the polymer upon tip bias. This would be interesting for further research. However, this is out of the scope of this thesis and is not desirable for the electrical characterization of blends. Therefore, in following measurements, scans were performed on fresh areas to be clear of electrical damage induced upon scanning.

4.2.3. MDMO-PPV:PCBM blends

Figure 4.10 shows the 2×2 μm² C-AFM topography (a) and current (b) image of a MDMO-PPV:PCBM 1:4 blended film. Low current variations in the order of 1 pA are observed. Similar current contrast is observed between the PCBM-rich regions and the surrounding MDMO-PPV:PCBM blend. From Figure 1.15, it is seen that the PCBM-rich regions are covered by a thin MDMO-PPV rich layer. Therefore, it can be concluded that the current recorded emerges from the conduction of holes in MDMO-PPV across the blend. No current is however observed at the base of the PCBM-rich regions. Interestingly, this contrast is also observed at the centre of the PCBM clusters (see arrows). This suggests that the probe is locally directly in contact with PCBM, i.e. the thin polymer rich layer is only partially covering the cluster or that the tip has locally damaged the thin MDMO-PPV rich layer.[25] The very low current is explained by the large injection barriers at the tip-PCBM contact.[25] Finally, the asymmetry of the dark contrast surrounding the clusters indicates possible tip induced artefacts in the current image. This effect is however small and confirms the high spatial resolution likely to be obtained with C-AFM.

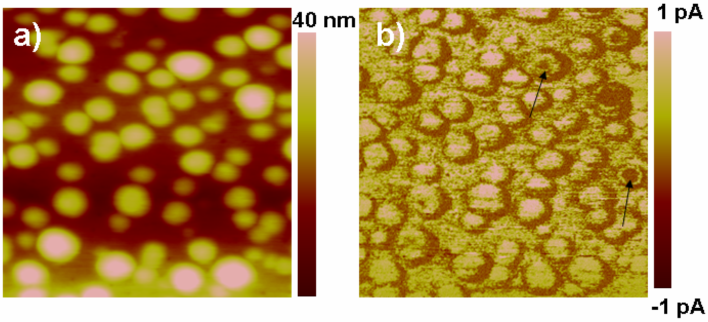

Figure 4.10: (a) 2×2 μm^2 C-AFM topography and (b) current images of the MDMO-PPV:PCBM 1:4 (toluene) blend with a sample bias of 1 V applied.

In addition to these measurements, scans were performed gradually decreasing the sample bias (down to -6.4 V), as shown in Figure 4.11.

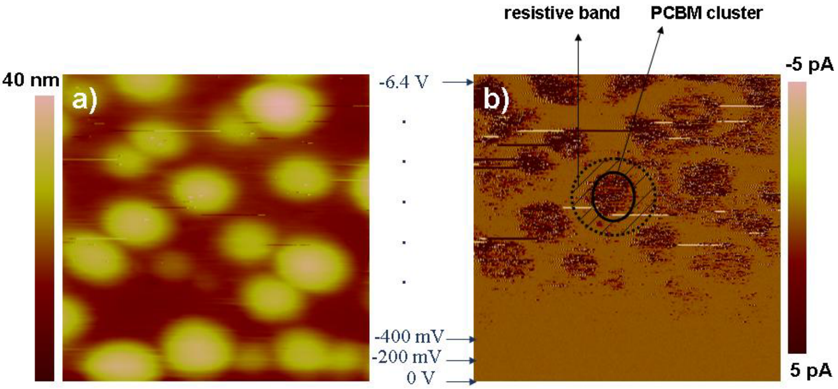

Figure 4.11: (a) 1×1 µm^2 C-AFM topography and (b) current images of the MDMO-PPV:PCBM 1:4 (toluene) blend while gradually decreasing the sample bias from 0 V down to -6.4 V with steps of 200 mV. A PCBM cluster is indicated by a circle while the resistive band surrounding the PCBM cluster corresponds to the arched area.

When no voltage is applied no distinction between the different phases of the blend can be seen. By decreasing the voltage, current starts to be detected around -1 V, indicating significant build-in voltage on both phases of the blend. The current detected coincides with the position of PCBM-rich regions. By furthermore decreasing the voltage, a higher current is flowing trough the PCBM-rich regions. Meanwhile, zero signal is uniformly observed across the surrounding blend. This suggests that locally the current transport is dominated by electrons, which are tunnelling through the thin MDMO-PPV layer into the PCBM-rich region. The non-uniform morphology and thickness of the polymer thin layer, therefore explains the progressive electrical delineation of the PCBM cluster while increasing the voltage. In the vicinity of the PCBM clusters no current is detected irrespective of the voltage (see arched area in Figure 4.11 (b)). This is explained by the large injection barrier between the ITO and the HOMO level of the surrounding MDMO-PPV, likely to prevent any holes from contributing to the conduction in the blend band. It can also be seen that away from the PCBM clusters and the no-current zone (arched area), the current signal contrast is the same as in the centre of the PCBM cluster. Therefore, it can be concluded that the current recorded emerges from the conduction of electrons in PCBM.

Interestingly, reversing the bias polarity did not yield opposite contrast indicating changes in the leading conduction mechanisms. Figure 4.12 shows the variations of the TUNA current gradually increasing the dc sample bias from 0 to

6.4 V. At low voltages uniform current contrast is observed. When the voltage increases, the current is progressively increasing in the MDMO-PPV rich regions. Slightly lower current is measured at the position of PCBM-rich regions. In this scope, the results obtained in Figure 4.12 are consistent with the ones obtained in Figure 4.10. Therefore, it can be concluded that the current recorded emerges from the conduction of holes through the MDMO-PPV in the blend. Meanwhile, the zero current observed at the location of the PCBM clusters is attributed to the high injection barrier between the ITO and the PCBM. On top of the image, a slightly higher current is detected at the position of few PCBM clusters (dotted circle in Figure 4.12 (b)), this is attributed to the remnant thin MDMO-PPV rich layer.

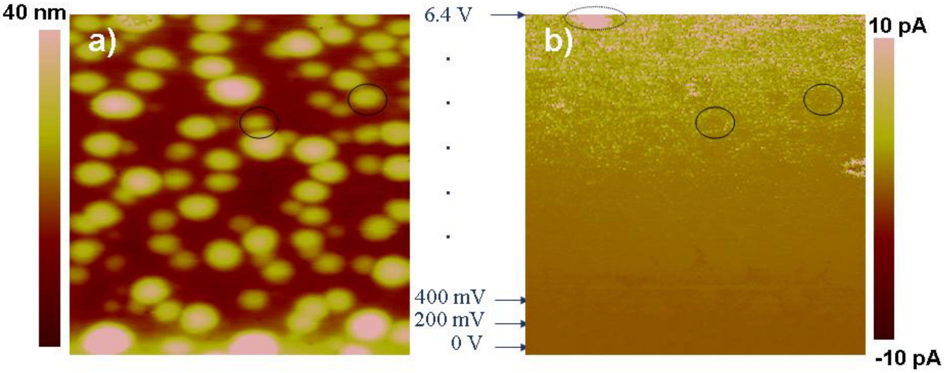

Figure 4.12: (a) 2×2 μm^2 C-AFM topography and (b) current images of the MDMO-PPV:PCBM 1:4 (toluene) blend while gradually increasing the dc sample bias from 0 V up to 6.4 V with steps of 200 mV. The circles indicate the position of two PCBM clusters. The dotted circle on top of (b) indicates a PCBM cluster with an unusual contrast.

4.2.4. P3HT:PCBM blends

4.2.4.1. Crystallization of P3HT

Figure 4.13 shows the 500×500 nm² C-AFM topography (a) and current (b) image simultaneously acquired across a 2:1 P3HT:PCBM blend.

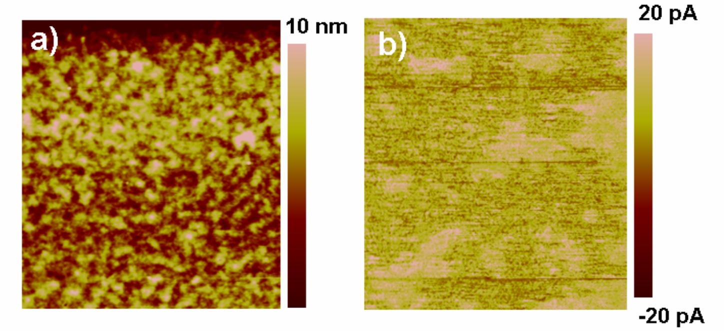

Figure 4.13: (a) 0.5×0.5 μm^2 C-AFM topography and (b) current images of the P3HT:PCBM 2:1 blend not annealed with a sample bias of 1.5 V applied.

While the sample exhibit smooth surface with low morphological variation (< 10 nm) compared to PPV based blend, larger current variations, of the order of 10 pA, were measured across the sample upon a sample bias of 1.5 V. Interestingly, nanoscale variations of the current could be observed. These variations are however not as pronounced for blends with higher PCBM contents (not shown). This suggests that the current variations for the 2:1 blend originate from more crystalline regions, most likely to occur increasing the amount of P3HT in the blend, mentioned in chapter two. In order to further investigate the charge transport mechanisms in crystalline regions, pure P3HT film was characterized by means of local I-V profiles. The investigations on pure material was motivated to avoid the possible contribution of PCBM on the I-V profile and offer highly crystalline regions, thus better conductivity properties. The poor signal to noise ratio of a single I-V profile, obtained by maintaining the tip immobile while ramping the voltage, implies the capture of several profiles, latterly averaged. However as previously mentioned, several ramps are likely to generate electrical damage, thus affecting the liability of the overall profile. To overcome this problem, a current scan was made on a narrow (500 nm) fresh area while gradually increasing the voltage. By averaging the current signal line by line, a "local" I-V curve could be made. A typical I-V profile is given in Figure 4.14. A perturbation in the local I-V curve can be observed, originating from an inaccuracy of the measurement.

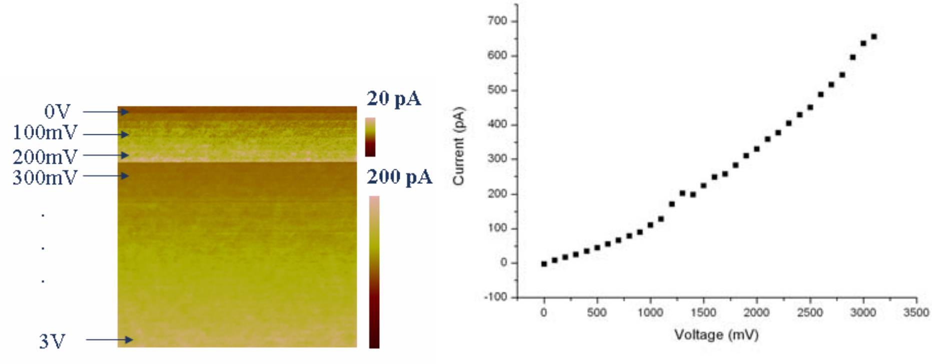

Figure 4.14: (left) Current image while gradually increasing the sample bias from 0 V up to 3 V and (right)" local" I-V profile obtained by averaging the current signal line by line in the left image of pure P3HT film.

A square dependence of the current density upon positive bias is evidenced, in good correspondence with macroscopic electrical characterization methods indicating that the charge transport mechanism in pure P3HT is governed by space charge limited current (SCLC), in which the current variation with the voltage applied is shown to follow the relation:

$$J = \frac{9}{8}\varepsilon_r \varepsilon_0 \mu \frac{V^2}{L^3}$$

equation 4-6

with J the current density, ε_0 the vacuum permittivity, ε_r the dielectric constant of the sample ($\varepsilon_0 = 8.854*10^{-12}$ A.s/V.m and $\varepsilon_r = 3.84$ for P3HT), μ the carrier mobility, and L the thickness of the sample.[26] The I-V curve obtained with C-AFM is compared with the dark I-V characteristics of a pure P3HT device. Profiles are shown in Figure 4.15. Both curves have been corrected for the build-in field caused by: offset in work function of ITO/PEDOT and Al compared to $PtIr_5$ and ITO, the interfacial state and ageing.

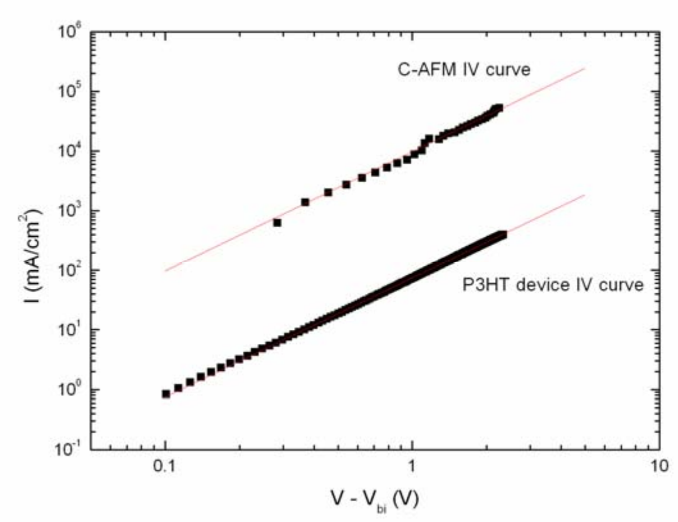

Figure 4.15: Log-log plot of the I-V profile of Figure 4.14 compared to the I-V profile obtained for a P3HT device measured in dark conditions.

Assuming a tip radius of 20 nm, hence a contact radius of the same order, the current density could be determined. Both profiles confirms charge transport mechanisms in the SCLC regime, but with a large difference of mobility. Using previous equation, a carrier mobility of $8.8*10^{-3}$ cm²/V.s was determined for C-AFM measurements. The mobility obtained from conventional macroscopic I-V characterization yielded $1.9*10^{-4}$ cm²/V.s, which is ± 40 times lower than the results obtained with C-AFM. It would suggest that the C-AFM measurement was performed in a place where locally the mobility is higher compared to the overall film. This is however quite unlikely considering the reproducibility of the measurement in different regions. Major discrepancies are therefore expected to yield from the different geometry of the experimental set-up recording the I-V profile. In the case of C-AFM, instead of considering the tip-sample electrical contact as a plate-plate system with consequently a uniform distributed electric field (Figure 4.16 (a)), a new model was found were SCLC regime is adapted to sphere-sphere interaction.[26] Ideally, a model should be made describing a half sphere/plate interaction (Figure 4.16 (b)), but this is beyond the scope of this thesis.

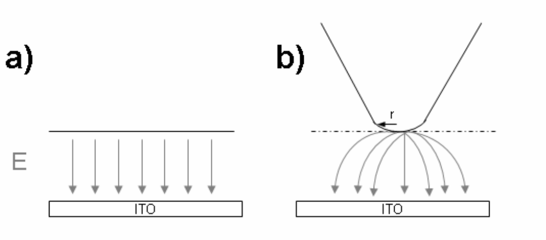

Figure 4.16: Electric field lines when current flows through a flat contact (a) or an AFM probe (b).

The SCLC is then described by the following relationship:

$$I = \frac{3\pi}{4}\mu\,\varepsilon_r\,\varepsilon_0\frac{V^2}{r} \qquad \textit{equation 4-7}$$

with r the thickness of the layer (100 nm).[26] The I-V profile obtained in Figure 4.14 (right) was fitted with equation 4-7 with V corrected with the build-in voltage (V_{bi}), shown in Figure 4.17. A V_{bi} of -0.55 V was obtained and the mobility was found to be $6.2*10^{-4}$ cm²/V.s, which is in better agreement with the mobility determined for the macroscopic solar cell device.

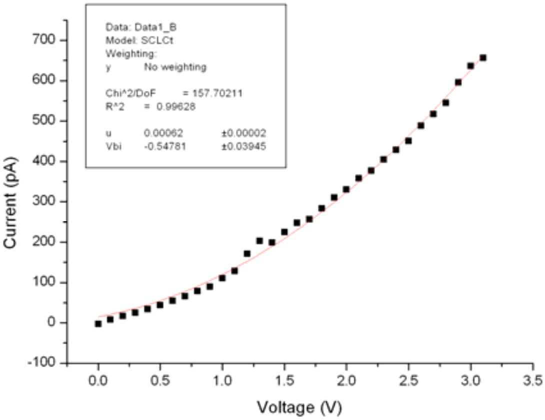

Figure 4.17: I-V profile of Figure 4.14 fitted with sphere/sphere interaction.

4.2.4.2. Crystallization of PCBM

In order to get an idea of the local conductive properties of the large PCBM needles formed upon annealing in P3HT:PCBM blend systems, C-AFM characterization has been attempted. In Figure 4.18, the topography (a) and current (b) images of a P3HT:PCBM 1:1 blend annealed for 10 min at 125°C are displayed. In Figure 4.18 (c), the topography and current profiles are depicted obtained from the black line in Figure 4.18 (a) and the red line in Figure 4.18 (b) respectively. Topographic variations in the order of 800 nm are observed. This is much higher than what observed for needles obtained after 5 min of annealing at 125°C of the 1:1 P3HT:PCBM blend in chapter 2. A topographic depression is observed in the vicinity of the needle. This depression region is expected to coincide with the depletion region consisting of a highly crystalline almost pure P3HT area surrounding the needle and formed by diffusion of PCBM upon annealing towards the PCBM crystalline needle. Around the depletion region semi-crystalline P3HT:PCBM blend is found. Current variations in the order of 5 pA are observed for a dc sample bias of -40 mV. This indicates locally a much higher conductive material than what has so far been observed in semi-conducting organic materials. Furthermore, the depletion region exhibits a higher current signal, thus a higher conductivity, compared to the rest of the blend and the PCBM needle itself. This is consistent with the presence of highly crystalline P3HT, which the nanoscale morphology is expected to improve the conductive properties. Interestingly, the spatial extend of the depletion region (current) ($\sim$ 10 μm) is higher than the one of the depression region (topography) ($\sim$ 1 μm). The results obtained for the depression region are consistent with findings in chapter 2. A gradual decrease of the conductivity is observed while moving away from the PCBM crystal. The PCBM needle has a slightly lower conductivity compared to the P3HT:PCBM region surrounding the depletion region originating from the large injection barrier between the tip and the LUMO of the PCBM. On the PCBM needle itself current contrast is observed.

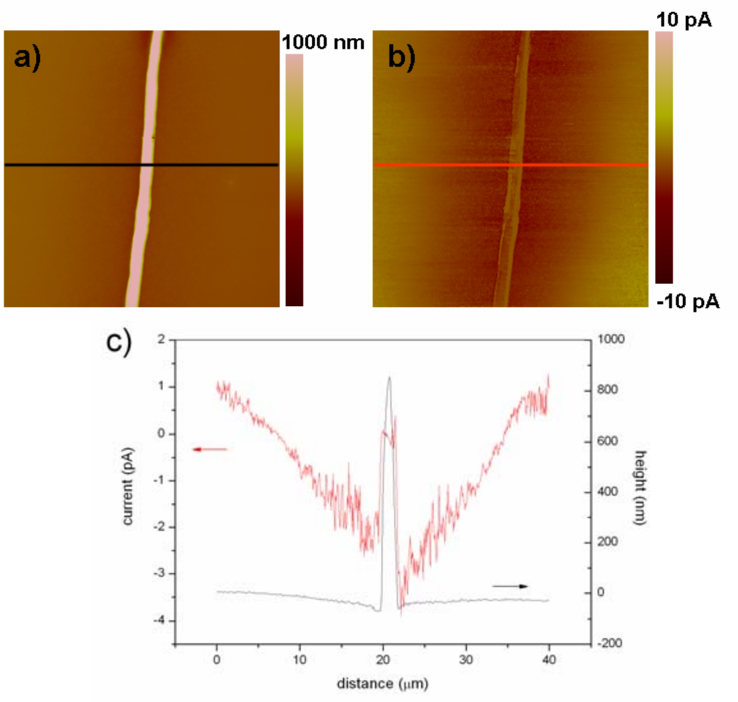

Figure 4.18: (a) 40×40 µm^2 C-AFM topography and (b) current images of the P3HT:PCBM 1:1 blend annealed for 10 min at 125°C with a sample bias of -40 mV applied. (c) Topography (black) and current (red) and profile obtained across the black and red line indicated in (a) and (b) respectively.

In order to have a look at the I-V profiles in the different critical regions a current image was obtained while gradually increasing and decreasing the voltage, as shown in Figure 4.19 (a). The I-V profiles extracted across the lines A, B and C displayed in Figure 4.19 (a) are shown in Figure 4.19 (b). Additional investigations at larger bias have also been performed to complete the profiles given in Figure 4.19 (b). Although different locations had to be considered in these additional measurements, good consistency was observed between the scans both in terms of morphology and current range. In Figure 4.19 (b) significant similarities are observed between the I-V profiles recorded in the depleted region and the blend. Interestingly for a negative bias, a higher current, thus a higher conductivity, is measured in the depletion region compared to the blend, consistently with the higher crystalline degree of P3HT in the vicinity of the needle. Only at positive biasing, current is recorded across the

PCBM needle. The zero signal observed at negative dc sample bias across the PCBM needle can be explained by the large injection barrier at the tip-sample contact. The low current for positive dc sample bias indicates poor conduction across the PCBM needle most likely induced by the electronic states at the different interfaces. We have to consider that in the blend I-V profile at positive dc sample bias, both the conduction along P3HT and PCBM has to be taken into account. Hence, the higher current density observed in the blend compared to the PCBM depleted region. Yet this contribution seems to be minor and at both negative and positive voltages applied, the charge transport in the blend seems mainly governed by holes in P3HT.

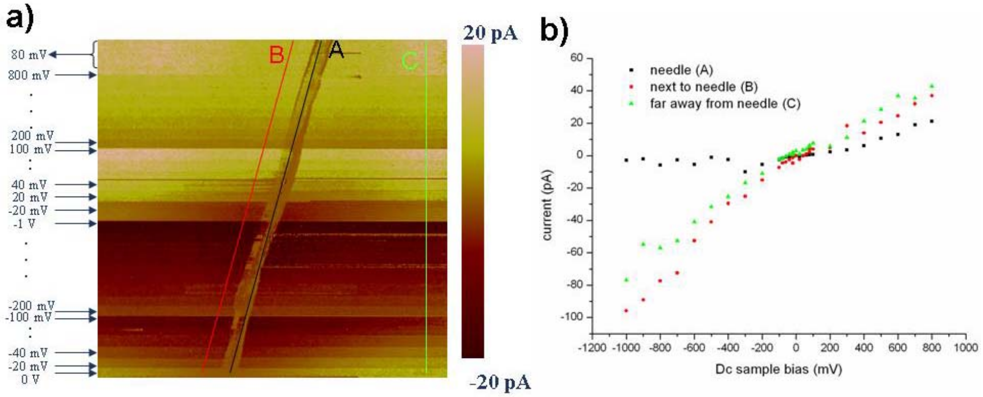

Figure 4.19: (a) C-AFM current image obtained by gradually increasing and decreasing the voltage and corresponding I-V profile obtained by extracting the current at the position of the needle (A), along the needle (B) and away from the needle (C) of the P3HT:PCBM 1:1 blend annealed for 10 min at 125°C.

4.3. General discussion and conclusion

The traditional EFM set-up was adapted to successfully locally probe electrical properties of conjugated polymer blends. MDMO-PPV:PCBM and P3HT:PCBM current-carrying blends evidenced a non-linear voltage drop, indicating that the layers behave as diffusive conductors with voltage dependent conductivity. In the "reference" blend system MDMO-PPV:PCBM local variations of voltage could be linked to resistance differences between the phase separated PCBM clusters with the surrounding blend. Within a PCBM cluster the resistance is shown to be lower compared to the surrounding blend. EFM-probing of the of the homogeneous P3HT:PCBM blend resulted in local voltage variations, but no clear explanation could be drawn. Probing the large PCBM needles with lateral EFM, was impossible because of the large topography variations and the preferential growth of PCBM on the Au.

Nevertheless, the difficult interpretation of results and poor spatial resolution (~ 50 nm) still hamper quantitative interpretation of results and obstruct further extensive use of EFM. C-AFM was shown to be an ideal complementary technique to probe transversal conductivity properties of organic blend samples, in particular for samples which do not show significant phase separation. For the MDMO-PPV:PCBM blend a resistive area surrounding the PCBM clusters was evidenced and electrically delineated. It could also be concluded that charge transport is mainly governed by holes in the MDMO-PPV in the positive voltage and electrons in PCBM for the negative voltage. The C-AFM characterization of P3HT:PCBM blends evidenced local current variations mainly attributed to the difference of crystallinity of P3HT regions within the blend. An additional key feature is the ability to locally perform I-V profiles. From local I-V profiles it was shown that the charge transport in P3HT is mainly governed by space charge limited current. Local mobility of P3HT in the order of 10^{-4} cm²/V.s was determined, in good correspondence with conventional macroscopic mobility measurements. This turns C-AFM as an ideal candidate to locally probe charge transport mechanisms in nano-structured systems. Yet, the quantification remains an issue of discussion and needs to be further developed. Contrary to EFM, the high topographic variations of the large PCBM needles was not an obstruction for C-AFM measurements. Significant conductivity differences were observed between the PCBM needle, the PCBM depleted region surrounding the needle and the P3HT:PCBM blend. It was first seen that the depletion region extends over a wider area than observed with the topography image and what could be observed with profilometer measurements and fluorescence microscopy in chapter 2. A gradual decrease in conductivity is observed moving away from the needle coinciding with progressive PCBM mixing. The PCBM depleted region evidenced higher conductivity. From the I-V profiles it could be determined that irrespective of the bias polarity, the charge transport is shown to be mainly governed by the hole conduction in the P3HT.

As a more general conclusion it can be stated that from the results obtained on these two types of organic blends, it is demonstrated that the combination of AFM/EFM/C-AFM is a powerful approach to obtain information on local morphological and electrical properties of blended organic material systems and can therefore also be applied in other field of plastic and hybrid electronics (e.g. hybrid solar cells, LEDs, transistors, (bio-)sensors,..).

4.4. References

[1] W. Vandervorst, T. Clarysse, J. Vanhellemont, A. Romano-Rodriguez, *J. Vac. Sci. Technol. B,* **10**, 1992, 449.
[2] C. C. Williams, *Annu. Rev. Mater. Sci.*, **29**, 1999, 471.
[3] D. Álvarez, J. Hartwitch, M. Fouchier, P. Eyben, W. Vandervorst, *Appl. Phys.Lett.*, **82**, 2003, 1724.
[4] K. Maknys, O. Douhéret, S. Anand, *Appl. Phys. Lett.*, **83**, 2003, 4205.
[5] S. Richter, M. Geva, J. P. Gamo, R. N. Kleiman, *Appl. Phys. Lett.*, **77**, 2000, 456.
[6] A. Olbrich, B. Ebersberger, C. Boit, J. Vancea, H. Hoffmann, H. Altmann, G. Gieres, J. Wecker, *Appl. Phys. Lett.*, **78**, 2001, 2934.
[7] M. Nonnenmacher, M. P. O'Boyle, H. K. Wickramasinghe, *Appl. Phys. Lett.*, **58**, 1991, 2921.
[8] S. Sadewasser, Th. Glatzel, S. Schuler, S. Nishiwaki, R. Kaigawa, M. Ch. Lux-Steiner, *Thin Solid Films*, **431**, 2003, 257.
[9] G. Lévêque, P. Girard, E. Skouri, D. Yarekha, *Appl. Surf. Sci.*, **157**, 2000, 251.
[10] F. Robin, H. Jacobs, O. Homan, A. Stemmer, W. Bächtold, *Appl. Phys. Lett.*, **76**, 2000, 2907.
[11] Scanning Probe Microscopy: Characterization, Nanofabrication and Device Application of functional Materials, NATO Science Series, Kluwer Academic Publishers, 2005.
[12] S. E. Shaheen, C. J. Brabec, N. S. Sariciftci, F. Padinger, T. Fromherz, J. C. Hummelen, *Appl. Phys. Lett.*, **78**, 2001, 841.
[13] C. H. Lei, A. Das, M. Elliott, J. E. Macdonald, *Nanotechnology*, **15**, 2004, 627.
[14] A. Das, C. H. Lei, H. E. Thomas, M. Elliott, J. E. Macdonald, P. Glarvey, M. L. Thurner, *Appl. Surf. Sci.*, **252**, 2006, 5477.
[15] C. H. Lei, A. Das, M. Elliott, J. E. Macdonald, M. L. Thurner, *Synth. Met.*, **145**, 2004, 217.
[16] D. C. Coffey, D. S. Ginger, *Nature materials*, **5**, 2006, 735.
[17] R. Turton, The Physics of Solids, Oxford University Press, Oxford, England, chapter 5-6, 2002.
[18] http://www.hmi.de/bereiche/SE/SE2/arbeitsg/analytik/nano
[19] M. Nonnenmacher, M. P. O'Boyle, H. K. Wickramasinghe, *Appl. Phys. Lett.*, **58**, 1991, 2921.
[20] Electrostatic Force Microscopy for Autoprobe CP Research Operating Instructions, Thermomicroscopes, Sunnyvale, USA, 2000.
[21] S. W. Howell, "Electrostatic Force Microscopy studies of nanoscale systems", PhD thesis, Perdue University, 2001.

[22] H. Hoppe, T. Glatzel, M. Niggemann, A. Hinsch, M. Ch. Lux-Steiner, N. S. Sariciftci, *Nano Lett.,* **5**, 2005, 273.
[23] A. Alexeev, J. Loos, M. M. Koetse, *Ultramicroscopy*, **106**, 2006, 191.
[24] D. J. Miliron, I. G. Hill, C. Shen, A. Kahn, J. Schwartz, *J. Appl. Phys.*, **87**, 2000, 572.
[25] O. Douhéret, A. Swinnen, M. Breselge, I. Van Severen, L. Lutsen, D. Vanderzande, J. Manca, *Microelectronic engineering*, **84**, 2007, 431.
[26] M. A. Lampert, P. Mark, Current injection in solids, Academic Press, New York and London, 1970.

5. Summary and future work

In the next two paragraphs a brief overview will be given of all the results obtained in this thesis and future work will be discussed.

5.1. Summary of the results obtained in this thesis

The major objective of this thesis was to correlate morphology to the electrical properties of bulk heterojunction solar cells. Since at the beginning of this work P3HT:PCBM solar cells gave the best efficiencies, the focus was on this type of blend. First, an extensive morphology study was needed since it is generally known that morphology influences the properties of bulk heterojunction solar cells. Secondly, the relationship between morphology and electrical properties was still inefficiently known and therefore a few options were explored how to correlate them.

First, the P3HT:PCBM blend was studied morphologically with a wide variety of techniques, i.e. transmission electron microscopy (TEM), X-Ray diffraction (XRD), atomic force microscopy (AFM), confocal fluorescence microscopy and optical microscopy. Different blend ratios and various annealing conditions were studied. Using XRD, the non annealed pure P3HT was found to be semi-crystalline. With addition of PCBM the crystallization is suppressed and can subsequently be regained by annealing treatment. With annealing treatment, a twofold crystallization was observed using TEM and optical microscopy. Upon short (i.e. 5 min) annealing times and lower annealing temperatures (i.e. 75°C-100°C) an enhanced crystallization of P3HT appeared. Increasing further annealing temperature and time, revealed the formation of novel needle-like crystalline PCBM-structures, identified by SAED as triclinic PCBM, of a few μm up to 100 μm in size. At specific preparation conditions these crystals can grow out to a two-dimensional network of PCBM-needles and in some cases to PCBM-pallets. It has been demonstrated that key-parameters to “tune” the dimensions and spatial distribution of the PCBM needles are blend ratio and annealing conditions. It was found that the crystallization mechanism of P3HT was not responsible for this specific shape of crystals, since annealing of regiorandom P3HT:PCBM blends rendered the same needle like PCBM crystals, but rather the low Tg of P3HT in combination with the different start morphology compared to MDMO-PPV:PCBM blends. Secondly, the PCBM needles were studied more in detail. Around the PCBM needles a thinner area of almost pure and highly crystalline P3HT was found. This PCBM depleted region originates from diffusion of PCBM out of the matrix towards a growing PCBM crystal upon annealing. Confocal microscopy with fluorescence confirmed that regions surrounding the needles are made of almost pure P3HT. A stable morphology was obtained when all the PCBM has diffused out of the matrix. This was achieved for the 1:2 blend when annealed between 8-16 hours at 100°C. Thus, longer annealing times result in an irreversible morphology consisting of a pure matrix of highly crystalline P3HT embedding PCBM crystals. Moreover, these large PCBM crystals were also encountered in solar cell devices, hampering the perfect operation of the solar cell.

In order to get a clear idea of how and why this morphology of the P3HT:PCBM blend is formed a preliminary state diagram was composed. Differential scanning calorimetry (DSC) was used for studying melting and crystallization behaviour while modulated temperature differential scanning calorimetry (MTDSC) was used for glass transition determination. First the pure P3HT and PCBM was investigated followed by different blend compositions. The T_g of pure P3HT was determined at 18.7°C and a melting and crystallization temperature of 209°C and 179°C respectively, values which are in good correspondence with literature reports. Both crystallization and melting peaks exhibited a shoulder originating probably from different crystal structures. For the first time a T_g for PCBM, i.e. 130°C, could be found. A double melting peak, a small one at 266°C and a larger one at 287°C, was encountered for PCBM which can originate from two crystal forms, i.e. triclinic and monoclinic, present in pristine PCBM. A crystallization peak was found around 228°C.
For all blend ratios, a single glass transition was observed. With increased PCBM contents the T_g shifts from the T_g of P3HT till the T_g of PCBM, meaning that all blend compositions are in a homogeneous phase, down to a scale of 10 nm. Only phase separation induced by the crystallization of either P3HT or PCBM could be found, no “intrinsic” liquid-liquid phase separation is observed. Phase separation was also not observed in the melt, confirming our observations of the glass transition. From the results obtained for the crystallization and melting behaviour of the blends, it could be concluded that with addition of P3HT the melting crystallization of PCBM lowers significantly, in contrast to the melting temperature, which decreased much less. The same effect is occurring when PCBM is added to P3HT, although here the effect is more pronounced. Hence, both components impede each others crystallization. The most amorphous blend is thus obtained with a 60% weight concentration of PCBM. That PCBM impedes the crystallization of P3HT was also seen in the morphology study in chapter two, nevertheless it is demonstrated by formulating a state diagram or preliminary phase diagram, a quick and more accurate idea can be given of how the blend behaves morphologically. A lot off information can be quickly deducted from a state diagram. Moreover, since solar cells are typically operating outdoor at a maximum temperature of 80°C, the beginning of the glass transition is an important parameter in the study of solar cells, since below the glass transition the blends are in a ‘stable’ glassy state meaning no morphological changes can

occur. For the P3HT:PCBM blends, only phases containing 90 wt% PCBM or more are in the 'stable' glassy state at a temperature of 80°C, meaning that P3HT:PCBM blend is not that suitable for solar cell fabrication, where long term thermal stability is necessary. Nevertheless, one should keep in mind that still physical ageing could occur. Since it is known now that annealing increases the solar cell properties of a P3HT:PCBM solar cell, partially because of the increased crystallization of the P3HT, the end of the glass transition can be used as the lower limit of the temperature window for annealing (increasing the crystallinity or changing the morphology).

An elaborate morphological study was now performed. In order to link this morphology to local electrical properties different SPM techniques were applied. In this work, the opportunity to use EFM and C-AFM has been provided. Interestingly, the non-contact scanning procedure inherent to EFM provides a non-destructive scanning guarantee on such soft materials as organic semi-conductors. In C-AFM, this major issue was handled using very soft probes. C-AFM was specifically attractive for its ability to map sample conductivity and local I-V profiling. The traditional EFM set-up was adapted successfully in order to probe local lateral conductivity differences, while the C-AFM is used to probe transversal conductivity differences and to analyse charge transport mechanisms.

Blends consisting of a PPV-derivative and PCBM have first been investigated. The standard EFM set-up was successfully adapted to perform local lateral conductivity measurements. A lateral non-linear voltage drop was observed for the PPV:PCBM film indicating that the current carrying film acts as a diffusive conductor. At the Au contacts the voltage drop is small, indicating a low injecting barrier between the current carrying film and the Au contact. Local voltage variations were linked to resistivity differences in the film and within a PCBM cluster the resistance is shown to be lower compared to the surrounding blend.

The main focus in this thesis was the study of P3HT:PCBM blends. Lateral EFM was also performed and similarly to PPV:PCBM blend also here a non-linear voltage drop was observed and a small injection barrier is present between the Au contacts and the current carrying film. Small local voltage variations were also observed. However, in spite of the homogeneity of the film, it was complex to correlate them with the electrostatic properties of the film. Besides, the large PCBM needles could not be analysed either because of the high topographic variations and its significant perturbing contribution to the EFM signal.

In parallel to EFM investigations, C-AFM has been applied to probe the transversal conductivity properties of the same PPV:PCBM and P3HT:PCBM blends. Since C-AFM is operating in contact mode, the possible scan induced topographical and electrical damage had to be investigated. Using soft probes, topographic damage could be reduced enormously. However, local electrical damage was observed most likely emerging from electrochemical effects at the tip sample contacts and resulting in significant current intensity. This therefore imposed the scans to always be performed on a new area. First, MDMO-PPV:PCBM were investigated and very low current variations (in the order of pA) could be observed. A resistive area around the PCBM clusters was further evidenced and electrically delineated. By gradually varying the voltage upon scanning conducting mechanism were investigated. Charge transport is mainly governed by holes in the MDMO-PPV in the positive voltage and electrons in PCBM for the negative voltage. P3HT:PCBM blends were also characterized. Larger conductivity compared to the MDMO-PPV blend was found. Small conductivity differences were attributed to local differences in crystallinity of P3HT. Further, pure P3HT was investigated to analyse locally the charge transport mechanism. From local I-V profiles it was shown that the charge transport in P3HT is mainly governed by space charge limited current. The calculation for the mobility was based on sphere/sphere interaction model most likely to better represent the geometry of the tip-sample interaction. A mobility of 6.2×10^{-4} cm²/V.s in good agreement with what is measured with conventional methods. Contrary to EFM, the high topographic variations of the large PCBM needles was not an obstruction for C-AFM measurements. Significant conductivity differences were observed between the PCBM needle, the PCBM depleted region surrounding the needle and the P3HT:PCBM blend. It was first seen that the depletion region extends over a wider area than observed with the topography image. A gradual decrease in conductivity is observed moving away from the needle coinciding with progressive PCBM mixing. The PCBM depleted region evidenced higher conductivity. I-V profiles were also performed to compare charge transport mechanism in the different areas. Irrespective of the bias polarity, the charge transport is shown to be mainly governed by the hole conduction in the P3HT.

Both techniques have been shown to be good candidates to locally probe conductivity differences. It is demonstrated that the combination of AFM/EFM/C-AFM can be a powerful approach to obtain complementary information on local morphological and electrical properties of blended organic material systems.

5.2. Future work

Towards the future, the demonstrated ability to tune the dimensions of needle-like PCBM crystals through appropriate blend ratio and annealing conditions opens a new route to obtain (nano-)structuring. Since (nano-)structuring is of great importance for novel organic and hybrid electronic applications, future work will consist of electrical measurements and ordering in two or even three dimensions of these crystalline needles. Preliminary experiments have already been performed by stamping the P3HT:PCBM films with a predefined mm-stamp. With annealing it was seen that at the pressed regions, PCBM crystals started to grow, seen in Figure 5.1. By optimizing the stamp procedure and fabricating a stamp with μm structures. Structuring of PCBM needles could be possible.

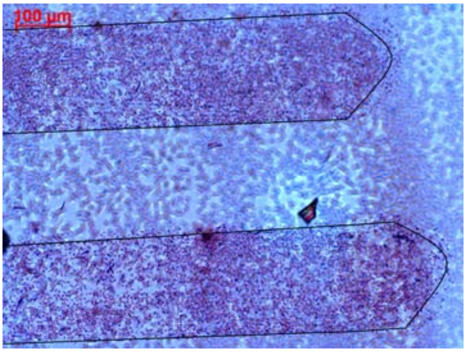

Figure 5.1: Optical microscopy image of stamped and consequently annealed P3HT:PCBM film.

In addition to this stamping, rubbing of the P3HT:PCBM film was performed using AFM in contact mode. By gently, scanning over the surface and applying a small force P3HT chains at the surface could be aligned. By applying an additional heat treatment the P3HT in the bulk is crystallized and the formation of PCBM crystals is impeded, even after an annealing of 2 hours at 170°C no crystals are found at the spot were the rubbing was done. Future experiments that can be done consist of lateral EFM measurements to determine mobility changes according to the rubbing direction.

It was demonstrated that formulating first a state diagram would accelerate the search for the better bulk heterojunction solar cell and minimize tremendously the work effort. Since in this work, only a preliminary phase diagram or better a state diagram was formulated, future work will consist of composing a 3D phase diagram were the effect of solvent is shown on the thermodynamic properties of the P3HT:PCBM blend. In addition, the influence of different heating rates will be investigated. Finally, microthermal analysis could be performed on these blends, which enables local thermal conductivity, topography and modulated temperature (phase and amplitude) probing by combining thermal analysis with AFM. In that way morphology could be directly correlated to the thermodynamic properties of the blend.

EFM and C-AFM were used to get a basic idea of what is possible with these techniques. Still a lot off work has to be done to optimise both EFM and C-AFM measurements. A first important parameter that has to be adjusted is the operation in air. Operating in vacuum or nitrogen atmosphere would prevent oxidation of the polymer, especially important if the system would be extended with a thermal stage, making it possible to simultaneously map conductivity differences with annealing treatment. Additionally the effect of illumination should be further investigated. Appropriate lightning, corresponding to the absorption spectra of the blend, should be provided. The system should be extended, making it possible to investigate the photovoltaic phenomena in full solar cell devices with and without illumination (AM 1.5 spectra). Also, the quantification of the analysis of the local I-V profiles should be improved by formulating the appropriate model for the tip-sample interaction (half sphere/plate). An additional idea is to combine the local 2D mapping of C-AFM with the well-established electrical characterisation methods, such as local field effect transistor (FET) and local time of flight measurements. Since it was demonstrated that the combination of AFM/EFM/C-AFM is a powerful approach to obtain information on local morphological and electrical properties of blended organic material systems, it can therefore in the future also be applied in other field of plastic and hybrid electronics (e.g. hybrid solar cells, LED’s, transistors, (bio-)sensors,..).